CDF/ANAL/ELECTROWEAK/CDFR/7104
version 1.2

Measurement of the W Boson Mass in Run 2

Ashutosh Kotwal and Chris Hays
Duke University
Sahand Hormoz, William Trischuk, Oliver Stelzer-Chilton, and Ian Vollrath
University of Toronto
Larry Nodulman
Argonne National Laboratory

August 9, 2004

Abstract

We describe a measurement of the W boson mass using $\approx$200 pb^{-1} of $\sqrt{s}$=1.96 TeV $p\bar{p}$ data taken with the CDF II detector. We measure the mass for both electron and muon final states from the transverse mass distribution. We find a combined mass of $m_W = 80257 \pm 33(\text{stat.}) \pm 70(\text{syst.})\text{MeV/c}^2$. *The central value includes a blinding offset!* We also study fits to the charged-lepton p_T and neutrino p_T distributions and find compatible results with slightly larger uncertainties.

Contents

1 Introduction

The mass of the W boson is an important parameter of the Standard Model. Precise knowledge of the W boson mass, combined with that of the top mass, results in a significant constraint on the mass of the unobserved Higgs particle. The current world measurements of m_W=(80.426 $\pm$ 0.034) GeV and m_{top}=(178.0 $\pm$ 4.3) GeV produce a Higgs mass estimate of m_H=117^{+67}_{-45} GeV. Incorporating the current data from the Tevatron will reduce the uncertainties on both the top and W masses, further constraining the Standard Model Higgs mass.

We describe in this note the first W mass measurement from $\sqrt{s}$=1.96 $p\bar{p}$ collisions. The mass is measured using the electron and muon decays of the W, and fitting the transverse mass and lepton and neutrino momentum distributions, for different mass hypotheses. The data correspond to (218.1 $\pm$ 12.4) pb^{-1} (electron channel) and (190.8 $\pm$ 10.9) pb^{-1} (muon channel) taken with the CDF detector between February, 2002, and September, 2003.

Because we cannot measure the longitudinal momentum of the neutrino – its transverse momentum is inferred from transverse momentum balance of all activity in the event – we cannot fully reconstruct the final-state W candidates. In order to extract the W mass we compute the transverse mass:

$$m_T = \sqrt{2p_T(l)p_T(\nu)[1 - cos(\phi_l - \phi_\nu)]},$$

which depends only on the measurable quantities in W decay. Unfortunately this quantity does not lend itself to analytic parametrisation. This leads us to use a Monte Carlo simulation to predict the shape of the transverse mass distribution as a function of m_W. By fitting these predictions to the data – with a binned maximum-likelihood fit – we can extract the W boson mass.

These lineshape predictions depend on a number of physics and detector effects that we constrain from control samples or simulation. Important physics effects include internal QED radiation, the intrinsic W boson transverse momentum and the proton parton distribution functions. Detector effects include external bremsstrahlung in the detector material, tracker momentum scale, calorimeter energy scale, resolutions of both detectors, and the detector acceptance. In order to study these effects at the level of 10^{-4} we require a detailed simulation where we can control each effect and routinely generate sample sizes of >10 million events to study systematic effects. We have developed a sophisticated, fast simulation for this purpose.

The W mass measurement consists of the following components: Event generation, including next-to-leading-order photon and gluon radiation (Section 2); detector simulation (Section 3); event selection (Section 4); calibration of detector energy and momentum scales (Section 5); modelling the hadronic recoil measured in the calorimeter (Section 7); and measurement of the backgrounds and the modelling of their distributions (Section 8). We describe each component along with its systematic uncertainty. We show the final fit results, gather together all the systematics and combine the results in Section 9.

We include a random offset – drawn from a flat distribution ranging from -100 MeV/c^2 to + 100 MeV/c^2 – in all our fit mass values prior to final approval of the result. This protects us from inadvertently tuning our model in such a way as to bias the fit m_W. This blinding offset is *still* included in the results quoted in this version of the note.

2 Event Generation

In order to construct templates for extracting the best-fit W mass, we generate W events with RESBOS [1], which captures the relevant QCD physics and models the W p_T spectrum well. This is coupled with WGRAD [2], which accounts for relevant QED processes, such as final-state radiation (FSR). We incorporate the WGRAD physics by adding WGRAD photons to the two-body RESBOS events. We discuss in detail the systematic uncertainties arising from both the WGRAD and RESBOS generators.

2.1 Modeling QED with WGRAD

We simulate QED corrections to W production and decay with WGRAD, which includes all $\mathcal{O}(\alpha)$ electroweak processes including a single real final-state photon as well as the final-state soft and virtual photonic corrections.

We use a version of WGRAD that produces unweighted events [3] (WGRAD on its own produces weighted events). This is necessary for our procedure of adding WGRAD photons to the RESBOS events as well as for future plans to numerically merge WGRAD with RESBOS, the details of which are beyond the scope of this note. The unfavorable aspect of using unweighted events is that the unweighting procedure can be quite slow (typically $\sim$ 1 sec/event). It should be noted that WGRAD contains no QCD effects and thus the produced W bosons have zero p_T.

QED effects relevant to W production and decay are (i) photon radiation off the incoming quarks, (ii) photon radiation off the W propagator, (iii) photon radiation off the final-state charged lepton, and (iv) all other radiative processes, e.g. virtual corrections via photons and Z bosons. In terms of the impact on measuring the W mass, the dominant effect is that of a single photon radiated off the final-state charged lepton. The next-largest effect is that of a second final-state photon (not included in the WGRAD calculation). Other processes such as real photons radiated off the initial-state quarks (ISR) and the propagator have small effects on the fitted W mass.

There are two intrinsic WGRAD parameters that are of particular interest to us. The first parameter is δ_s, which controls the photon energy cut:

$$E_\gamma > \delta_s \sqrt{\hat{s}}/2, \tag{1}$$

where $\sqrt{\hat{s}}/2$ is the parton energy in the parton-parton center-of-mass system. The second parameter is δ_c, which controls the photon collinearity cut:

$$\cos\theta < 1 - \delta_c, \tag{2}$$

where θ is the angle between the radiated photon and the charged lepton in the parton-parton center-of-mass frame. Note that this parameter is only relevant when ISR is included [3].

2.2 Shifts in the Fitted W Mass due to QED Processes

In order to gauge how various QED processes impact our measurement of the W mass we use a fast detector simulation that accounts for detector acceptance and resolution (Section 3). In the fast simulation we use generator-level WGRAD at leading order (LO) to construct a series of templates between 80 and 81 GeV. Then we use as input a simulated data file consisting of generator-level WGRAD with an input W mass of 80.45 GeV with some QED effects included (e.g. FSR, ISR, etc.). From a binned maximum likelihood fit we obtain the best-fit value of the W mass, which in the presence of QED corrections is shifted relative to the templates. In terms of real physics events this is unrealistic since the WGRAD samples have W $p_T = 0$. However, it is sufficient for testing the impact of QED alone, assuming the QED effects can be decoupled from the QCD.

As a consistency-check of the simulation and fitter we fit simulated LO data with LO templates. This results in a small bias in the muon channel and no statistically significant shift in the electron channel (Table 1). In addition, using LO templates, we simulate ISR-only and interference-only data (both of which are options in WGRAD), and these give shifts no larger than ~ 5 MeV. For these sets of data, we varied the WGRAD parameters δ_s and δ_c over wide ranges and found no significant deviations. Based on these findings we attribute a 5 MeV systematic uncertainty from the simulation and fitter, and a 5 MeV systematic uncertainty from ISR and interference. In addition, since ISR and interference are small effects over wide ranges of δ_s and δ_c, and given that FSR is the dominant effect with respect to the fitted W mass, we use only FSR in our implementation of WGRAD. Furthermore, to speed up CPU processing time we use the Berends and Kleiss (BK) approximation of FSR [4], which is included as an option of WGRAD. This approximates the soft and virtual terms in the calculation and is sufficient for studying FSR systematic effects [5]. The mass shifts observed for FSR (BK), relative to LO, are provided in Table 1.

Having isolated FSR (BK) as the QED correction to combine with RESBOS events, we investigate various systematic uncertainties related to this process. The first task is to determine how the shifts introduced by FSR (BK) change as we change the WGRAD parameters δ_s and δ_c. Since we know that δ_c is only relevant when ISR is included (because the collinear singularity is regulated by the finite lepton masses in the final state), we need only investigate the changes arising from δ_s. Figures 1 and 2 show the variation in the shift as a function of δ_s. We fit a line to the results of fits for reasonable values of δ_s (below 0.001) and take the uncertainty on the constant term as the systematic uncertainty from the choice of δ_s.

There is an uncertainty associated with using the Berends and Kleiss approximation of FSR instead of using the full treatment. It is CPU-intensive to acquire the necessary statistics to determine this uncertainty, so as a first approximation we use the uncertainty

Process	Fit Type	Shift (μ channel) (MeV)	Shift (e channel) (MeV)
LO	p_T	-7 ± 3	-4 ± 3
	m_T	-9 ± 5	-2 ± 3
	$\not\!\!E_T$	-12 ± 6	-2 ± 5
Interference	p_T	-4 ± 2	-7 ± 2
	m_t	-4 ± 3	-4 ± 3
	$\not\!\!E_T$	-2 ± 6	-7 ± 5
ISR only	p_T	$+1 \pm 3$	$+3 \pm 2$
	m_T	-2 ± 5	4 ± 3
	$\not\!\!E_T$	$+6 \pm 7$	$+3 \pm 4$
FSR (Berends and Kleiss)	p_T	-127 ± 5	-87 ± 5
	m_T	-149 ± 6	-107 ± 4
	$\not\!\!E_T$	-94 ± 8	-54 ± 7

Table 1: Shifts from the input W mass value of 80.45 GeV/c^2 for LO, ISR, interference terms, and FSR (using the Berends and Kleiss approximation). In the case of FSR, shifts to lower best-fit W mass values are observed due to the changes in the lineshapes of the fit variables from the radiated photon. The shift is smaller for the electron channel since collinear photons get merged with the electron energy cluster. The $\not\!\!E_T$ fit has smaller shifts than the p_T or m_T fits because wide-angle photons are added to the recoil and thus included in the $\not\!\!E_T$ calculation.

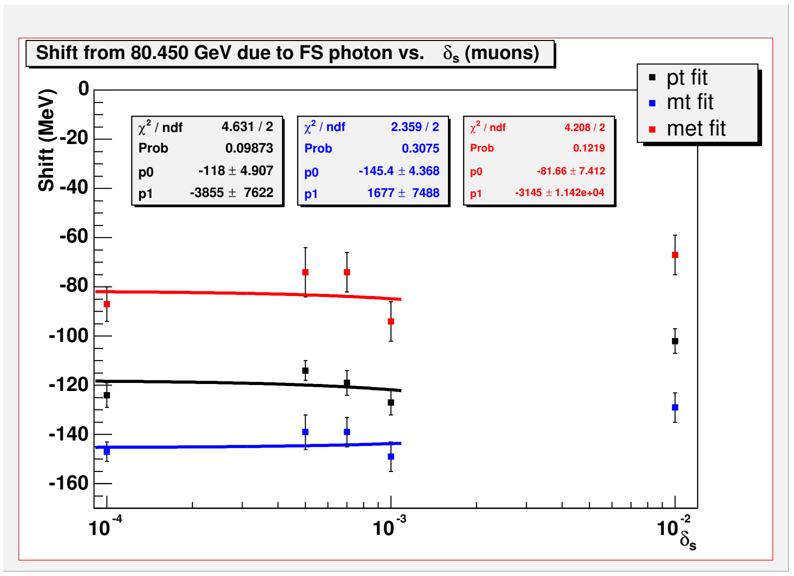

Figure 1: Shifts from the input W mass of 80.45 GeV for muons as a function of δ_s for the three fit variables: p_T^μ, m_T, and p_T^ν.

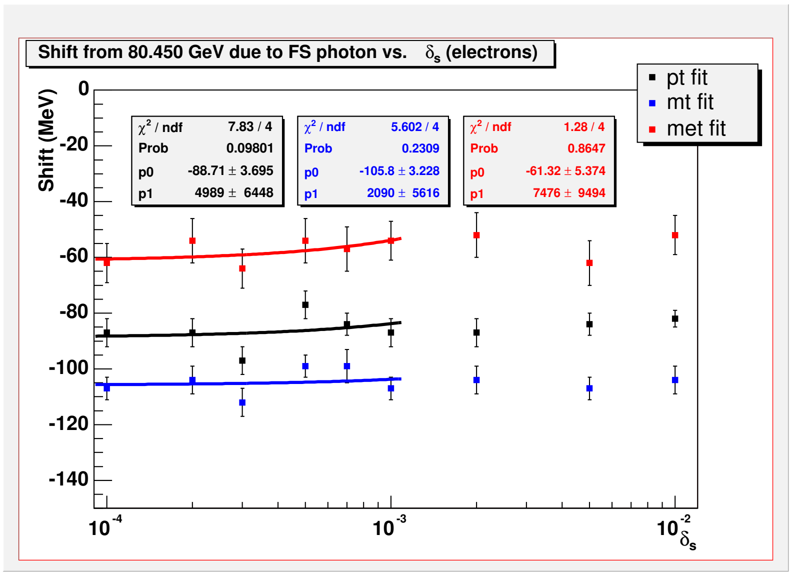

Figure 2: Shifts from the input W mass of 80.45 GeV for electrons as a function of δ_s for the three fit variables: p_T^e, M_T^W, and p_T^ν.

estimated in Run 1b for the m_T fit. The quoted uncertainties of 10 MeV for muons and 20 MeV for electrons [6] included several QED effects, so we take 5 MeV as the uncertainty due to FSR (BK) [19]. In the event that future studies demonstrate a statistically significant difference between FSR and FSR (BK), we will use the full FSR option in WGRAD.

Another source of uncertainty arises from the method in which we add photons to the RESBOS events. In the generation of the mass templates for fitting, we sample a 2D histogram of $\sqrt[3]{y}$ vs. $\sqrt{\Delta R}$, where $y = E_\gamma/(E_\gamma + E_l)$ and $\Delta R(l,\gamma) = \sqrt{(\Delta\eta)^2 + (\Delta\phi)^2}$. The cube- and square-roots flatten the sharply-peaking distributions of y and ΔR, respectively, rendering them amenable to sampling. Figures 3 and 4 show the projections of these two variables for both muons and electrons. To quantify the systematic uncertainty introduced by this method, we constructed templates by sampling a histogram generated at 80.45 GeV/c^2 with FSR (BK). We then used the original FSR (BK) events to produced simulated data. If by sampling the histogram we exactly reproduced FSR effects, we should see no shift in the best-fit mass value. The results are summarized in Table 2. We see a noticeable shift for muons, while the electrons do not show a statistically significant shift. This effect is thought to be an artifact of the sampling procedure and is smaller for electrons since collinear photons get combined with the electron energy cluster in the calorimeter, thus reducing the sensitivity to histogram-sampling biases. In the muon case we increase y_γ by 2 parts in 10000 to correct for the bias introduced by the method. No correction is applied in the electron channel. We attribute a 5 MeV systematic uncertainty to the muon channel from this method.

	Shift (MeV)		
Process	p_T	m_T	$\not{E}_T$
$W \to e\nu$	$+6 \pm 5$	$+6 \pm 6$	$+13 \pm 11$
$W \to \mu\nu$ (before correction)	-12 ± 6	-24 ± 7	-19 ± 10
$W \to \mu\nu$ (after correction)	$+6 \pm 6$	-2 ± 8	$+13 \pm 11$

Table 2: Shifts from $M_W = 80.45$ GeV due to sampling a histogram that contains WGRAD final state photons. A correction factor is applied in the muon channel to eliminate the shift.

As mentioned earlier, WGRAD currently does not include a second final-state photon. In the Run 1b W-mass analysis an external package called PHOTOS was used to investigate the impact of a second photon. That analysis concluded that the effect of a second photon on M_W (for the transverse mass fit) was less than 10 MeV for the muon channel and less than 5 MeV for the electron channel [6]. The authors of WGRAD are currently working on a calculation that includes the effect of a second photon [5] and we intend to incorporate this when it becomes available. However, for now we assume the shift in the fitted W mass from a second photon is 10% of the single photon shift [8], and take this as a systematic uncertainty on the measured mass (Table 3).

In summary, we sample a histogram of WGRAD photons to incorporate relevant QED

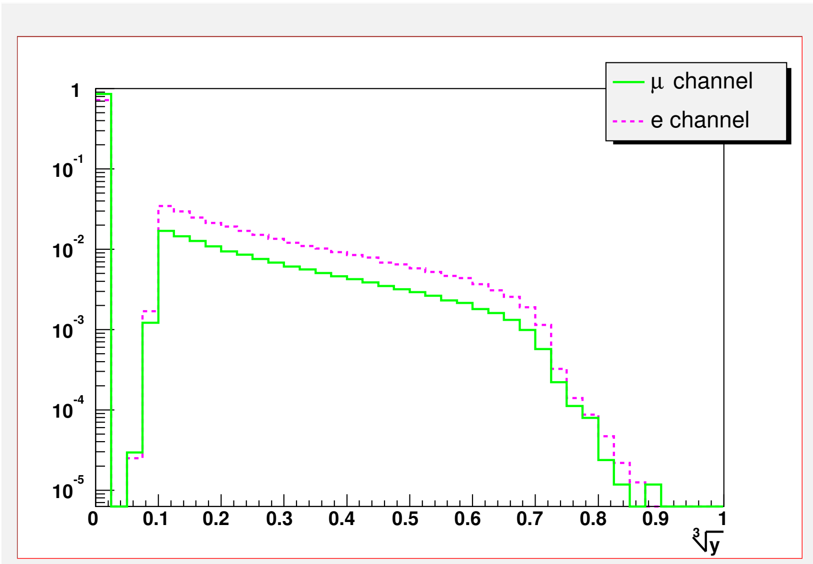

Figure 3: Projection of $\sqrt[3]{y}$ for muons and electrons. More photons are produced by WGRAD for electrons than for muons since there is more radiation collinear with the electron than the muon. The muon sample contains 17% events with a photon while the electron sample contains 31% with a photon. Events with no photon are in the zero bin.

effects into the lineshapes of the mass fitting templates. We use FSR using the Berends and Kleiss approximation in running WGRAD. The largest QED systematic is from a second final-state photon, which is not modelled in WGRAD.

2.3 QCD Radiation/$p_T(W)$ model

The W p_T spectrum has a large impact on the lineshapes of the fit and is thus a key ingredient to the W mass measurement. We model this spectrum using RESBOS, which computes the quintuple differential cross section $\frac{d^5\sigma}{dQ_T^W\, dy_W\, dQ_W^2\, d\Omega}$ for $p\bar{p} \to W^\pm$. RESBOS is superior to other event generators in that it models the W p_T spectrum well at low p_T via multiple-soft-gluon resummation techniques, and it contains several of the most important helicity amplitudes for W production. The helicity amplitudes influence the angular distributions of the final-state leptons at higher p_T.

The production cross section is given by the partonic cross section convoluted with the parton distribution functions. In the momentum-space calculation of the partonic cross section the non-perturbative physics is described by three parameters that must be determined from experiment. Conventionally these parameters are called g_1, g_2, and g_3. The other free parameter in the model is Λ_{QCD}. However, since Λ_{QCD} is fixed by the choice of PDF we

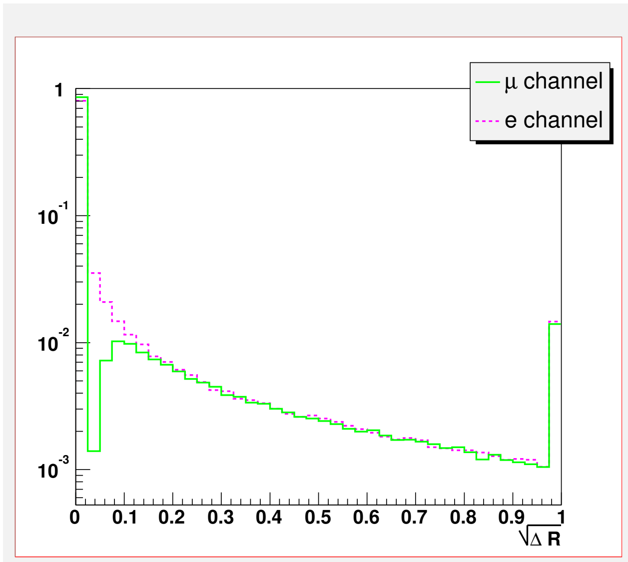

Figure 4: Projection of $\sqrt{\Delta R}$ for muons and electrons. Here we can see that the electrons contain significantly more collinear photons than the muons. The wide angle radiation is nearly identical between the two. Events with no photon are in the zero bin. Events with $\Delta R > 1$ are in the far right hand bin.

focus solely on the impact of the parameters g_1, g_2, and g_3. Previous analyses have shown that the dominant effects on the $p_T(W)$ spectrum come from changes in g_2 and Λ_{QCD} [7], where increases in g_2 tend to increase the mean boson p_T (Figure 5).

To determine the systematic uncertainty from modelling the W p_T spectrum, we first construct templates with RESBOS and parameter values obtained from a global fit to low-energy Drell-Yan and Tevatron Run 1 Z data [9]:

$$\begin{aligned} g_1 &= 0.21 \text{ GeV}^2 \\ g_2 &= 0.68 \text{ GeV}^2 \\ g_3 &= -0.60 \end{aligned}$$

We then use as data events generated with $M_W = 80.45$ GeV and various g parameters. We take the W p_T systematic corresponding to a g_2 variation of 0.12, leaving g_1 fixed. This variation agrees with that of [10], which also shows that g_1 and g_2 are 100% anti-correlated at a fixed Q value. Thus, varying g_2 by 0.12 [20] is equivalent to varying g_1 by a similar amount. In addition, following [10] we vary g_3 by ± 0.3. The systematic uncertainties extracted from these variations are shown in Table 4.

	Systematic (MeV)		
Source	Muon	Electron	Common
Simulation/Fitter	5	5	5
ISR/Interference	5	5	5
δ_s	5	5	-
Second photon	15	10	10
FSR vs. FSRBK	5	5	5
Sampling histogram	5	-	-
Total QED	20	15	13

Table 3: Summary of QED and fitter systematics for the mass fit in the muon and electron channels. We take the uncertainties to be the same for the three fit distributions.

	Systematic (MeV)		
Parameter Range	p_T	m_T	$\not\!\!E_T$
$g_2 \pm 0.12$ GeV^2	22	7	11
$g_3 \pm 0.3$	16	11	14
Total QCD/W p_T	27	13	18

Table 4: Systematic uncertainties due to varying the g parameters in RESBOS about their nominal values. We combine muons and electrons and take the uncertainties to be common to both. The numbers include a statistical uncertainty of ~ 4 MeV.

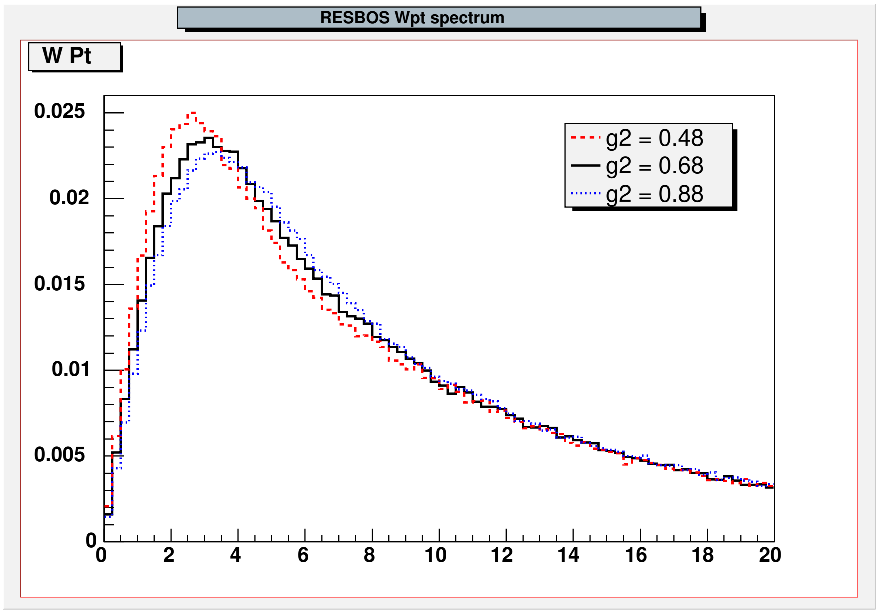

Figure 5: W p_T spectrum generated by RESBOS for various g_2 values. The mean W p_T increases with increasing g_2.

2.4 Proton Parton Densities

Parton distribution functions (PDFs) enter into the W mass measurement through their effects on the detector acceptance and kinematics of the decay charged lepton. The PDF constraints are obtained from global fits to many data sets such as deep inelastic scattering, jet production and W charge asymmetry. There are two major groups that provide semi-regular updates to parton distributions when new data or theory becomes available, namely the MRST and CTEQ collaborations.

The CTEQ6 PDF allows 20 free parameters in the global fit to the data and uses a Hessian method, where a 20×20 matrix is diagonalized and 20 orthogonal eigenvector directions in parameter space are determined. Each eigenvector direction corresponds to some linear combination of PDF parameters. From these eigenvectors are constructed 40 uncertainty PDFs varying by $\pm\Delta\chi^2$ of 100, which is meant to correspond to 90% CL. To obtain the variation due to the 40 uncertainty PDFs, 40 million events are generated in PYTHIA for each PDF employing an interface to the PDFs in ROOT [11]. A MC template generated with the central CTEQ6 PDF (CTEQ6M) is then used to obtain the best fit for each uncertainty PDF. After simulating the detector acceptance and response, we obtain the variation of the 40 CTEQ6 error PDFs compared to the fit result of the CTEQ6M PDF (Figure 6).

To estimate the PDF systematic uncertainty on a given measured quantity, the CTEQ collaboration provides a formula to compute the uncertainty corresponding to 90% CL. To

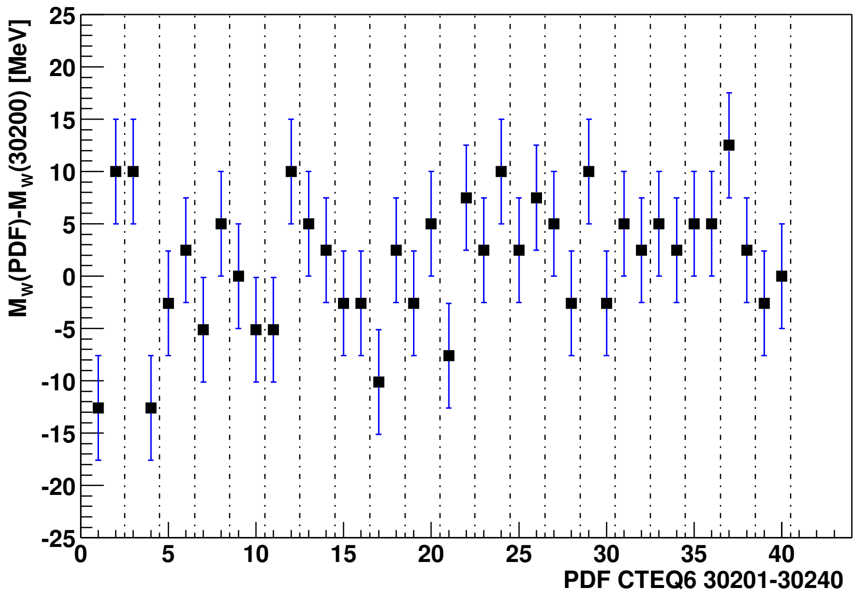

Figure 6: Difference between the simulated m_T mass fit for each of the 20 CTEQ PDF uncertainty pairs and the default PDF (CTEQ6M, or CTEQ6 30200).

obtain a 1σ systematic uncertainty on the W mass, we divide this formula by a factor of 1.6:

$$\text{CTEQ6 `}1\sigma\text{' uncertainty} = \tfrac{1}{2}\sqrt{\Sigma_i(\Delta M_W(+)_i - \Delta M_W(-)_i)^2}/1.6 = 15 \text{ MeV},$$

where $\Delta M_W(\pm)_i$ corresponds to the measured mass difference between the CTEQ6M template and the $\pm\Delta\chi^2 = 100$ PDF data, for a given eigenvector i.

The latest PDF from the MRST collaboration (MRST2003) is found to fit well within the CTEQ6 error band. Generating 40 million events using the MRST2003 PDF and fitting the obtained transverse mass distribution with the CTEQ6M template, we find an 8 MeV difference with respect to the CTEQ6M fit. This falls well into the 15 MeV uncertainty found by the CTEQ6 method. A systematic uncertainty of 15 MeV on the W mass for the M_T fit due to the PDF choice is therefore determined. Performing the analogous analysis for the p_T and $\not{E}_T$ fits, we find systematic uncertainties of 18 MeV and 19 MeV, respectively.

3 Detector Simulation

We simulate the tracker and calorimeter response, and the muon acceptance, using a fast detector simulation. The simulation is capable of reading in vector files containing 3-momentum and vertex information of electrons, muons, photons and neutrinos, simulate all relevant detector effects, and produce histograms of kinematic quantities. In this section we describe the detector effects in our simulation and our parametrisations. We will return to the constraints on these parameters in sections 5 and 7.

3.1 Simulation of Passive Material

The effects of passive material on electrons, muons and photons are important for this analysis. For muons we are interested in the ionization energy loss, and for photons the conversion process $\gamma \to ee$. For electrons the bremsstrahlung process $e \to e\gamma$ is most relevant, though we simulate their ionization energy loss as well. In addition, multiple coulomb scattering for electrons and muons is simulated in order to incorporate its effect on resolution.

The passive material of the COT inner wall and inside it is represented by a 3D lookup table called "Silimap" [12], which stores the material properties in a finely binned 3D histogram vs (r, ϕ, z). Silimap is created by scanning the full detector geometry as implemented in cdfSim. Three material properties are stored in Silimap:

1. the number of radiation lengths x_0, needed for evaluating the bremsstrahlung and conversion probabilities
2. the normalization constant needed for evaluating the Bethe-Bloch formula for ionization energy loss
3. the ionization constant needed for evaluating the Bethe-Bloch formula

3.2 Tracker Simulation and Reconstruction

We simulate the COT tracks associated with electrons and muons using a hit-level simulation. These particles are propagated along a helical trajectory from the production point, stepping through the layers of passive material represented in Silimap. At the intersection with each layer, the number of radiation lengths $x_0(r, \phi, z)$ is used to deflect the particle according to the predicted amount of multiple coulomb scattering. The particle energy is reduced by the ionization energy loss predicted by the Bethe-Bloch formula.[1] For electrons, the probability of radiating a bremsstrahlung photon is evaluated, and radiated photons are produced collinearly with the electron with the bremsstrahlung energy spectrum. The electron energy is reduced correspondingly. The total conversion lengths along the photon flight path, starting at the emission point, are evaluated and used to compute the photon conversion probability. If the photon is converted, the conversion electrons are propagated to the calorimeter as helices.

The COT active volume contains simulated wires placed at the appropriate radii and stereo angles. Hits are digitized and smeared according to a gaussian [13] with resolution

[1] The full Bethe-Bloch formula is implemented, including the density effect.

determined by muons from J/ψ or Z decays. Based on the distribution of the number of COT hits on data tracks, the single-hit efficiency is tuned to be ϵ_1 for a fraction h_1 of the tracks and ϵ_2 for the rest of the tracks. The hit resolution r_1 is used for a fraction R_1 of the tracks and the hit resolution r_2 is used for the rest of the tracks.

The smeared hits are fit with a helix to obtain the fitted track parameters [13]. The latter are used to compute the fitted track kinematics. The simulation also has the option of beam-constraining the fitted track, where the beam position $(x = 0, y = 0)$ is included in the track fit. The transverse momentum is obtained from the curvature using $p_T = 0.00211593/|c|$.

3.3 Calorimeter Response

The response of the calorimeter to the hadronic recoil is described by a response function R, which scales the true recoil magnitude to simulate the measured magnitude. The response function is parameterized as

$$R \equiv u_{rec}/u_{true} = a + b \cdot r - c \cdot r^2, \tag{3}$$

where $r = u_{true}/100$ GeV, and a, b, c are positive constants to be fit to the data. This function describes an inverted parabola. When $r > b/(2c)$ the function R becomes non-monotonic, which we consider to be an unphysical representation of the detector response; we therefore fix R to its maximum value for $r > b/(2c)$. The hypothesis that R becomes constant at high u_{true} is confirmed from cdfSim by plotting $|\vec{u_{rec}} \cdot \hat{u_{true}}|/u_{true}$ vs u_{true} for W events generated with PYTHIA.

The recoil resolution is assumed to have two components, which are summed vectorially: a "sampling" term representing the calorimeter "jet" resolution, and an underlying event component in a random direction. The sampling resolution is parameterized as $s_{had} \cdot \sqrt{u_{true}}$. The underlying event contribution is represented by a random vector (e_x, e_y), given by

$$e_i = A_i + B_i \cdot \Sigma E_T \oplus \sigma_i(\Sigma E_T) \tag{4}$$

The mean values of e_x and e_y are separately parameterized as linear functions of ΣE_T, from minimum-bias data. The minimum-bias data are chosen to have the same distribution of instantaneous luminosity as the W data. e_x and e_y are also independently fluctuated with Gaussian random variables, with the r.m.s. given by σ_x and σ_y respectively. The latter are parameterized as power-law functions of ΣE_T using the same minimum-bias data.

We obtain the results $A_x = 0.073, B_x = 0.00566, A_y = 0.007, B_y = 0.01576$, and $\sigma_x = 0.3887 \cdot (\Sigma E_T)^{0.5216}$, $\sigma_y = 0.367 \cdot (\Sigma E_T)^{0.5342}$.

The distribution of ΣE_T is obtained from the same minimum-bias data,

$$P(\Sigma E_T) = (\Sigma E_T)^{0.323} \cdot e^{-(\Sigma E_T)/25.18} \tag{5}$$

However, this ΣE_T distribution is not a complete representation for W and Z events, because of the difference in n, the mean number of interactions at the same instantanous luminosity. Defining the instantanous luminosity at which $n = 1$ for zero-bias events as L_1, we have

$n_{ZB} = L_{MB}/L_1$, and $n_{MB} = n_{ZB}/(1 - e^{-n_{ZB}})$. Furthermore, $n_{W,Z} = N_{W,Z} + L_{W,Z}/L_1$, where $N_{W,Z}$ represents the effective number of minimum-bias interactions in the hard collision. We define a minimum-bias scale factor $\alpha_{MB}^{W,Z} = n_{W,Z}/n_{MB}$, and use it to scale the ΣE_T value generated according to Eqn. 5 to obtain a more realistic simulation of ΣE_T.

The measured values of the mean instantaneous luminosity (in units of $10^{31}/\mathrm{cm}^2/\mathrm{s}$) are $L_1 = 3.3$, $L_W = L_Z = 2.11$ and $L_{MB} = 2.02$.

3.4 Muon Acceptance Modelling

The acceptance of the muon detectors is extracted from the cdfSim geometry using the Fake-Event generator. Single muons are propagated through the detector, reconstructed, and the probability of identifying the reconstructed muon in the CMUP and the CMX detectors is evaluated as a function of ϕ, $\cot\theta$ and z_0. We find that the variation with z_0 is small over the luminous region of the beam, and neglect this dependence. We also find little correlation between the ϕ and $\cot\theta$ dependences. We create 1D histograms to use as lookup tables to evaluate ϵ_ϕ^{CMUP}, $\epsilon_{\cot\theta}^{CMUP}$ and ϵ_ϕ^{CMX}, $\epsilon_{\cot\theta}^{CMX}$.

To increase the event-generation efficiency, we renormalize the ϵ_ϕ^{CMX} and $\epsilon_{\cot\theta}^{CMX}$ maps such that the maximum efficiency in any bin is unity. In order to match the ratio of CMUP and CMX W candidates observed in the data, we renormalize the ϵ_ϕ^{CMUP}, $\epsilon_{\cot\theta}^{CMUP}$ maps such that the maximum efficiency in any bin is 0.84. The muon identification efficiency is evaluated in the simulation using the following relation:

$$\epsilon^\mu(\phi, \cot\theta) = \epsilon_\phi^{CMUP}(\phi) \cdot \epsilon_{\cot\theta}^{CMUP}(\cot\theta) + \epsilon_\phi^{CMX}(\phi) \cdot \epsilon_{\cot\theta}^{CMX}(\cot\theta) \tag{6}$$

In addition, we make the muon fiducial cuts: $|z_{cal}^\mu| < 230$ cm and $|z_{SL7}^\mu| < 155$ cm. The comparison between the data and simulation muon cosec θ distributions from W events is shown in Fig. 7.

3.5 Electron Acceptance Modelling

Fiducial electrons are defined by: 12 cm $< |z_{cal}^e| <$ 230 cm, $|z_{SL7}^e| <$ 155 cm and $|z_0| <$ 60 cm.

3.6 Efficiency Modelling

We simulate the track trigger efficiency as a function of η. We simulate the electron and muon finding efficiencies as functions of $u_{||}$.

3.7 Underlying Event

The transverse recoil $\mathbf{u}$ is measured by summing all calorimeter towers in the event, excluding lepton towers. We use W data to measure the underlying-event energy in the lepton towers [14]. Figure 9 shows the spatial distribution of the mean E_T per tower in the vicinity of the

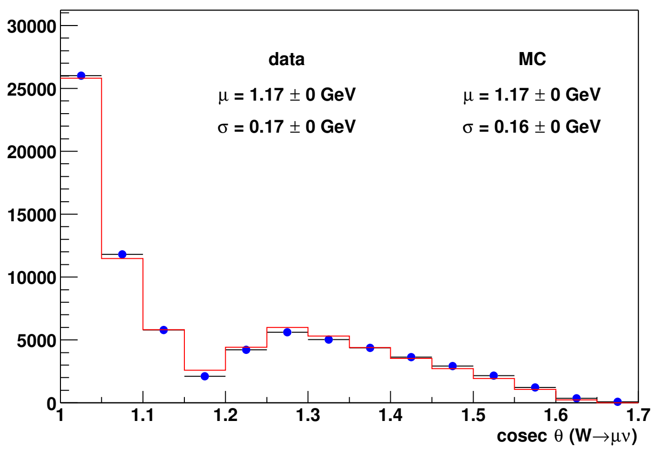

Figure 7: The comparison of data and simulation cosec $\theta(\mu)$ distributions from $W \to \mu\nu$ events.

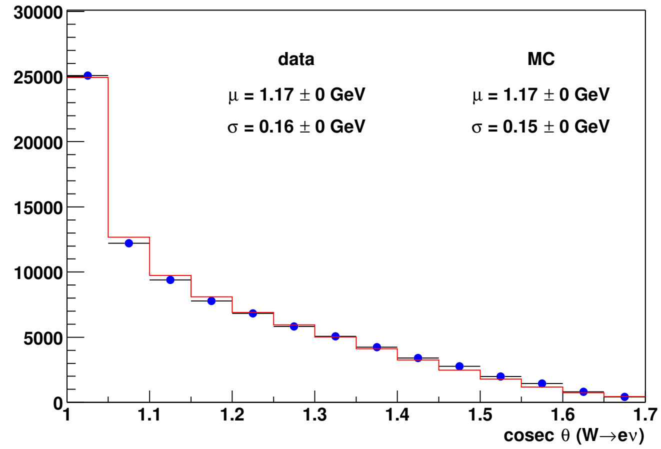

Figure 8: The comparison of data and simulation cosec $\theta(e)$ distributions from $W \to e\nu$ events.

muon track in $W \to \mu\nu$ data. Based on these distributions we remove the three indicated towers around the muon track. We measure the underlying event transverse energy (E_T^{ue}) in these towers using equivalent towers separated by two or more towers in ϕ. The predicted distribution of $\log_{10} E_T^{ue}$ in the removed muon towers is shown in Fig. 10, and the variation of $< E_T^{ue} >$ with η, $u_{||}$ and $u_\perp$ is shown in Figs. 11-13, respectively. We include the variation with η and $u_{||}$ in our simulation, but not the variation with $u_\perp$.

The same study is also done for electrons. Figure 14 shows the spatial distribution of the mean E_T per tower in the vicinity of the electron seed tower in $W \to e\nu$ data. Based on these distributions we remove the seven indicated towers around the electron seed tower. We measure the underlying event in those towers using equivalent towers separated by 3, 6, 9, or 12 towers in ϕ. The predicted distribution of $\log_{10} E_T^{ue}$ in the removed electron towers is shown in Fig. 15, and the variation of $< E_T^{ue} >$ with η, $u_{||}$ and $u_\perp$ is shown in Figs. 16-18 respectively. We include the variation with η and $u_{||}$ in our simulation, but not the variation with $u_\perp$.

To assess the potential systematic uncertainties in the mass fits from removing the underlying event energy along with the electron energy (from 7 towers) and the muon minimum ionizing energy (from 3 towers), we use the variation of E_T^{ue} as a function of tower ϕ separation between the charged lepton and the measurement region. The results of these variations are shown in Fig. 19 for electrons and Fig. 20 for muons. From these plots we conclude that the variation in predicted underlying event energy in the removed electron (muon) towers is 15 (10) MeV/c^2. Since this correction is made at *exactly* the ϕ of the charged lepton, it is a direct uncertainty on $u_{||}$ and hence on the transverse mass. We take these variations to be the systematic uncertainties on the m_T fits, twice the variations to be the uncertainties on the $\not\!\!E_T$ fits, and no systematic uncertainty on the charged-lepton p_T fits. These uncertainties

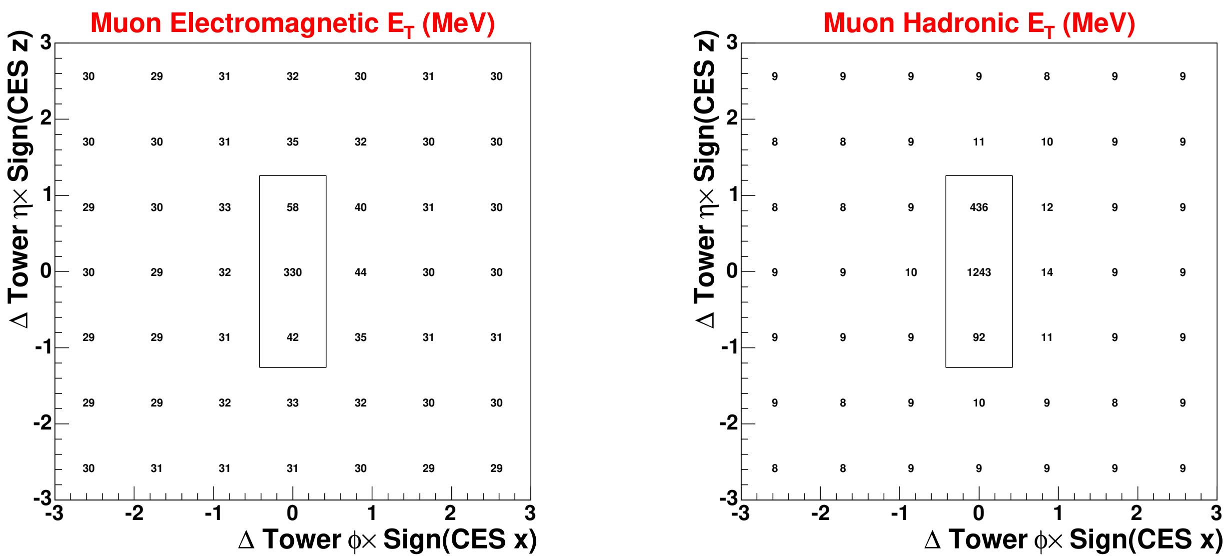

Figure 9: The mean E_T per EM (left) or HCAL (right) tower in the vicinity of the muon track. Here CES z is local to the tower: positive CES z is closer to the neighboring tower in the $+\eta$ direction, and vice versa for negative CES z.

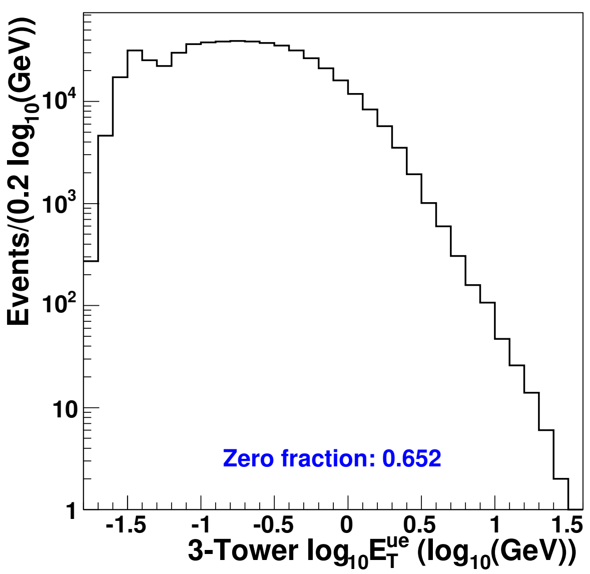

Figure 10: The predicted distribution of $\log_{10} E_T^{ue}$ in the removed muon towers. 65% of the events have $E_T^{ue} = 0$ (not shown).

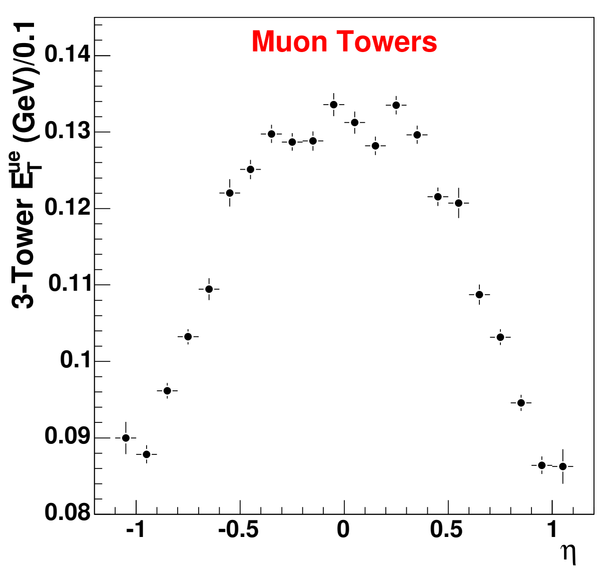

Figure 11: The predicted variation of $< E_T^{ue} >$ in the removed muon towers with η.

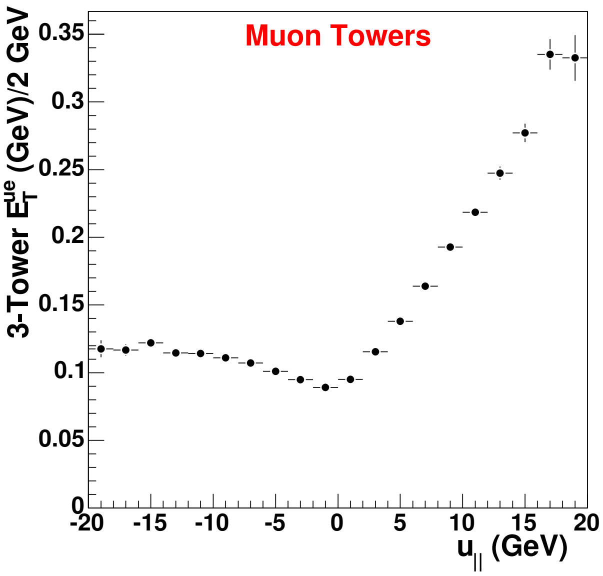

Figure 12: The predicted variation of $< E_T^{ue} >$ in the removed muon towers with $u_{||}$.

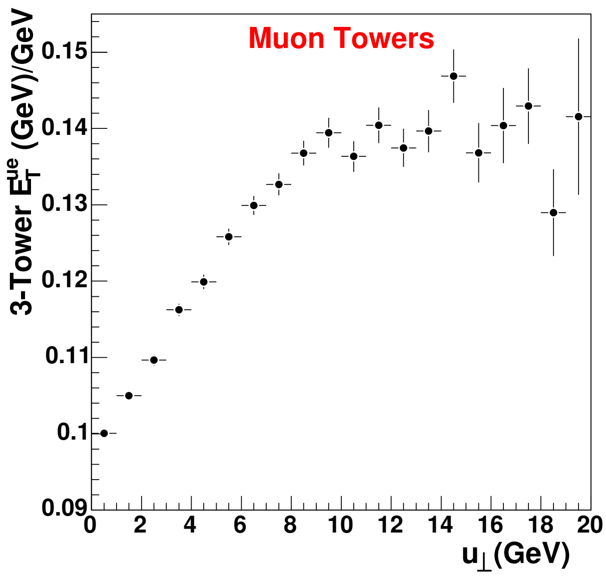

Figure 13: The predicted variation of $< E_T^{ue} >$ in the removed muon towers with $u_{\perp}$.

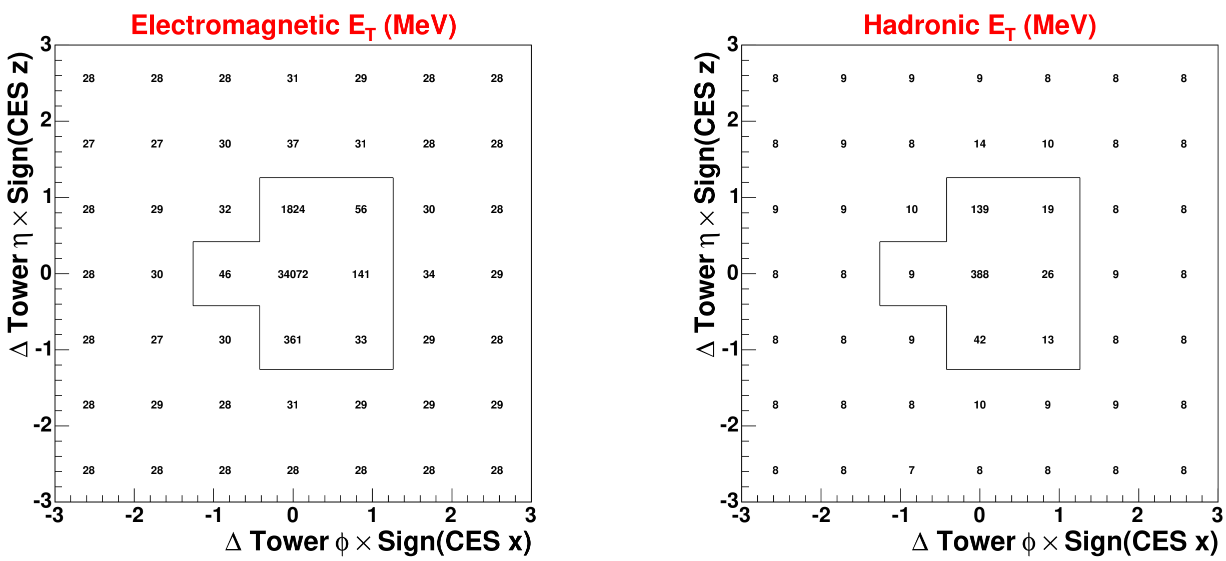

Figure 14: The mean E_T per EM (left) or HCAL (right) tower in the vicinity of the electron seed tower. Here CES z is local to the tower: positive CES z is closer to the neighboring tower in the $+\eta$ direction, and vice versa for negative CES z.

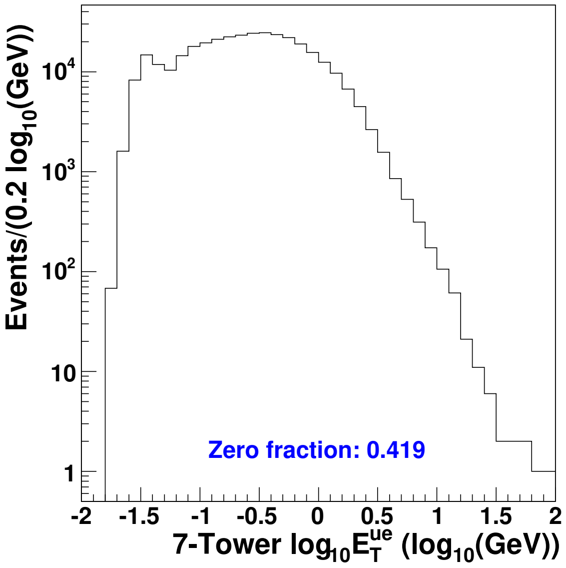

Figure 15: The predicted distribution of $\log_{10} E_T^{ue}$ in the removed electron towers. 42% of the events have $E_T^{ue} = 0$ (not shown).

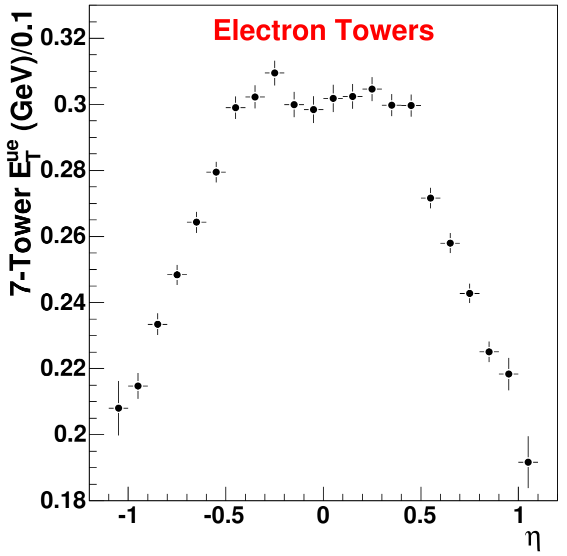

Figure 16: The predicted variation of $< E_T^{ue} >$ in the removed electron towers with η.

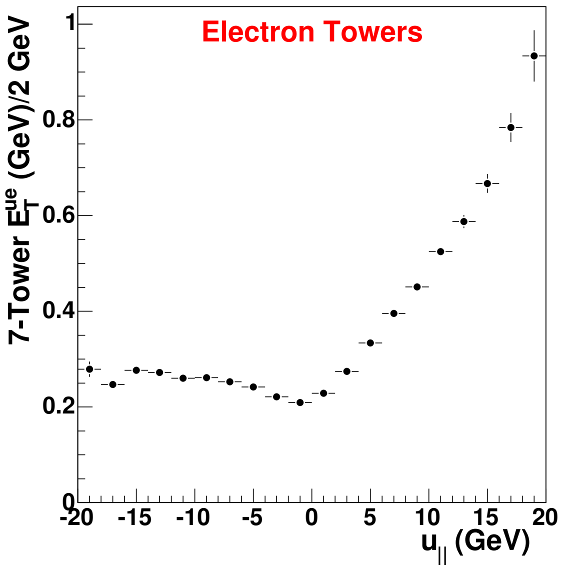

Figure 17: The predicted variation of $< E_T^{ue} >$ in the removed electron towers with $u_{||}$.

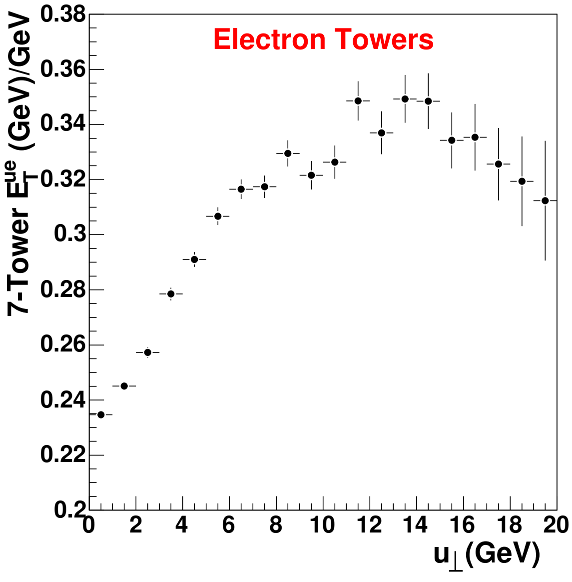

Figure 18: The predicted variation of $< E_T^{ue} >$ in the removed electron towers with $u_{\perp}$.

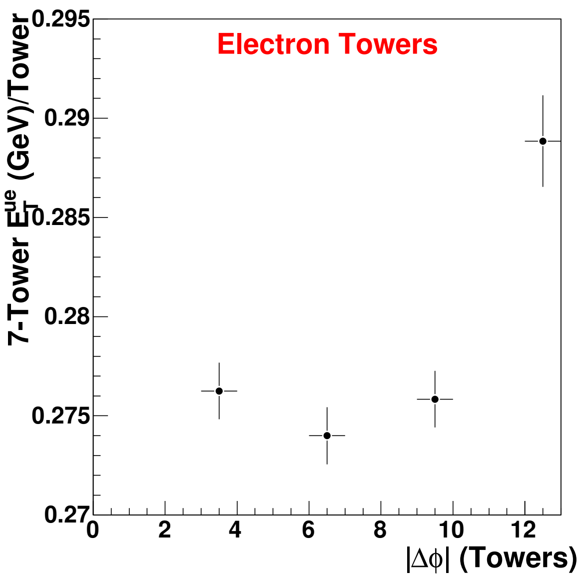

Figure 19: The mean energy in 7 towers as a function of $|\Delta\phi|$ between the electron and the measurement region.

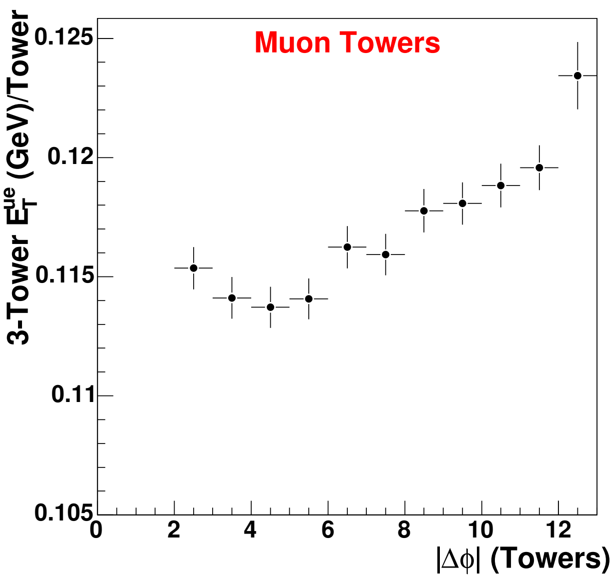

Figure 20: The mean energy in 3 towers as a function of $|\Delta\phi|$ between the muon and the measurement region.

are reported in section 9.2.

4 Event Selection

The event selection for the W mass measurement consists of four components: data set definition; trigger selection; lepton identification; and kinematic selection. The selection produces high-purity W samples that are amenable to simulation, and Z calibration samples with negligible background.

In addition to the selections discussed below, we define our W samples with the following kinematic ranges: $50 < m_T < 100$ GeV, $25 < p_T(l) < 55$ GeV, and $25 < \not\!\!E_T < 55$ GeV. The selection criteria described here yield the event samples listed in Table 5.

4.1 Electron Channel

The electron identification (Table 6) includes Δz, L_{shr}, and Had/EM requirements, due to the trigger selection and the EM cluster definition. We additionally apply a well-simulated E/p requirement to improve background rejection. Finally, we make tight track-quality requirements to aid the simulation of the electron track.

The $\not\!\!E_T$ requirement in the W selection suppresses $Z \to ee$ events where both electrons are measured in the calorimeter. To suppress the background where one electron goes into

Sample	Candidates
$W \to e\nu$	87873
$W \to \mu\nu$	71056
$Z \to e^+e^-$	3364
$Z \to \mu^+\mu^-$	5010

Table 5: W and Z event samples for 218 (191) pb^{-1} of high-p_T electron (muon) CDF-II data.

Component	Requirement
Trigger	ELECTRON_CENTRAL_18
Identification	Electron $E_T > 25$ GeV Track $p_T > 15$ GeV $L_{shr} < 0.3$ $\lvert\Delta z\rvert \leq 5$ cm $E/p \leq 2$ Had/EM ≤ 0.1 ≥ 3 axial SL's with ≥ 5 hits ≥ 3 stereo SL's with ≥ 5 hits Detector $\lvert\eta\rvert < 1$ Cluster $\lvert$CES $x\rvert < 18$ cm Fiducial CEM (cluster-based)
Kinematic (W)	$\mathbf{u}$<20 GeV $\not{E}_T > 25$ GeV Exactly 1 identified electron No oppositely-charged track with all of: $p_T > 20$ GeV $\lvert$CES $x\rvert > 22$ cm or $\lvert$CES $z\rvert < 6$ cm Calorimeter isolation < 0.1 $\lvert d_0\rvert < 0.2$ cm
Kinematic (Z)	Exactly 2 identified electrons Electrons have oppositely-charged tracks

Table 6: The $W \to e\nu$ and $Z \to ee$ event selection criteria for the W mass measurement.

a calorimeter crack, we remove events with an additional oppositely-charged, isolated, high-p_T track in the crack region. The number of W events removed is negligible, as there are only 7 same-sign candidates passing this selection (4 of these candidates have dilepton mass between 81 GeV and 101 GeV).

We estimate the purity of the Z calibration sample by taking the ratio of the number of same-sign events to opposite-sign events. This ratio is 1.3%, and we expect the majority of the same-sign events to be real electrons with the wrong sign caused by bremsstrahlung and subsequent conversion.

4.2 Muon Channel

The $W \to \mu\nu$ event selection starts with the two highest-p_T tracks in the event. If the two tracks are not rejected according to the Z identification listed below, the event selection continues by identifying which of the two selected particles pass the tight muon and track cuts. The event is vetoed if it is consistent with the presence of a cosmic ray [15]. Additional event selection restricts the observed recoil activity and muon-corrected missing transverse energy in the calorimeter. The $Z \to \mu\mu$ calibration sample consists of pairs of identified muons, at least one of which has an associated stub.

We list the muon and track identification and event selection below, as well as the `dukehkg` [16] ntuple accessors used for the selection.

<u>Muon Cuts:</u>

- Good run for muon systems
  `http://www-cdf.fnal.gov/internal/physics/ewk/Wmass/godparents/goodrun_cmupcmx_wmass.txt`
- Fiducial stub in CMU and CMP or CMX
  `MU_mu_fidCMU[muon], MU_mu_fidCMP[muon], MU_mu_fidCMX[muon]`
- $|\Delta x| < 3$ cm (CMU), < 5 cm (CMP), < 6 cm (CMX)
  `MU_mu_dx[muon][0], MU_mu_dx[muon][1], MU_mu_dx[muon][2]`
- Triggered muon
  CMUP: `GLB_L3_MUON_CMUP18 && GLB_L1_CMUP6_PT4 &&`
  `(GLB_L2_AUTO_L1_CMUP6_PT4 || GLB_L2_TRK8_L1_CMUP6_PT4)`
  CMX: `GLB_L3_MUON_CMX18`
- $E_{em} < 2+\max(0,0.0015(p\text{-}100))$ GeV
  `MU_mu_emE[muon]`
- $E_{had} < 6+\max(0,0.0028(p\text{-}100))$ GeV
  `MU_mu_hadE[muon]`

<u>Track Cuts:</u>

- 25 GeV/$c < p_T <$ 55 GeV/c
  `0.00211593 / fabs( TRACK_trk_cotbc_curv[track] )`

- track through all COT layers
  `TRACK_trk_nonbc_lastLayerCT[track]==95`
- 5 or more hits in at least 3 axial SL
  `TRACK_trk_nonbc_numHitSL[track][sl], sl uneven`
- 5 or more hits in at least 3 stereo SL
  `TRACK_trk_nonbc_numHitSL[track][sl], sl even`
- $|z0| < 60$ cm
  `TRACK_trk_cotbc_z0[track]`
- $|d0|$ (COT) < 0.2 cm (corrected for beam offset and slope)
  `COTNBC_cotnbc_d0[nbc_track]+(VERTEX_vtx_cot_beamx+COTNBC_cotnbc_z0[nbc_track]*`
  `VERTEX_vtx_cot_slopex)*sin(COTNBC_cotnbc_phi[nbc_track])-(VERTEX_vtx_cot_beamy+`
  `COTNBC_cotnbc_z0[nbc_track]*VERTEX_vtx_cot_slopey)*cos(COTNBC_cotnbc_phi[nbc_track])`

<u>Event Cuts:</u>

- not identified by cosmic tagger
  `(int(GLB_cosmic_bitword)&0x00004000)==0`
- $\mathbf{u} < 20$ GeV/c
  `see definition of` $|\mathbf{u}|$ in Sec. 3.7
- 25 GeV/c $< \not\!\!E_T <$ 55 GeV/c ($\vec{\not\!\!E_T} = -\vec{\mathbf{u}} - \vec{p_T}$)
- 50 GeV $< m_T <$ 100 GeV

<u>Z identification for rejection in W event selection:</u>

- the identified muon and the second highest p_T track pass:
  - $p_T > 10$ GeV/c
  - $E_{em} <$ 2+max(0,0.0015(p-100)) GeV
  - $E_{had} <$ 6+max(0,0.0028(p-100)) GeV
  - isolation fraction < 0.1
  `MU_mu_cR4Et[muon]/`p_T
  - opposite charge
- two identified muons

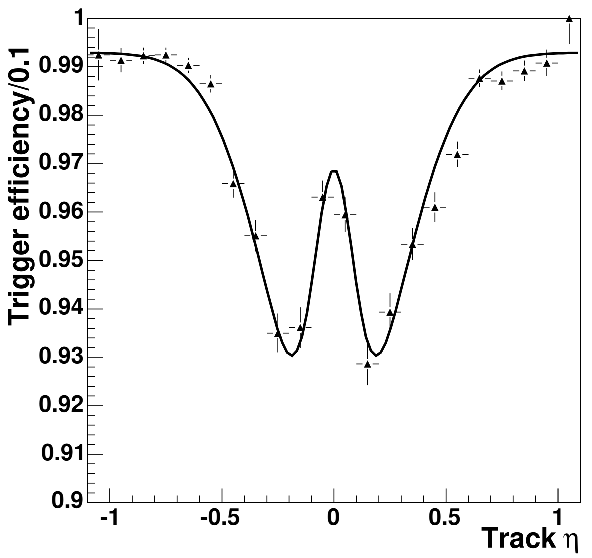

Figure 21: The trigger efficiency as a function of track η for the ELECTRON_CENTRAL_18 trigger.

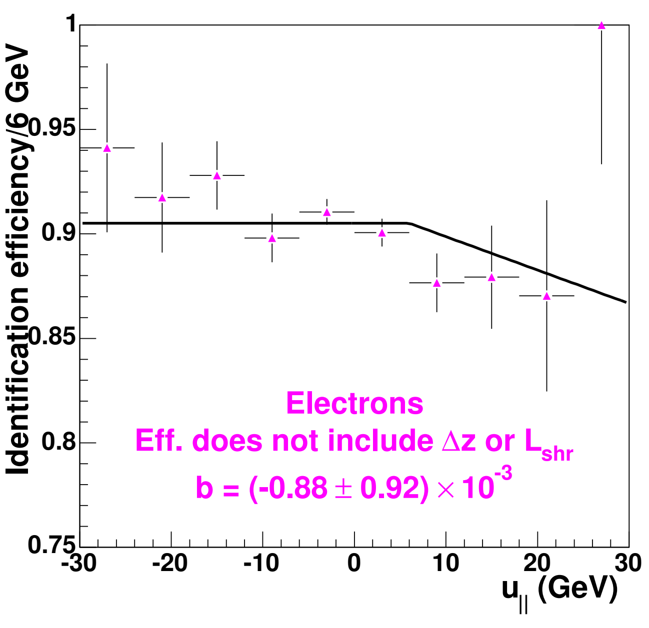

Figure 22: The variation of electron identification efficiency with $u_{||}$ measured from $Z \to ee$ candidates.

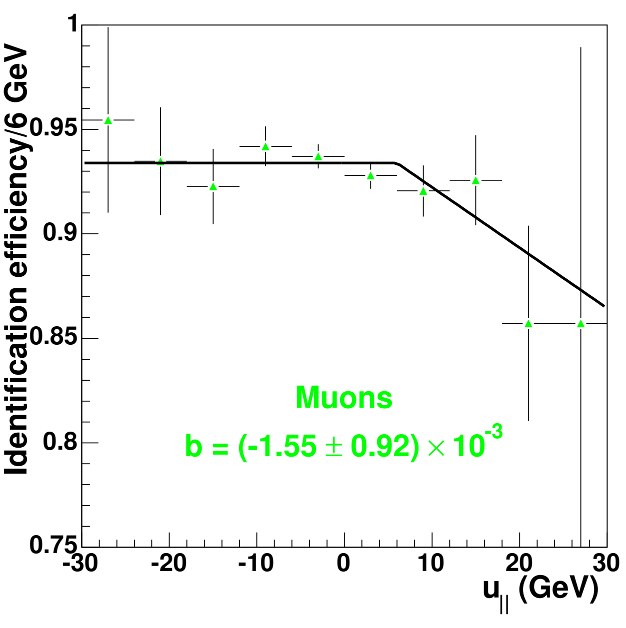

Figure 23: The variation of muon identification efficiency with $u_{||}$ measured from $Z \to \mu\mu$ candidates.

4.3 Selection Efficiencies

Event selection could cause kinematics-dependent biases [17]. These include E_T-dependence of trigger efficiency, η-dependence of track trigger efficiency, and $\vec{u}$-dependence of identification efficiency.

The trigger track requirement results in η-dependent efficiency (Fig. 21). We fit the efficiency η-dependence using a double Gaussian:

$$\epsilon_\eta = A_0 + A_1 e^{-x^2/2\sigma_1^2} + A_2 e^{-x^2/2\sigma_2^2} \tag{7}$$

The values of the fit parameters are shown in Table 7.

Parameter	Fit Value
A_0	0.993
A_1	-0.088
σ_1	0.28
A_2	0.064
σ_2	0.091

Table 7: The double Gaussian fit parameters for the trigger η efficiency. A_0 is the constant corresponding to maximum efficiency; A_1 (A_2) and σ_1 (σ_2) are the amplitude and sigma, respectively, of the first (second) gaussian.

The electron identification results in $u_{||}$-dependent efficiency (Fig. 22). We fit the $u_{||}$ efficiency using the following function:

$$\epsilon = a(1 - b((u_{||} - 6) + |u_{||} - 6|)) \tag{8}$$

The analogous plot for muons is shown in Fig. 23.
To improve the accuracy of the fit, we loosen the **u** requirement to <30 GeV. For simulating the event selection, the relevant parameter of this equation is b. With the default **u** requirement of <20 GeV, a consistent value of b is obtained.

We have studied the p_T-dependence of the muon trigger efficiency. The E_T-dependence of the electron trigger efficiency has also been studied. Both are found to be flat in our kinematic region. We have also studied the η-dependence of the muon identification efficiency, and find that it is flat within the CMUP and CMX respectively. We correct for global efficiency differences between CMUP and CMX by adjusting their relative acceptance.

5 Lepton Energy Calibration and Resolution

The detector calibration consists of tracker calibration and alignment, a run-dependent calorimeter energy scale, and validation/tuning of the passive material geometry.

5.1 Passive Material Geometry

As mentioned before, the passive material in the detector is simulated using the Silimap as a lookup table. The current version of Silimap is based on the geometry in the 5.3.1 release.

We validate and tune the passive material map using muons from cosmic rays and $J/\psi \to \mu\mu$ events. These measurements are sensitive to the ionization energy loss incurred by muons. We separately tune the number of radiation lengths using the tail of the E/p distribution of electrons from $W \to e\nu$ events. As the two mechanisms of energy loss scale differently with material properties (scale with atomic number Z for ionization energy loss and as Z^2 for the number of radiation lengths), we tune these two material properties independently.

The method for tuning the ionization energy loss is described in detail in CDF note 6351. The cosmic rays are used to directly measure the energy loss by comparing the momenta of the tracks measured (by the COT) before and after passing through the silicon detector. This measurement is performed as a function of z_0, both with data and simulated cosmic rays. The difference between the data and the simulation is applied as a correction function to Silimap. Final validation of the muon ionization energy loss is performed by measuring the J/ψ mass as a function of the muon p_T, which is discussed below.

The method of tuning the radiation lengths is to use photon conversions to map the radial and z-dependence as outlined in CDF note 6905. The final tuning of the absolute amount of material is done using the E/p tail fraction. Figure 24 shows the agreement between the tail fractions of the E/p distribution in two ranges. The variable S_{mat} is a scale factor applied to the tail fraction in the simulation, which is tuned using a maximum likelihood fit. By scaling the radiation lengths from 5.3.1 Silimap globally by 1.045, we achieve agreement with the data. We also use this fit to quantify the uncertainty in the radiation length scale factor. By scaling the fitted uncertainty by $\sqrt{\chi^2}$ of the fit, we obtain the shape uncertainty. This procedure is equivalent to taking half the difference between the second bin and the third bin, which correspond to different tail fractions, as the measure of the systematic uncertainty. QCD background also contributes a smaller uncertainty:

$$S_{mat} = 1.006 \pm 0.05(\text{shape}) \pm 0.01(\text{QCDbackground}) \tag{9}$$

The uncertainty in the amount of passive material is propagated to the uncertainty in the energy scale S_E obtained from the fit to the peak of the E/p spectrum. This is discussed in Sec. 6.1.

5.2 COT Alignment

Internal alignment of the COT is performed using a large sample of cosmic rays. Clean cosmic ray events are identified as events with one or two tracks only, of which at least one is a muon, and is tagged as a cosmic by the COT-cosmic tagger.

A single helix is fit to both tracks, and the hit residuals with respect to this ditrack are used to measure the misalignments of each cell. The $r\phi$ coordinate of each cell at the east

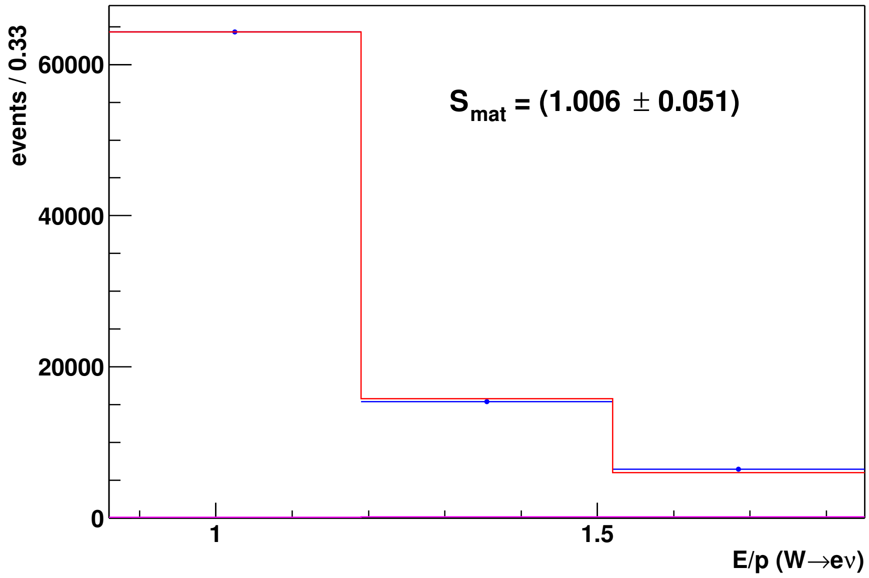

Figure 24: The fitted scale factor S_{mat} of the tail fraction of the E/p distribution from $W \to e\nu$ events. QCD background is included in the simulation templates.

and west endplate is measured separately, with a precision of $\sim 5\mu$m. The tilt angle of each cell is also measured precisely.

Collider data are used to ensure that the global (x, y) coordinates of the COT are consistent with the COT-beamline.

The details of this alignment technique and results will be described elsewhere.

In addition to the $r\phi$ alignment, a z-dependent alignment is necessary to account for wire sag and electrostatic motion. This alignment has not yet been performed using cosmic rays, so we apply a curvature correction determined using the $< E/p >$ difference between electrons and positrons from W decays [21]. We apply $\not\!\!E_T$ and E_T cuts of 30 GeV to reduce pion contamination, and we use an E/p window of $0.8 - 1.25$. The resulting correction is parametrized as a quadratic in $\cot\theta$:

$$\Delta(q/p_T) = c_0 + c_1 \cot\theta + c_2 \cot^2\theta \tag{10}$$

The parameters and their uncertainties are shown in Table 8. The difference in $< E/p >$ for positrons and electrons, before and after the correction, is shown in Fig. 25. The $< E/p >$ differences resulting from $\pm 1\sigma$ variations in the parameters are shown in Fig. 26.

We varied the coefficients c_0, c_1 and c_2 in the simulation, and fit the resulting simulated W events with the default templates. We obtain the systematic uncertainty on the W mass to be 20 MeV, due to the uncertainty in the curvature correction.

Parameter	Fit Value
c_0	-$(4.5 \pm 1.5) \times 10^{-5}$
c_1	-$(7.0 \pm 1.5) \times 10^{-5}$
c_2	$(2.45 \pm 0.25) \times 10^{-4}$

Table 8: The parameters of the coeffcients to the curvature correction function.

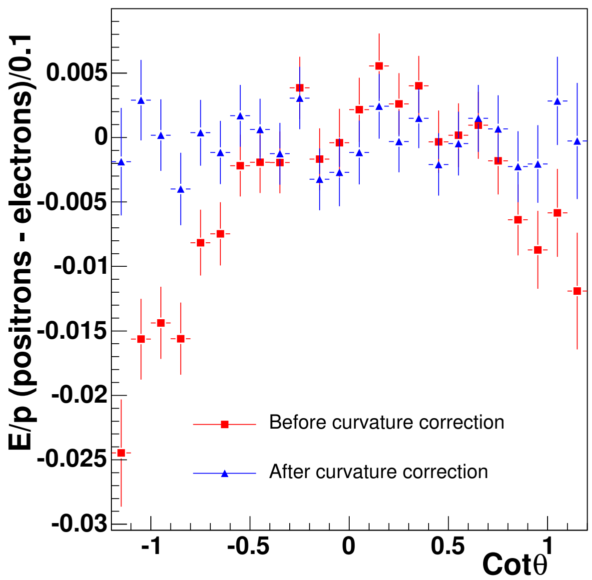

Figure 25: The difference in $< E/p >$ for positrons and electrons before (red) and after (blue) the curvature correction is applied.

5.3 COT Momentum and z Scales using $J/\psi \to \mu\mu$ Events

We simulate the J/ψ production using the `PYTHIA` generator and then simulate it with our detector simulation. More details on what goes into this simulation can be found in section 5.4.

The known J/ψ mass is used to set the COT momentum scale by performing a maximum likelihood fit to the dimuon invariant spectrum in the range $3.01 < m_{\mu\mu} < 3.15$ GeV. The background is assumed to be flat and is measured in the upper sideband $3.17 < m_{\mu\mu} < 3.31$ GeV, and included in the templates. The templates are generated as a function of the momentum scale deviation from unity $\Delta p \equiv p - 1$.

The J/ψ selection makes the following requirements on the muons;

- COT-only tracks
- 8 COT superlayers with at least 7 hits each

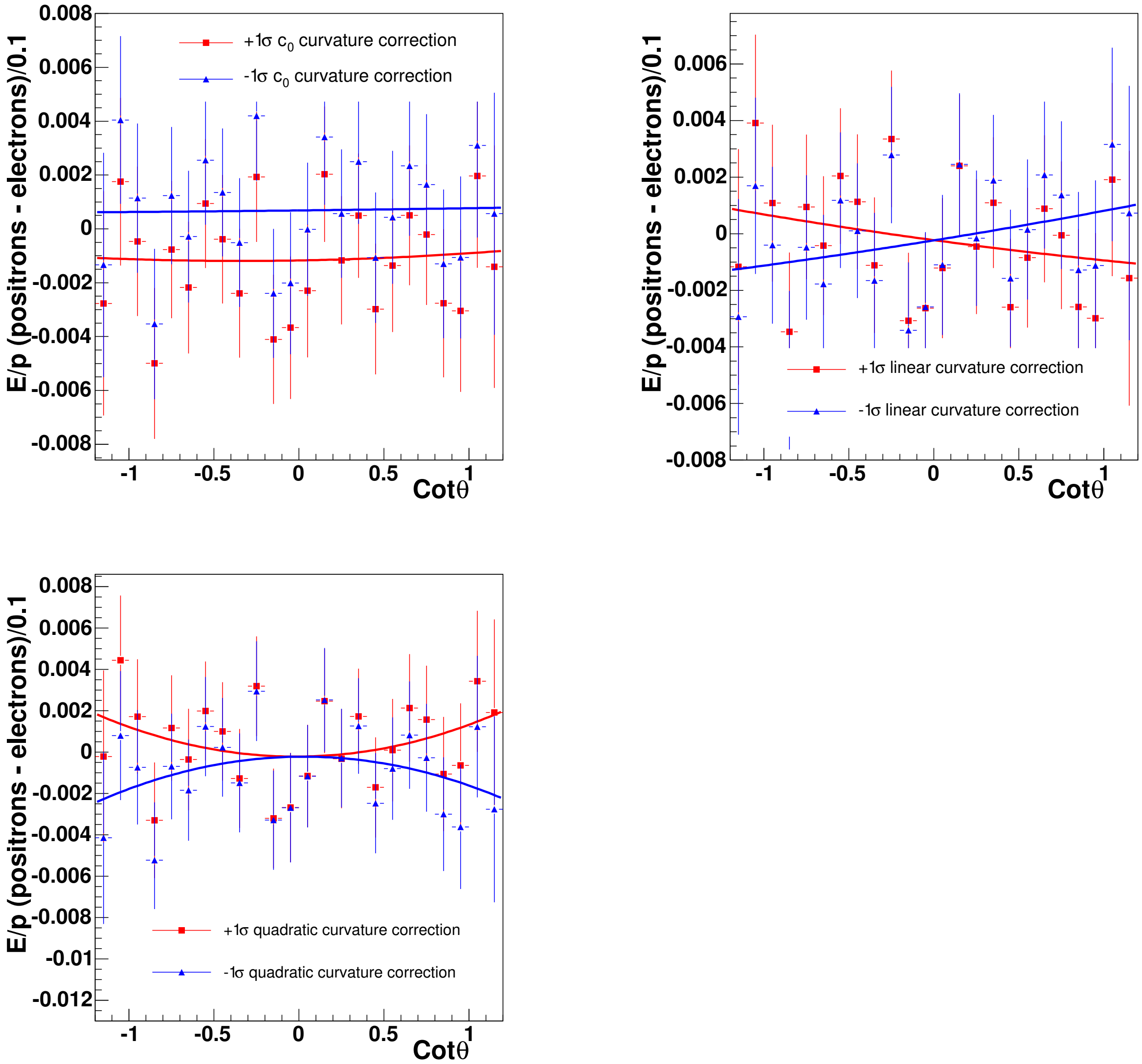

Figure 26: The effects of $\pm 1\sigma$ parameter variations on the $< E/p >$ difference between positrons and electrons.

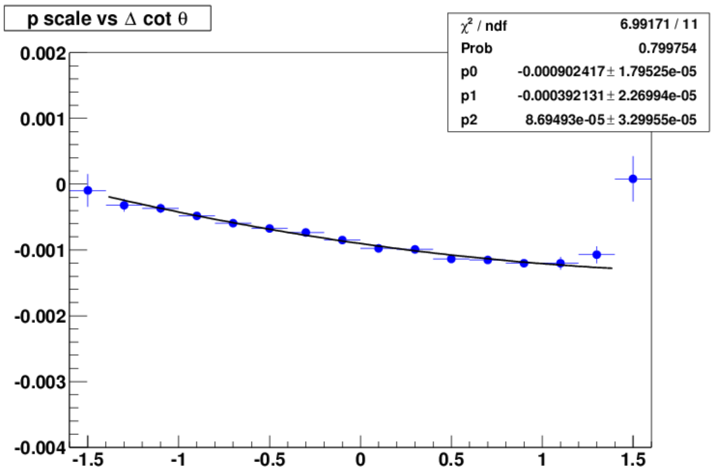

Figure 27: The fitted Δp as a function of Δ cot θ, before corrections. The fit is a parabola.

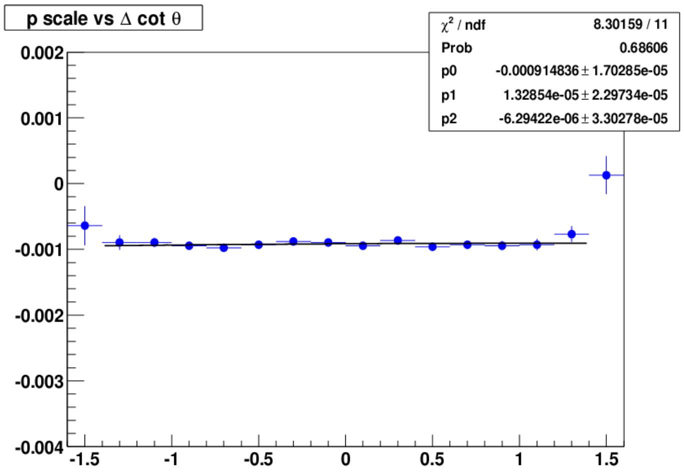

Figure 28: The fitted Δp as a function of Δ cot θ, after corrections. The fit is a parabola.

- $d_0 < 3$mm, where the d_0 is corrected to the beam spot
- $|z_0(\mu_1) - z_0(\mu_2)| < 3$ cm
- $p_t(\mu) > 1.8$ GeV

The non-beam-constrained track parameters are used to reconstruct the J/ψ kinematics.

We measure the variation of the fitted Δp with Δcot θ, the difference in cot θ between the positive and negative muon. A linear variation is induced by a relative rotation of the east and west endplates of the COT. A quadratic variation is induced by a z-scale (equivalent to a scale factor on cot θ), which can be caused by a small deviation of the stereo angles from the nominal value. Figure 27 shows evidence of both these effects.

We find that by making the following corrections to the data

$$cot\theta \rightarrow (0.9998 \pm 0.0001) \cdot cot\theta \quad (11)$$

$$c \rightarrow c - 6 \times 10^{-7} \cdot cot\theta \quad (12)$$

we eliminate both the linear and quadratic variation of the Δp with Δcot θ, as shown in Fig. 28.

The fitted $\Delta p/p$ as a function of $< 1/p_t^\mu >$ checks the simulation of the ionization energy loss. If the latter is correctly simulated, there should be no dependence. Figure 29 shows the dependence, fitted with a straight line. The extrapolated value of the $\Delta p/p$ to $< 1/p_t^\mu > \sim 0$ (relevant for W and Z bosons) is $\Delta p/p = (-1.04 \pm 0.06) \times 10^{-3}$. Averaged with the result from the $\Upsilon \rightarrow \mu\mu$ fit ($\Delta p/p = (-1.4 \pm 0.1) \times 10^{-3}$), and taking half the difference as a

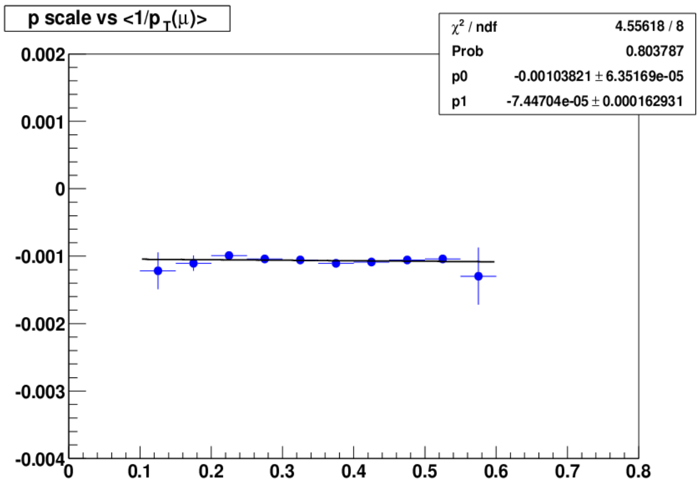

Figure 29: The fitted Δp as a function of $< 1/p_t^{\mu} >$, fitted with a straight line.

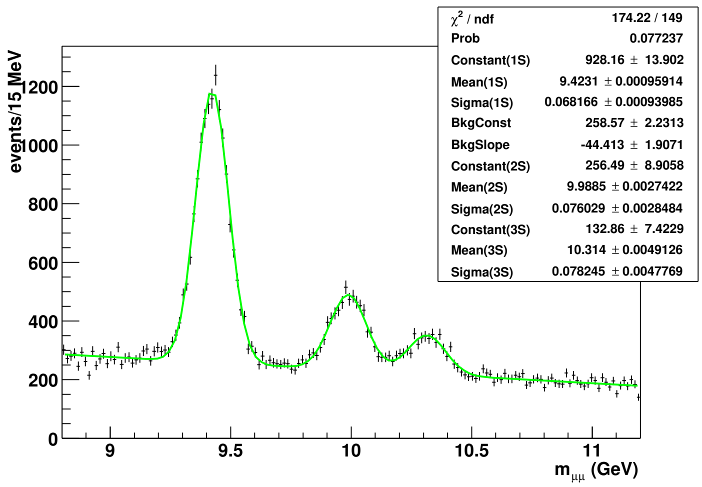

Figure 30: Dimuon mass spectrum with a fit of three Gaussians and a linear background.

systematic uncertainty, we quote the result

$$\Delta p/p = (-1.2 \pm 0.2_{\rm syst}) \times 10^{-3} \tag{13}$$

One cross-check we have been asked to perform was to look at the J/ψ mass as a function of ϕ to see if we can see any evidence of ϕ dependent calibration systematics. The result is plotted in figure 31. Although the fits in individual ϕ regions show statistically signficant fluctuations the are all compatible with the calibration and systematic uncertainty quoted in equation 13.

5.4 COT Momentum Scale using $\Upsilon \to \mu\mu$ Events

With a mass of the order 10 GeV/c^2, the Upsilon(1S) resonance supplies an intermediate reference point to study the momentum scale between the $\sim$3 GeV/c^2 J/Ψ mesons and the over nine times heavier Z^0 bosons.

Data Sample and Event Selection

We use the stripped upsilon sample from the B group `(bhmu0d)` which has been processed with the offline version 5.3.1. There are two triggers employed to select upsilon events `UPSILON_CMUP_CMU` and `UPSILON_CMUP_CMX`, requiring dimuon candidates with one muon candidate to have hits in the CMU and CMP muon detectors and the other candidate in either the CMU or in the CMX. To avoid range out of the triggered candidates the p_T cuts in the trigger are 3 GeV for CMU and CMX candidates and 4 GeV for CMUP candidates. In a

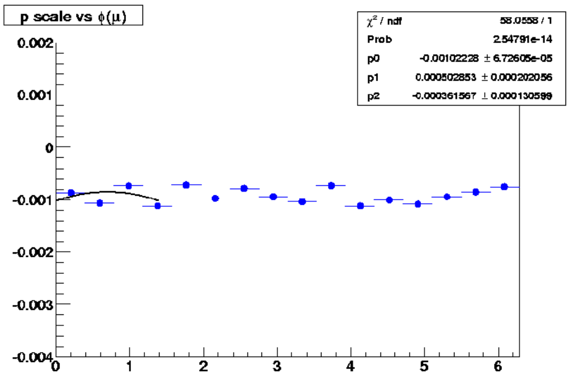

Figure 31: Fitted J/ψ mass in bins of track ϕ. The parabolic in the first few bins is an artifact and should be ignored.

similar fashion to the event selection for the J/ψ sample the following additional cuts are applied to the sample.

- $p_T > 4.2$ GeV/c for CMUP
- $p_T > 3.2$ GeV/c for CMU or CMX
- 5 or more hits in all SL's
- $\Delta z_0 < 3$ cm
- $|d0| < 0.3$ cm

The p_T cuts are chosen at a slightly larger value in comparison to the trigger cuts in order to be above the cut threshold. Figure 30 shows the dimuon mass spectrum with a fit of three Gaussian distributions added to a linear background. The three upsilon resonaces 1S, 2S and 3S are clearly visible.

Event Generation and Simulation

We use PYTHIA 6.136 to generate the kinematic variables from Υ(1S) decays which are input to the fast detector simulation described in section 3. The generator output is tuned slightly in order to better match the data.

Figure 32 and 33 show the data with Monte Carlo comparison of the Υ(1S) p_T and p_z distributions. The data is sideband subtracted for these (and all other data Monte Carlo comparisons to follow). Half of each are taken from the upper and lower sidebands. In the simulation, simple fiducial cuts are made to emulate the muon detector acceptance (acceptance map to be applied in 2nd iteration). Thus we do not know for example which of the

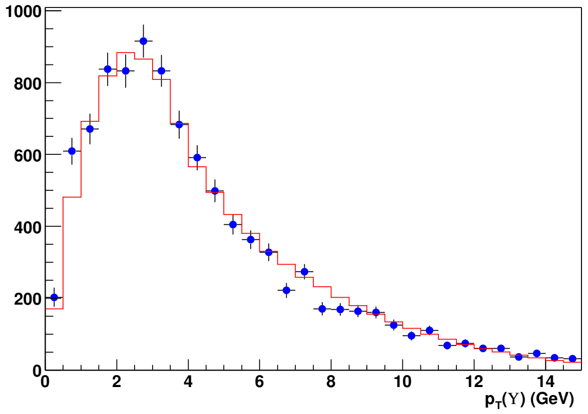

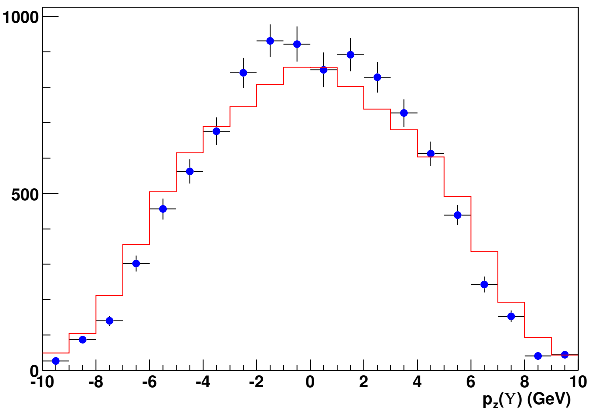

Figure 32: Comparison of data with Monte Carlo of the Υ(1S) p_T distribution.

Figure 33: Comparison of data with Monte Carlo of the Υ(1S) p_z distribution.

two muon candidates have stubs in CMU and CMP or CMU only, for which different p_T cuts are applied. To best match the data, we choose a scheme where 60% of the time it is random which generated muon gets the higher p_T cut applied. 40% of the time the muon candidate with the higher generated p_T gets assigned the higher p_T cut. The modelling of the acceptance for muons coming from the CMUP/CMX trigger is done by using crude z cuts motivated by the boundaries of the muon sub detectors. This is more straight forward compared to the CMUP/CMU(P) case since CMUP and CMX muon candidates are separated in angular acceptance. Figure 34 and 35 show the muon candidate p_T and p_z distributions comparing data and Monte Carlo. Figure 36 and 37 show data with Monte Carlo comparisons of the number of COT hits distribution and the difference in $\cot(\theta)$ distribution for the two muon candidates. The three parameters which control the binomial distributions for the hit efficiency in the simulation where set to ϵ_1=0.935, ϵ_2=0.875 and f_2=0.37 to best match the data.

Template Fits to Υ(1S) Resonance

The momentum scale is extracted in the same way as for the J/Ψ. Invariant mass templates are generated at each assumed scale and the binned log likelihod is computed. For the template generation a scale factor of 0.87 is applied in the simulation to the total ionizing material as found from the J/Ψ analysis. Since upsilons are produced only promptly we can extract the momentum scale for two invariant mass distributions, one which uses beam constrained tracks and the other one using COT tracks only, thus allowing a test for a possible systematic bias. The Υ(1S) mass signal region using beam constrained quantities is taken to be from $9.30 < M_{\Upsilon(1S)} < 9.56$ GeV and $9.26 < M_{\Upsilon(1S)} < 9.58$ GeV for the non beam

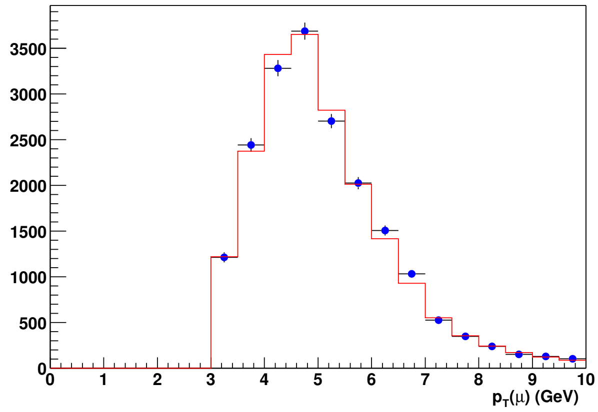

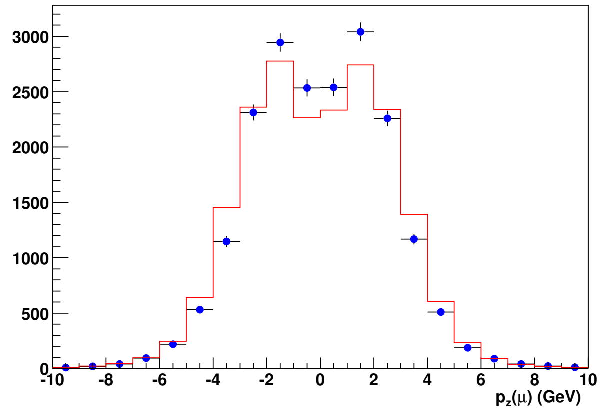

Figure 34: Comparison of data with Monte Carlo of muon candidate p_T distribution.

Figure 35: Comparison of data with Monte Carlo of the muon candidate p_z distribution.

constrained quantities. The latter one is wider due to the reduced resolution. The COT hit resolution in the simulation is tuned to best match (χ^2 minimum) the width of the dimuon mass peak. A hit width of σ=125μm is found for the non beam constrained distribution and σ=175μm for the beam constrained distribution. The curvature corrections derived from the J/ψ analysis have been applied for the upsilon invariant mass fits. Figure 38 shows the dimuon mass distribution using the non beam constraint quantities and the the best fit simulated lineshape.

Figure 39 shows the fit to the invariant mass distribution using beam constraint quantities.

A momentum scale slightly closer to unity is found, but with a smaller statistical uncertainty. The difference of the two scales is found to be $\delta(\Delta p/p)$=(0.064$\pm$0.055) 10^{-3}, where the uncertainty is computed by taking the square root of the squared differences of the two scales, representing the remaining statistical uncertainty. Applying Larry's curvature corrections [21] to the beam-constrained tracks, results in a scale of $\Delta p/p$=(-1.328$\pm$0.088) 10^{-3}. Applying the curvature correction as stated in equation 10 results in a scale of $\Delta p/p$=(-1.312$\pm$0.088) 10^{-3} thus leading to a difference of $\delta(\Delta p/p)$=(0.096$\pm$0.055) 10^{-3} compared to the non beam constraint case. The scale difference, if considered statistically significant (1.7σ), introduces a 8 MeV systematic uncertainty on the W mass.

5.5 COT Momentum Scale using $Z \to \mu\mu$ Events

We apply the COT momentum scale correction factor of 1.0012 to each of the beam-contrained muon tracks, to reconstruct the dimuon kinematics. We use $Z \to \mu\mu$ data processed with v5.3.1. We perform a maximum-likelihood fit for the measured Z pole mass,

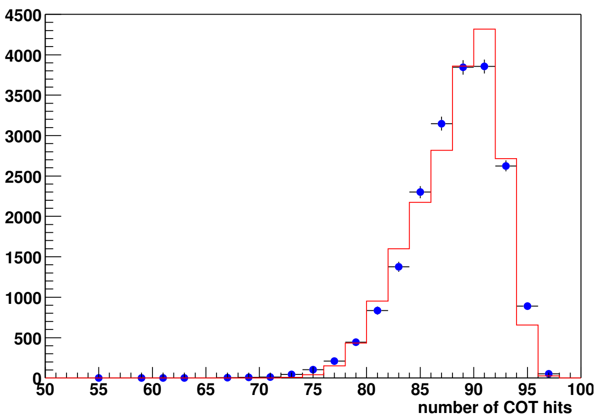

Figure 36: Comparison of data with Monte Carlo of number of COT hits distribution.

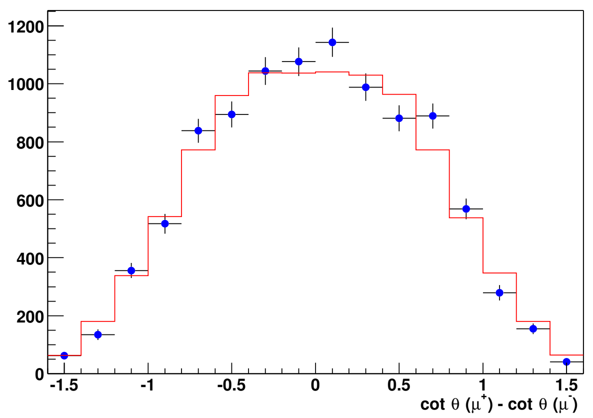

Figure 37: Comparison of data with Monte Carlo of the difference in $\cot(\theta)$ distribution.

where the fitting window is given by $84 < m_{\mu\mu} < 98$ GeV.

The templates are generates using RESBOS vector files. QED radiative corrections are implemented for FSR by sampling a 2D histogram of photon energy fraction y relative to the initial lepton energy, and ΔR between the photon and the lepton. The 2D photon distribution is generated using WGRAD.

The $Z \to \mu\mu$ mass fit is shown in Fig. 40, with the statistical error. The systematic uncertainty due to tracker momentum scale is 28 MeV, combining the uncertainties from the J/ψ and Υ analyses and the alignment corrections. We test the Z mass fitter and the QED radiative correction by generating templates with LO ZGRAD vector files [22], using the WGRAD FSR-BK histogram to produce radiative photons. We use these templates to fit simulated data, produced using ZGRAD with FSR-BK photons [22]. We find that the resulting fitted Z mass is lower than the input value by $14 \pm 4_{\rm stat}$ MeV. About half of this bias is due to the WGRAD histogram under-estimating the QED radiation off Z leptons, since the Q^2-scale is slightly higher for Z decay than W decay. We apply the 14 MeV fitter and QED bias correction with an 8 MeV systematic uncertainty for the fitter bias component, which is not yet understood. Finally, we investigate the sensitivity of the Z mass fit to the lower edge of the fit window, where we see an excess in the data. We vary the lower edge from 80 GeV to 87 GeV in 1 GeV steps, and find that the fitted mass fluctuates by ~ 5 MeV from the default value. Since this is not a monotonic variation, we attribute it to statistical fluctuations. Hence the result from the $Z \to \mu\mu$ mass fit is:

$$
\begin{aligned}
M_Z &= 91101 \pm 48_{\rm stat} \pm 28_{\rm tracker} \pm 8_{\rm fitter} \text{ MeV} \\
&= 91101 \pm 56 \text{ MeV} \qquad (14)
\end{aligned}
$$

The result is lower than the world-average Z mass at the 1.5σ level.

5.6 COT Momentum Resolution

The tracking resolution is tuned using the width of the Z mass peak. The resolution is parameterized in the simulation by the hit resolution σ_h. We vary this parameter so that the χ^2 of the Z mass distribution is minimized, and let the χ^2 increase by 1 to obtain the error on σ_h. We obtain

$$\sigma_h = (200 \pm 15)\mu m \tag{15}$$

6 Online and Production Calibration for Central Electrons

Online, individual PMT gains and an overall scale factor are applied in reconstructing energy which is used at all levels of triggering. Initial values for CEM PMT gains were set using source calibration. An early sample of data was used to check the Z mass at the level of 0.2% and since then time dependence, taken for convenience as run number dependence, has been monitored using the 8 GeV electron trigger sample. We attempted to keep the overall scale within a range of 3% by revising the online scale factor when needed. The windowed (0.8 to 1.25) E/P distribution for 8 GeV electron triggers as reconstructed online is shown in Fig. 41.

The a piecewise continuous run number dependence was used in production to reduce the time dependence. The windowed E/P for 8 GeV triggers with E + P > 22 is plotted in Fig. 42 with the production correction. Note that due to the windowing, deviations tend to be reduced by about a third; corrections are iterated. The run ranges that were used to generate individual tower gains are marked. Statistical accuracy for tower gains, other than the outermost η rings, is less than $\pm 0.3\%$. The spread in the initail set of production tower gains was $\pm 5\%$ and revised pmt gains were downloaded at the detector; since then the tower gain spread has gradually diffused back up to about $\pm 02.5\%$.

The 8 GeV sample is dominated by fakes and windowed E/P is thus appropriate as a fuction of η as well as ϕ. Windowed E/P for electron W candidates within the 8 GeV trigger sample (E_T and MET > 22GeV) is plotted versus shower max z coordinate in Fig. 43. Note that for real electrons, a roughly parabolic increase with z is expected as controlled in detail by the material inside the COT. Detailed tuning remains to be done. Tower 0 gain trends high due to fakes having more leakage.

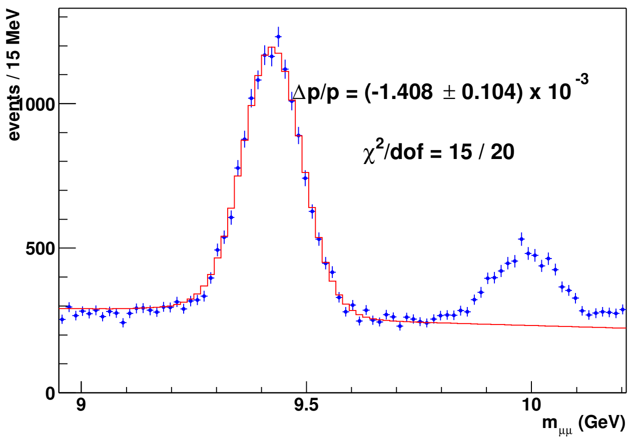

Figure 38: The invariant mass distribution with the best fit simulated template and the extracted momentum scale using non beam constraint quantities.

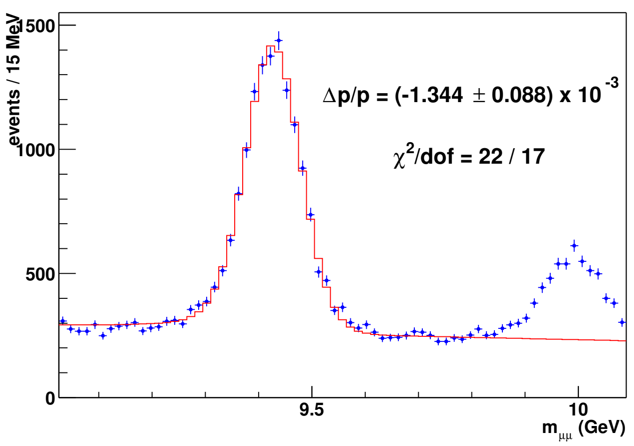

Figure 39: The invariant mass distribution with the best fit simulated template and the extracted momentum scale using beam constraint quantities.

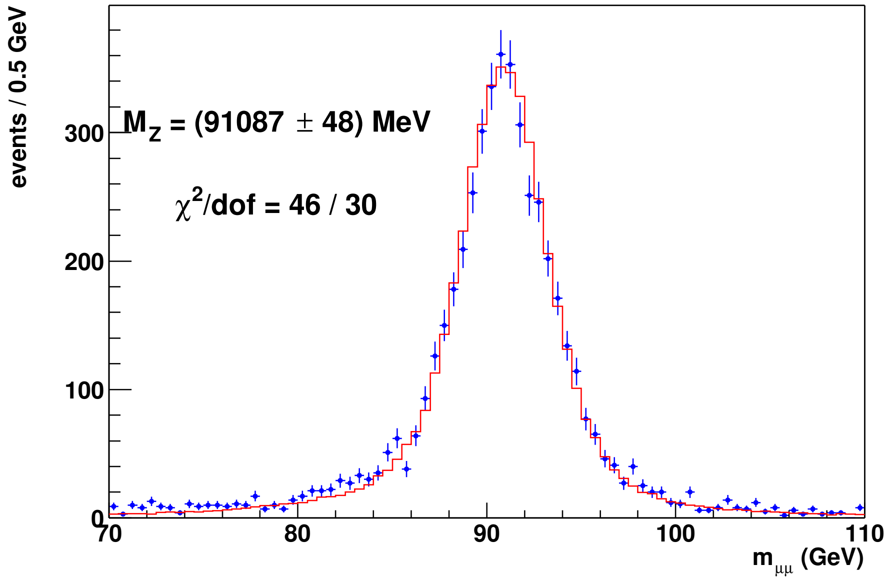

Figure 40: The fitted $Z \to \mu\mu$ mass using the COT momentum scale derived from the $J/\psi \to \mu\mu$ measurement.

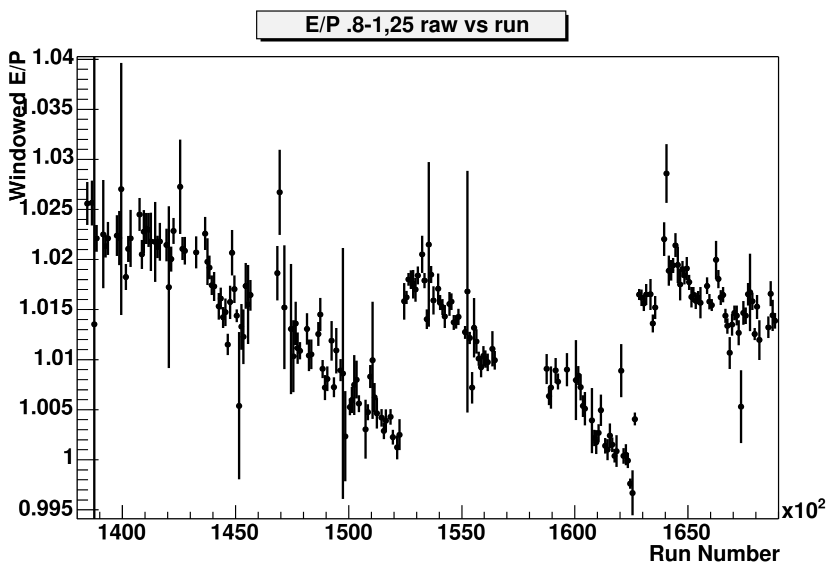

Figure 41: Windowed E/P (0.8-1.25) versus run number for 8 GeV electrons with $E+P > 22$. Online scale was revised upward by 3% twice.

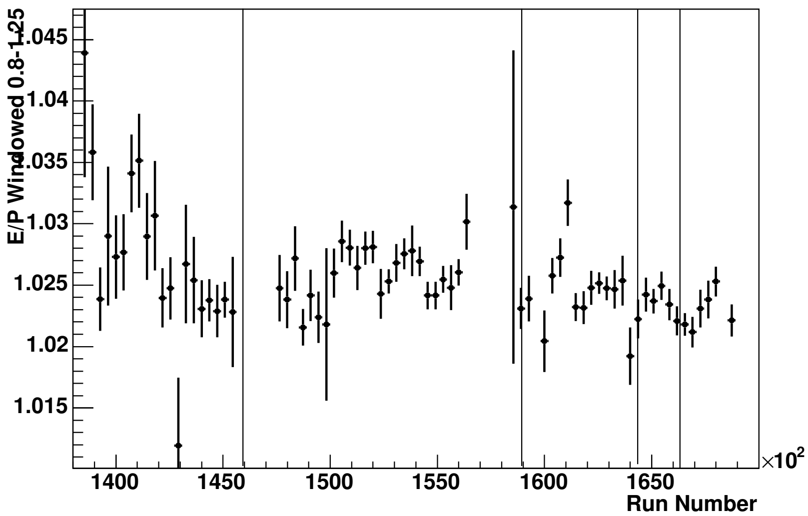

Figure 42: Windowed E/P (0.8-1.25) versus run number for 8 GeV electrons with $E+P > 22$ with offline run dependence correction applied. Vertical line denote run ranges used to determine tower gains.

6.1 Electromagnetic Calorimeter Scale and Resolution

We set the electromagnetic calorimeter energy scale using the peak of the E/p distribution from $W \to e\nu$ events. The track momentum has the momentum scale correction applied, as derived from the $J/\psi \to \mu\mu$ data. We perform a maximum likelihood fit for the energy scale factor S_E, with the results shown in Fig. 44. The data have been corrected by scaling the cluster energy by the factor 1.003. The energy is measured using the two-tower cluster algorithm in the data. In the simulation, the two-tower algorithm is used to coalesce radiated photons. Two-tower underlying event energy is also added to the simulated cluster energy.

The uncertainty on the energy scale S_E receives contributions from the uncertainty in the amount of passive material (Sec. 5.1), and the uncertainty in the track momentum scale (Eqn. 13). Thus we obtain

$$\begin{aligned} S_E &= 1.00007 \pm 0.00032_{\rm stat} \pm 0.00068_{X_0} \pm 0.00031_{\rm tracker} \\ &= 1.00007 \pm 0.00081 \end{aligned} \tag{16}$$

The electromagnetic calorimeter resolution is tuned by minimizing the χ^2 near the peak region. The resolution is parameterized as

$$\sigma_E/E = 13.5\%/\sqrt{E_T} \oplus \kappa \tag{17}$$

where κ is the tuned constant term in the resolution. From the width of the E/p peak we measure $\kappa = (1.2 \pm 0.05)\%$.

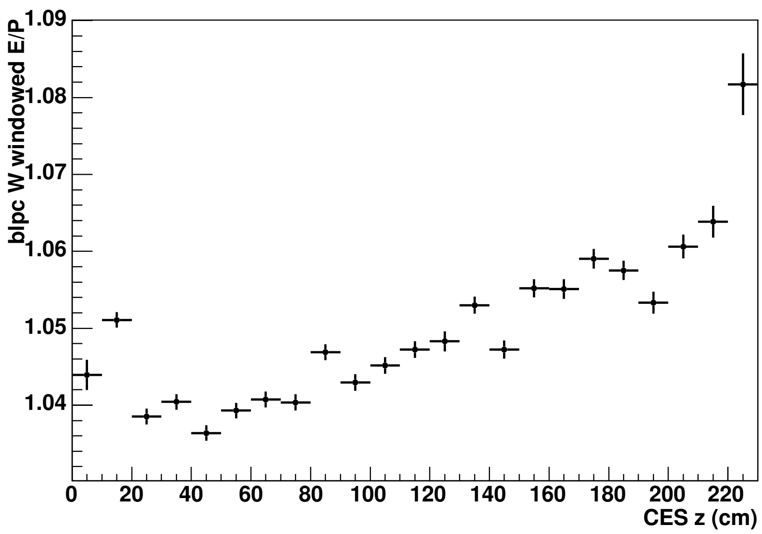

Figure 43: Windowed E/P (0.8-1.25) shower max z coordinate for 8 GeV electrons with $E + P > 22$.

The $Z \to ee$ lineshape prefers $\kappa = (1.3 \pm 0.1)\%$. We use the result from the $Z \to ee$ fit, since it is statistically consistent with the calorimeter resolution measured from the E/p peak fit: therefore $\kappa = (1.3 \pm 0.1)\%$. The advantage of this choice is that the calorimeter resolution used for the W fits is independent of tracking momentum resolution. The $Z \to ee$ mass fit is shown in Fig. 46.

The calorimeter energy non-linearity is studied by performing template fits to the E/p distribution in bins of E_T. As usual, the templates are also generated in each E_T bin separately, to take other E_T-dependent effects such as resolution into account. The fitted energy scale S_E is plotted vs E_T and a small positive slope is observed for a linear fit, showing that the calorimeter energy response increases slightly with energy. We parameterize the linear increase of S_E as follows:

$$\delta S_E = \xi(E_T - 36) \text{ GeV} \tag{18}$$

We choose the offset to be 36 GeV, which is $< E_T >$ for the W sample, so that the inclusive energy scale is not sensitive to ξ. We fit S_E as a function of E_T with the functional form

$$S_E = 1.00007 + \xi(E_T - 36) \text{ GeV} \tag{19}$$

where the constant 1.00007 is the energy scale from the fit to the inclusive E/p distribution.

To suppress the effect of E_T-dependent QCD background contamination, the binned S_E fit is performed with a tighter W sample: we raise the E_T and $\not\!\!E_T$ cuts to 30 GeV, and lower the u_T to 10 GeV, which lowers the QCD background contamination below 0.5%. We do not include any QCD background component in the binned S_E fits, but we estimate the systematic uncertainty due to it by assuming that all the remaining background is in the first two E_T bins. We measure the effect of this assumption on the fitted S_E in the first two bins, and propagate it to the change in the slope ξ. We find the systematic uncertainty on ξ due to QCD background by this procedure to be 2×10^{-5}/GeV, which as we show below is negligible compared to the statistical uncertainty.

Since the W sample does not have good statistics beyond E_T of 45 GeV, we augment the data by performing the same binned S_E fit with the Z sample as well. Both electrons in the Z event are used. This populates the region of $45 < E_T < 50$ GeV more reliably than the W sample, where background contamination in the tail of the E_T distribution could be a concern.

We find that $\xi = 34 \times 10^{-5}$/GeV describes both the W and Z data. We correct the data for this non-linearity, and find a one-one correspondence between the observed slope of S_E vs E_T and the non-linearity parameter. Figures 47 and 48 show the binned S_E results from the W and Z samples respectively, after the non-linearity correction is applied. The residual slopes are consistent with zero and with each other within statistical errors. We average the residual slopes to obtain $(0.6 \pm 8.1) \times 10^{-5}$/GeV, giving the result

$$\xi = 0.00034 \pm 0.00008_{\rm stat} \tag{20}$$

The results mentioned earlier in this section already have this non-linearity correction applied. The uncertainty in the W (Z) mass due to the uncertainty in ξ is 25 (55) MeV/c^2.

The difference of the measured $Z \to ee$ mass from the PDG value is

$$\begin{aligned} \Delta M_Z &= -144 \pm 64_{\rm stat} \pm 81_{S_E} \pm 55_\xi \text{ MeV} \\ &= -144 \pm 119 \text{ MeV} \end{aligned} \tag{21}$$

which is 1.2σ below the PDG value.

When we combine these same uncertainties and apply them to the W boson mass fits we find a

$$\Delta m_W = \pm 81_{S_E} \pm 25_\xi = 85 \text{ MeV} \tag{22}$$

due to systematics on energy scale and non-linearity. This is reported as the systematic in section 9.

7 Hadronic Recoil Tuning

We use $Z \to \mu\mu$ events to tune the recoil response and resolution parameters. We project the p_T-balance onto the η and ξ axes, and compare the distributions with the simulation. The hadronic scale parameters a, b, c are tuned using the mean value of the p_T-balance in the η direction, as a function of $p_T(\mu\mu)$. We obtain the values $a = 0.55, b = 1.4, c = 3.0$. The comparison is shown in Fig. 49.

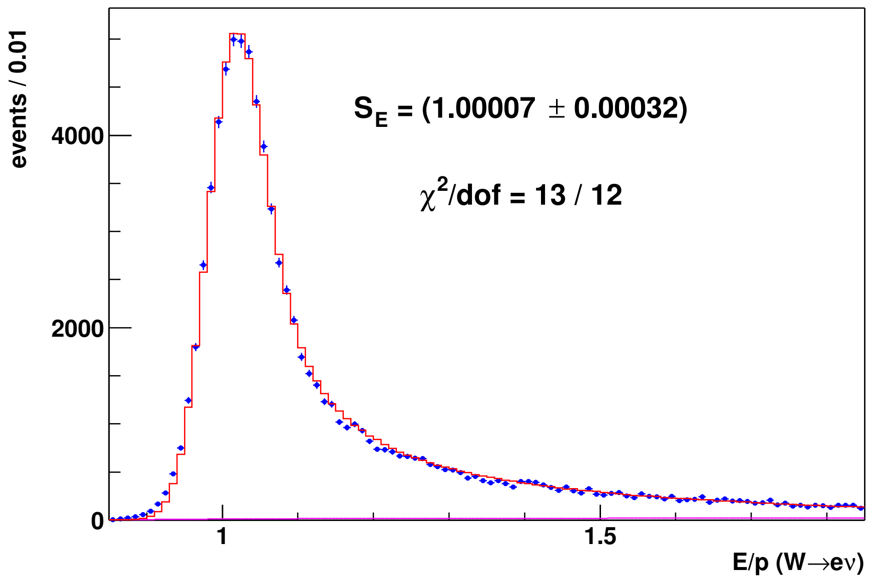

Figure 44: The maximum likelihood fit to the E/p peak from $W \to e\nu$ data. The QCD background distribution is included in the simulation templates. The data are already corrected with the energy scale factor of 1.003.

To derive the uncertainty on the hadronic response parameterization, we scale the response function R by $1 \pm \delta R$, in order to change the χ^2 in Fig. 49 by unity. We obtain

$$\delta R = 0.013 \tag{23}$$

We measure the resolution parameters by comparing the r.m.s. of the p_T-balance in the η direction, as a function of $p_T(\mu\mu)$ (see Fig. 50). The parameter s_{had} is sensitive to the slope of the plot, and we measure

$$s_{\text{had}} = 0.7 \pm 0.1 \text{ GeV}^{\frac{1}{2}} \tag{24}$$

The intercept of the plot determines the parameter α_{MB}. We tune the parameter N_Z as a means of tuning α_{MB} for $Z \to \mu\mu$ events. We measure

$$N_Z = 1.07 \pm 0.05_{\text{stat}} \tag{25}$$

Figures 51-52 show the $p_T(\mu\mu)$ and recoil distributions.

We use this model to compare the recoil quantities in W data to the simulation. We find that the resolution tuned with the Z events does not fully describe the recoil distributions of the W events. We increase the parameter N_W to the value

$$N_W = 1.2 \tag{26}$$

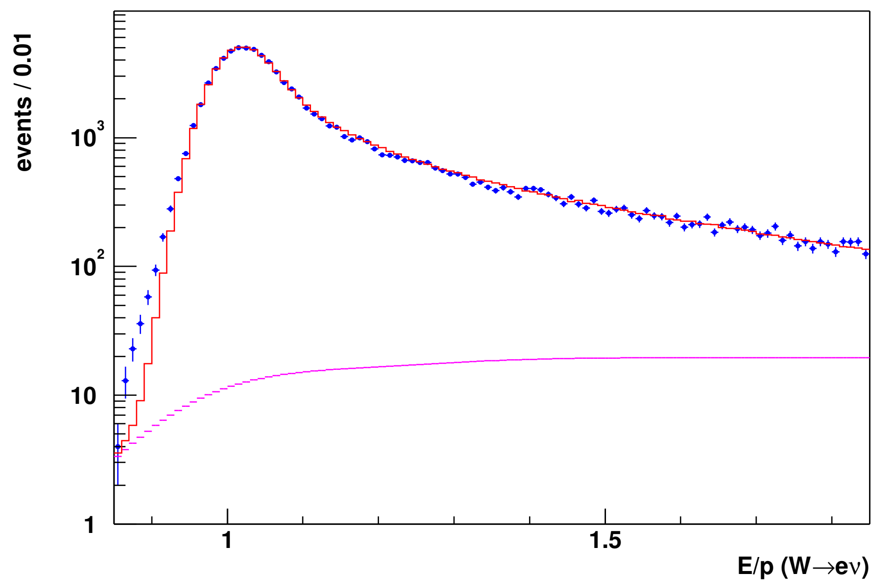

Figure 45: The maximum likelihood fit to the E/p peak from $W \to e\nu$ data. The QCD background distribution is included in the simulation templates. The data are already corrected with the energy scale factor of 1.003.

to be able to describe the W data. Figures 53-54 show the distributions of the two projections of the u_T. Figures 55-56 show the u_T and $\phi_u - \phi_l$ distributions.

We check the simulation of the recoil response and resolution using $Z \to ee$ (Figs. 57-60) and $W \to e\nu$ (Figs. 61-64) events. The distributions are in good agreement.

The difference in recoil resolution between W and Z events is likely due to the inefficiency of the lepton selection. If the inefficiency is sensitive to the hadronic activity in the event, the selection of two leptons in Z boson events is likely to suppress hadronic activity in Z events more than in W events. Figure 65 shows the comparison of the ΣE_T distributions of our W and Z events. A difference in mean ΣE_T, and a larger difference in recoil resolution between W and Z events, are observed if tighter lepton selection is applied, such as axial=4/stereo=3 COT SL cuts. For the latter cuts, we have ($< \Sigma E_T(W) >= 54.79 \pm 0.13$ GeV) and ($< \Sigma E_T(Z) >= 53.12 \pm 0.45$ GeV). The ΣE_T in W and Z events is suppressed by the tighter tracking cuts.

To summarize, we compute the systematic uncertainty on the recoil model scale we vary δR in equation 23 by 1σ and find that this alters the fit mass by 20 MeV/c^2 for the transverse mass and neutrino p_T fits and by only 5 MeV/c^2 for the charged lepton p_T fits.

For the recoil model scale we consider two effects. We vary s_{had} by the uncertainty shown in equation 24 and find this results in a 20 MeV/c^2 uncertainty on the transverse mass fits, 10 MeV/c^2 on the charged lepton p_T fits and 30 MeV/c^2 on the neutrino p_T fits. To this we add the effect of difference between the apparent activity underlying Z and W events. We

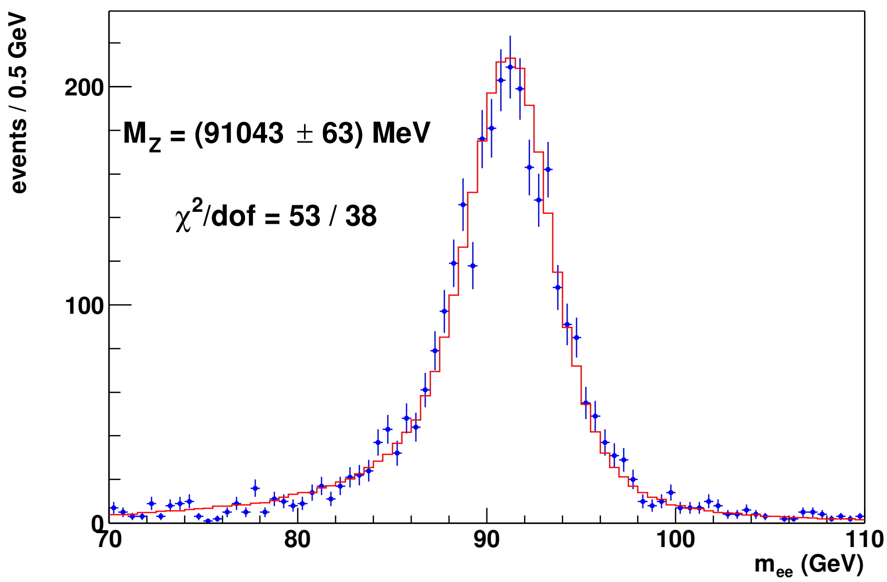

Figure 46: The maximum likelihood fit to the $Z \to ee$ mass peak, with the fitted mass value. The data are already corrected with the energy scale factor of 1.003.

see $N_Z = 1.07 \pm 0.05$. We use $N_W = 1.20$ (with a negligible statistical uncertainty). As one can see from figures 63 and 55 even this does not fully describe the low u_T region. We find that inflating N_W to 1.32 actually does describe these plots well. Thus, for the preliminary result, we take $N_W = 1.20 \pm 0.13$ which allows us to cover matching both the Z and W u_T distributions in the range of our systematic uncertainties. This results in 37 MeV/c^2 uncertainties on the transverse mass fits, 13 MeV/c^2 uncertainties on the charged lepton p_T fits and 65 MeV/c^2 uncertainties on the neutrino p_T fits. We combine these two effects the summaries of systematics in section 9 on the line labeled "Recoil Resolution" and quote 42, 16 and 72 MeV/c^2 for the m_T, p_T and $\not\!\!E_T$ fits, respectively.

In order to check that the uncertainties due to energy scale and resolution may be treated independently and added in quadrature, we investigate the sensitivity of the fitted W mass to correlated fluctuations of the recoil scale and resolution parameters. We fluctuate the response function R and the resolution parameter N_W simultaneously by $(\pm 2\sigma, \pm 2\sigma)$ in the simulation, use the resulting templates to fit the data, and take the differences of the fitted W masses along the two "diagonals". We divide these differences by $4\sqrt{2}$ to obtain the W mass variations along the correlated (anti-correlated) directions, and obtain 11 MeV (28 MeV), 4 MeV (3 MeV), and 44 MeV (38 MeV) for the m_T, $p_T(l)$ and $\not\!\!E_T$ fits respectively. Combining them in quadrature gives 30 MeV, 5 MeV and 58 MeV for the m_T, $p_T(l)$ and $\not\!\!E_T$ fits respectively. Since these variations do not show evidence of a large sensitivity to correlated recoil scale and resolution parameter fluctuations, we continue to treat recoil scale and resolution uncertainties as being independent.

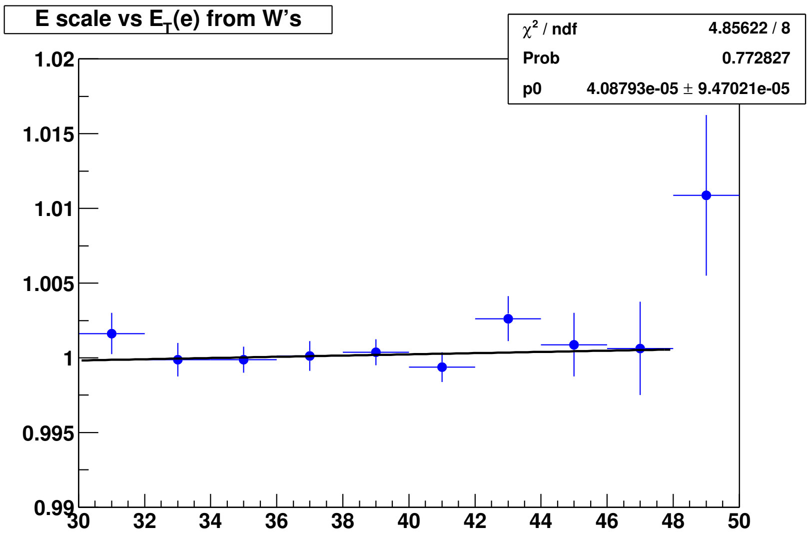

Figure 47: The fitted energy scale S_E, obtained from the E/p distribution in bins of E_T for the W sample. The line is the best fit for the non-linearity parameter ξ, after the non-linearity correction is applied to the data.

8 Background

Backgrounds passing the event selection cuts have a very different transverse mass, transverse momentum and transverse missing energy distributions in comparison to the W signal. In order not to bias the mass fits to these distributions, the backgrounds have to be included in the simulated templates used to extract the mass. The background to the W$\rightarrow \mu\nu$ and W$\rightarrow e\nu$ samples come from hadronic jet production, decays in flight, Z production, W's decaying in the tau channel and cosmic rays.

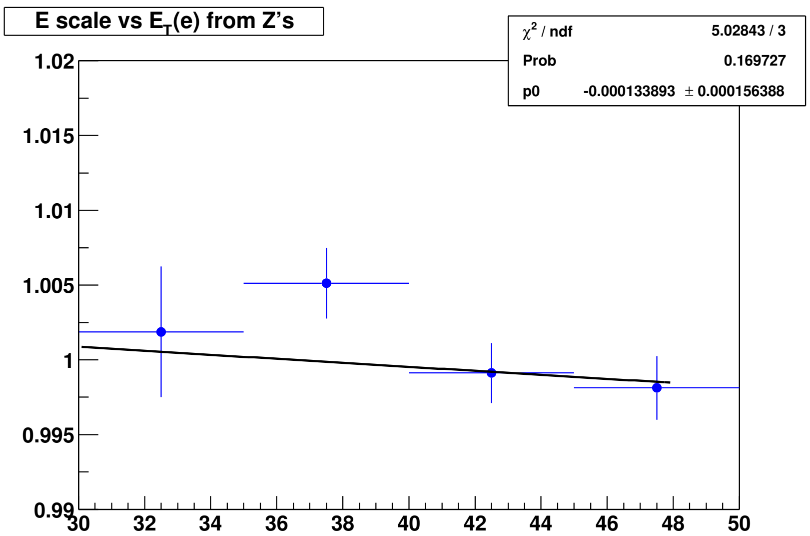

Figure 48: The fitted energy scale S_E, obtained from the E/p distribution in bins of E_T for the Z sample. The line is the best fit for the non-linearity parameter ξ, after the non-linearity correction is applied to the data.

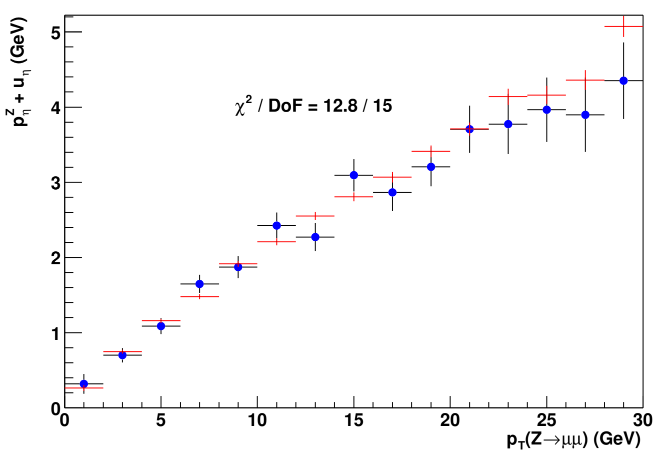

Figure 49: The mean value of p_T-balance in $Z \to \mu\mu$ events.

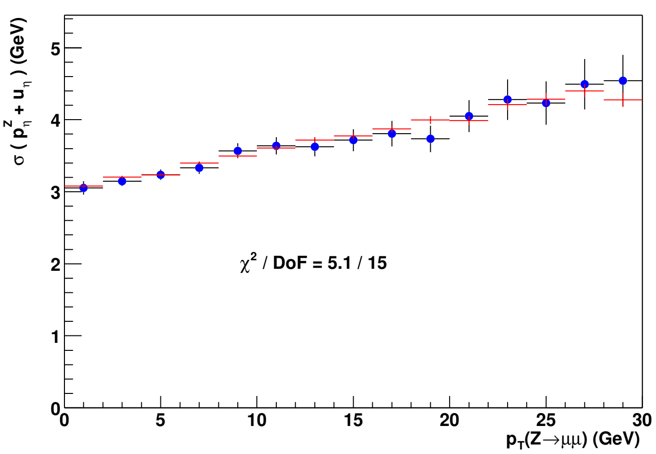

Figure 50: The r.m.s. of p_T-balance in $Z \to \mu\mu$ events.

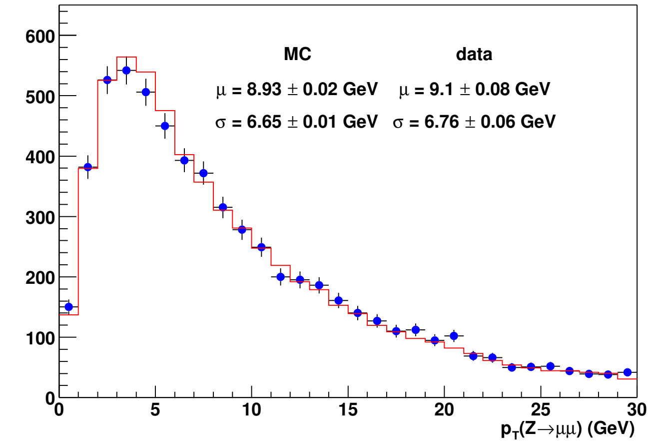

Figure 51: The distribution of $p_T(\mu\mu)$ in $Z \to \mu\mu$ events.

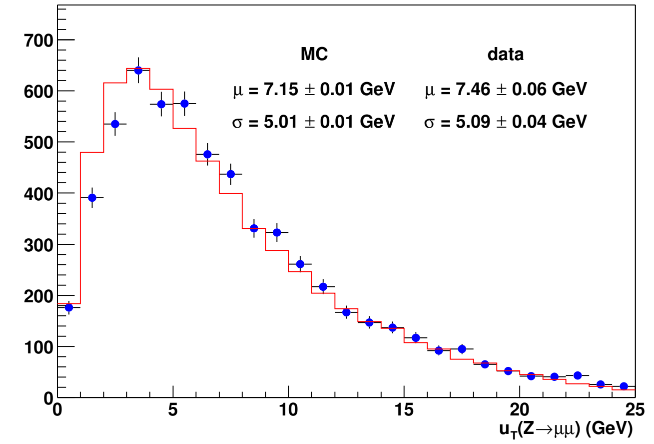

Figure 52: The distribution u_T in $Z \to \mu\mu$ events.

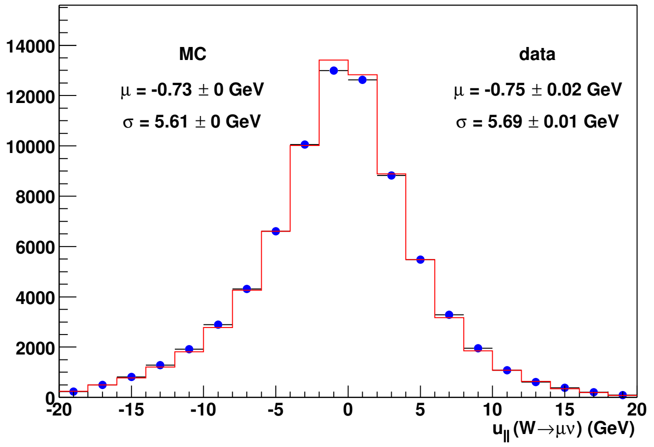

Figure 53: The distribution of $u_{||}$ in $W \to \mu\nu$ events. Background contribution is included in the simulated distribution.

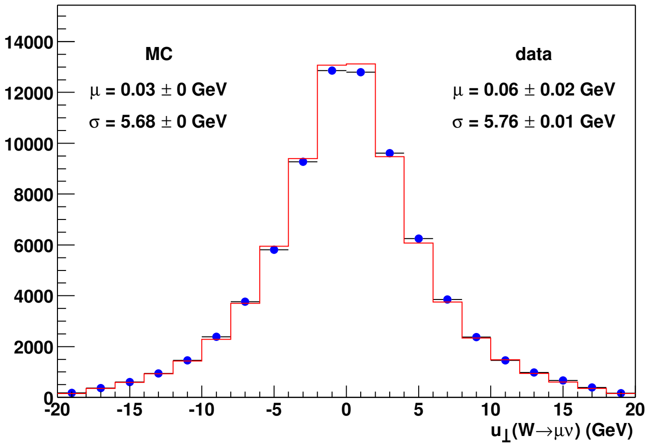

Figure 54: The distribution u_{perp} in $W \to \mu\nu$ events. Background contribution is included in the simulated distribution.

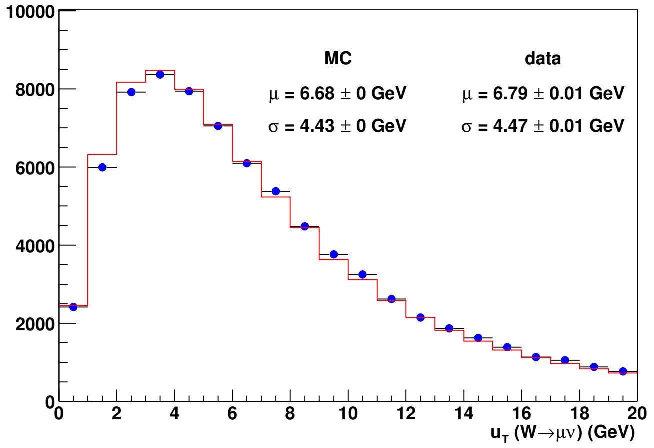

Figure 55: The distribution of u_T in $W \to \mu\nu$ events. Background contribution is included in the simulated distribution.

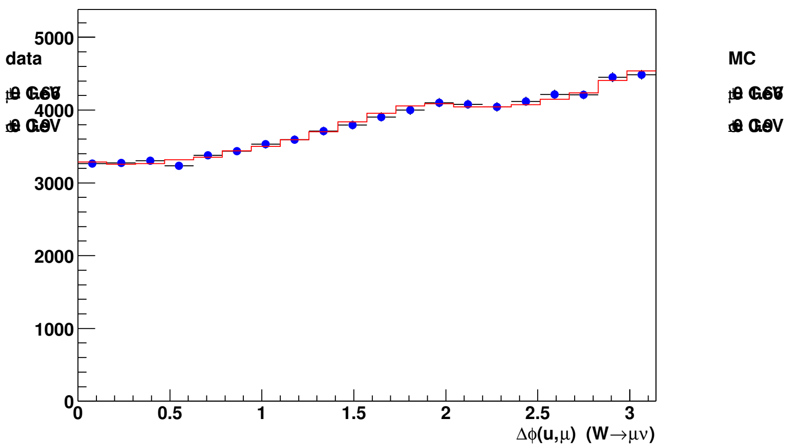

Figure 56: The distribution $\Delta\phi$ in $W \to \mu\nu$ events.

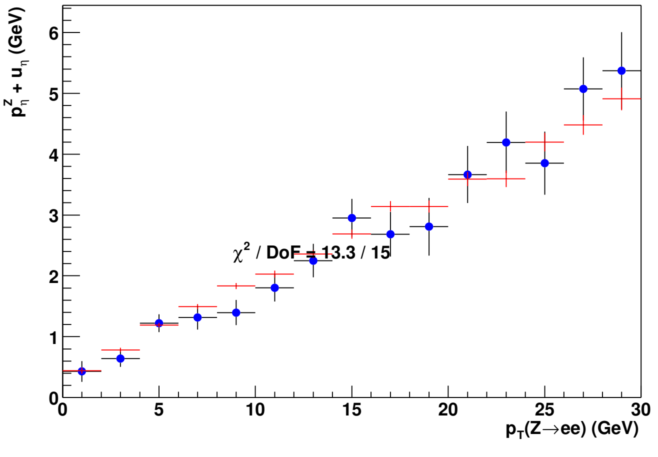

Figure 57: The mean value of p_T-balance in $Z \to ee$ events.

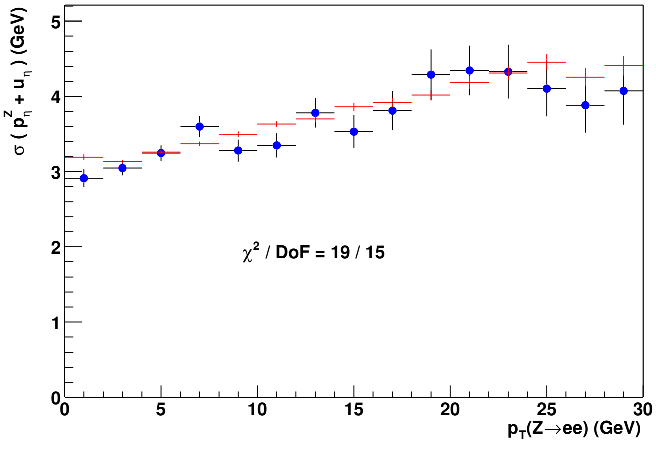

Figure 58: The r.m.s. of p_T-balance in $Z \to ee$ events.

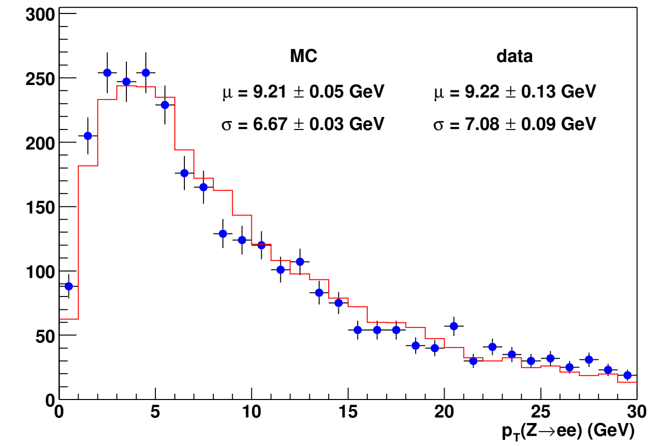

Figure 59: The distribution of $p_T(ee)$ in $Z \to ee$ events.

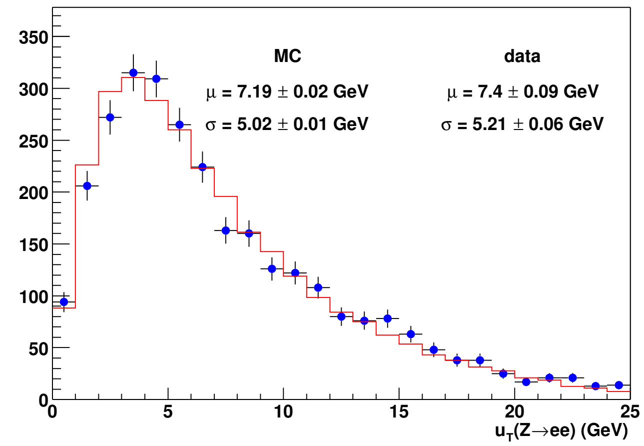

Figure 60: The distribution u_T in $Z \to ee$ events.

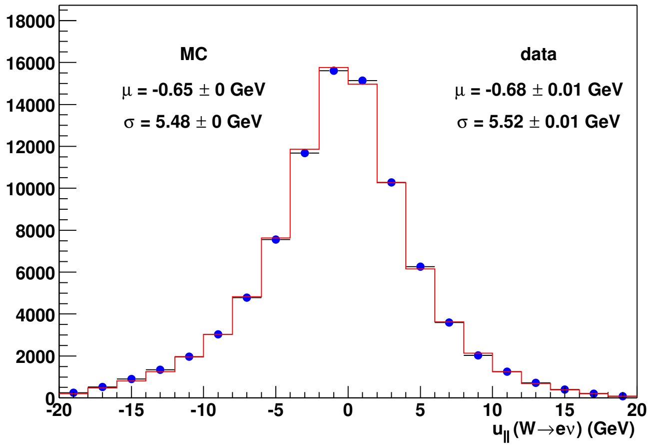

Figure 61: The distribution of $u_{||}$ in $W \to e\nu$ events.

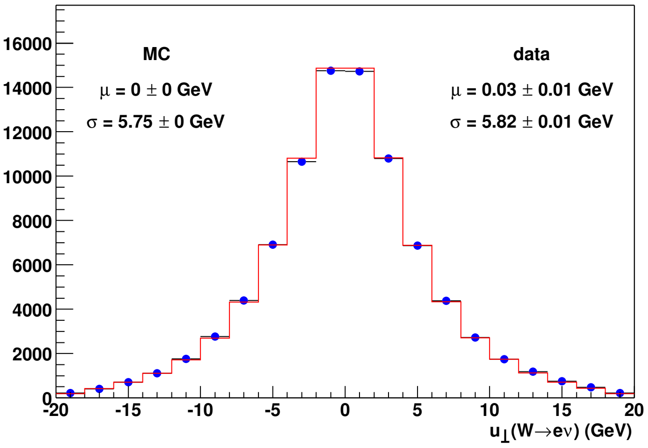

Figure 62: The distribution u_{perp} in $W \to e\nu$ events.

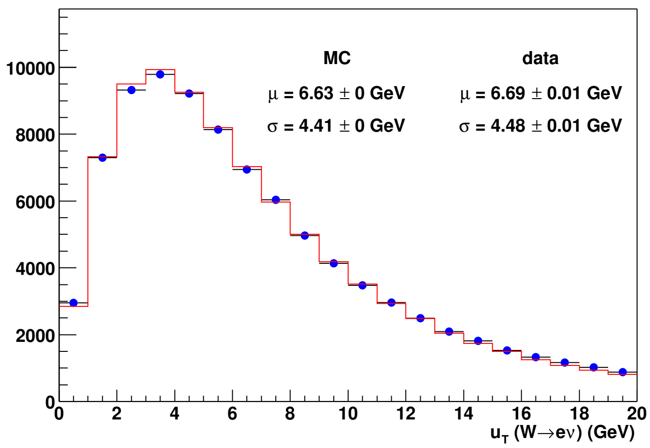

Figure 63: The distribution of u_T in $W \to e\nu$ events.

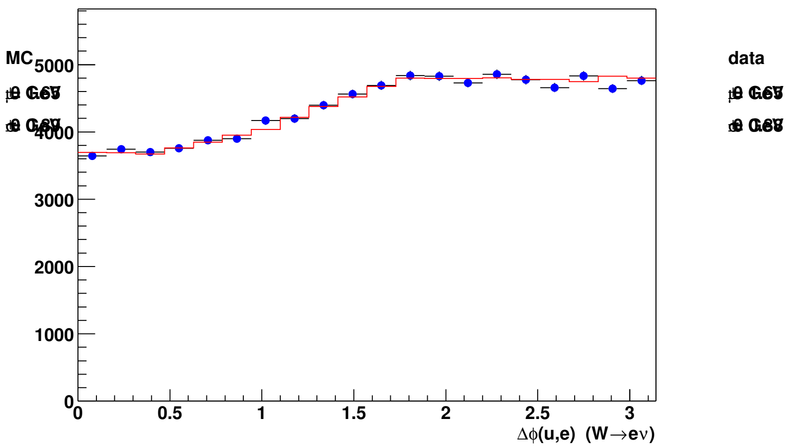

Figure 64: The distribution $\Delta\phi$ in $W \to e\nu$ events.

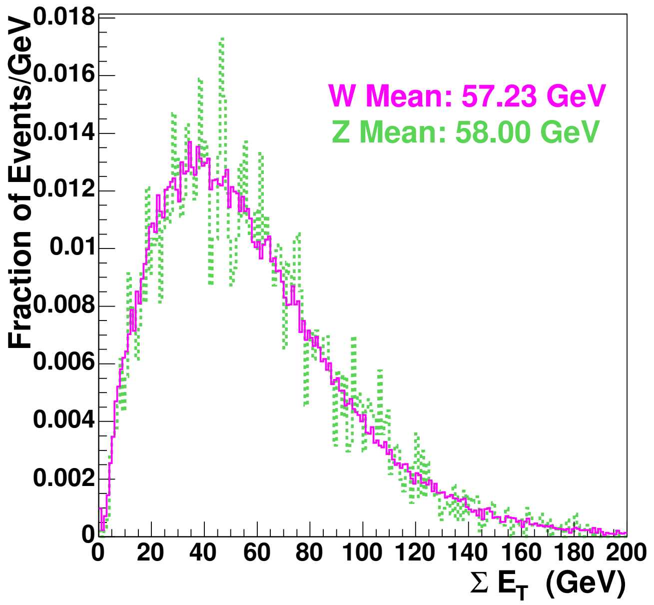

Figure 65: The comparison of ΣE_T distributions in W and Z events.

8.1 Electron Channel

The background contributions to the W data set affect the measured W mass by altering the shapes of the fit distributions. We measure the shapes and the normalizations of the backgrounds and incorporate them into the W data set simulation. The uncertainties of the shapes and normalizations translate directly into a systematic uncertainty on the measured W mass.

The background to the $W \to e\nu$ data set consists of events containing hadronic jets, $Z \to ee$, and $W \to \tau_e \nu$. Reference [18] decscribes he procedure for measuring each background's normalization and shape, and its corresponding uncertainties.

The $Z \to ee$ and $W \to \tau_e \nu$ backgrounds are obtained from Monte Carlo and normalized using the ratio of acceptances to $W \to e\nu$ Monte Carlo events. The shapes and normalizations are well understood.

The QCD background is obtained from a fit to the $\not\!\!E_T$ distribution in the W data sample, using a neural network identification variable to select the hadronic-jet $\not\!\!E_T$ distribution. The result is shown in Fig. 66.

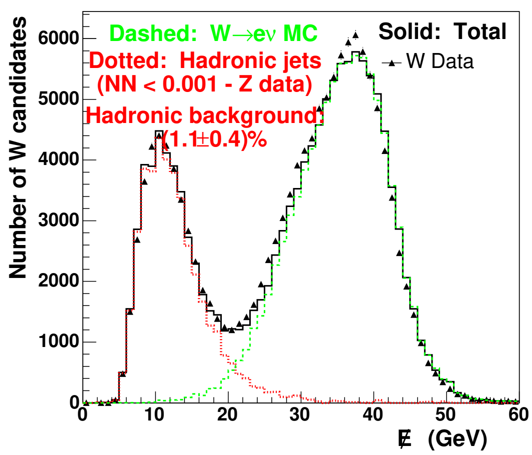

Figure 66: The fit of the $\not\!\!E_T$ distributions of $W \to e\nu$ Monte Carlo and hadronic jets to the W candidates. The hadronic-jet $\not\!\!E_T$ distribution is obtained using the low-neural-network-output (NN <0.001) region and corrected for electron contamination using the Z NN distribution.

Table 9 shows the fraction of each type of background in the $W \to e\nu$ data set. The uncertainties on the normalization result in systematic uncertainties on the W mass measurement of 16 MeV, 6 MeV, and 8 MeV for the M_T, p_T and $\not\!\!E_T$ fits, respectively (Table 10).

Background	% of $W \to e\nu$ data sample
Hadronic jets	1.1 ± 0.4
$W \to \tau\nu$	1.9 ± 0.1
$Z \to ee$	0.26 ± 0.03

Table 9: The percentages of the various backgrounds to the $W \to e\nu$ data set.

Background	M_T fit	p_T fit	$\not\!\!E_T$ fit
Hadronic jets	15 MeV	5 MeV	5 MeV
$W \to \tau\nu$	3 MeV	3 MeV	5 MeV
$Z \to ee$	3 MeV	0 MeV	3 MeV

Table 10: The systematic uncertainties of the various W mass fits due to the uncertainty on the normalization of the $W \to e\nu$ backgrounds.

8.2 Muon Channel

The largest backgrounds in the W$\to \mu\nu$ sample comes from Z$\to \mu\mu$ where one of the muon tracks is lost. In size, this is followed by $W \to \tau\nu$ events, where the τ decays into $\mu\nu$. Other backgrounds come from decays in flight (kaons), from QCD jet events, where one jet contains a non-isolated muon and from cosmic rays, entering the CDF detector.

8.2.1 Cosmic Background

High energetic muons originating from cosmic rays can fake a W decay. Most of these events are removed by a specially designed cosmic tagger. The cosmic tagger utilizes the fact that the track originating from a cosmic ray does not coincide with the bunch crossing time. It employs a multi-parameter fit to the found hits in the COT tracking chamber including the track production time t_0 as a free parameter.

We estimate the remaining cosmic background by examining the production time distribution of the refitted tracks for all signal candidates with the hypothesis that they originated from the center of the detector. We compare this distribution with events which were identified as cosmic rays and with Z$\to \mu\mu$ events. These distributions are shown in Figure 67 for the W signal region and in Figure 68. for the d_0 sideband region.

For the identified cosmic rays, one would expect a flat t0 distribution. Biases from the pattern recognition of the tracking algorithms, which favour tracks with small t0, result in a plateau for smaller t0 values. We estimate the size of the cosmic background in the W candidate sample by normalizing the sideband regions of the t0 distribution for the identified cosmic sample to the W candidate sample. Table 11 shows the estimates applying different normalization regions for the W signal region and for the d_0 sidebands of the signal region. The d_0 sideband events are selected between $|0.2|$-$|0.6|$ cm. It also shows the same

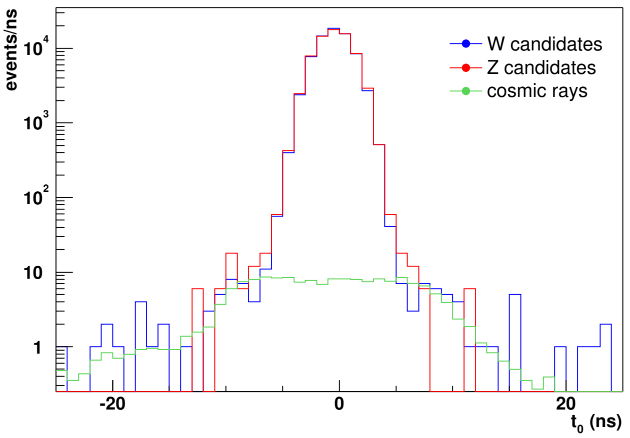

Figure 67: t0 distribution for the outgoing track for all signal events.

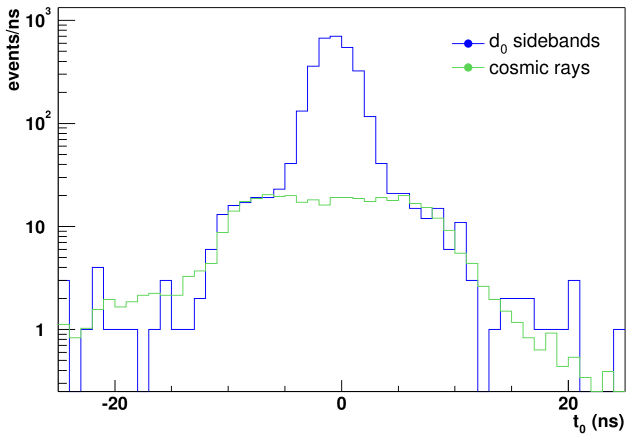

Figure 68: t0 distribution for the outgoing track for d_0 sideband events.

Normalization Region	Estimate in Signal Region	Estimate in d_0 Sidebands
7-15 ns	0.24±0.03	0.28±0.03
7-10 ns	0.24±0.04	0.28±0.03
7-25 ns	0.29±0.03	0.29±0.03
10-25 ns	0.35±0.05	0.30±0.03

Table 11: Background estimates for different normalization regions.

plateau characteristic for the cosmic events as in the W signal region. From the spread of the background size estimates in the two regions we obtain a cosmic background size of 0.3±0.1%.
We obtain the kinematic background shapes from identified cosmic rays found in the used inclusive muon sample. All W selection cuts are applied, with exception to the cosmic tag, which is inverted.

8.2.2 Decays in Flight (Kaon) Background

The t0 distribution of d_0 sideband events in Figure 68 shows a large signal on top of the flat plateau originating from cosmic rays. This signal is thought to come from decays in flight, such as kaons decaying into muons. We estimate the contamination of this background in our signal region by evaluating the $\delta\phi(l,u)$ distribution, shown in Figure 56. An excess in the data can be observed at pi originating from decays in flight. Adding the $\delta\phi(l,u)$ distribution from decays in flight sideband events to the simulation to match the data, we estimate this background to be $1.0 \pm 1.0\%$.

8.2.3 QCD Background

The QCD dijet background is estimated utilizing the fact, that QCD jet events tend to be non isolated and have low missing transverse energy in the event. The first distribution we examine is the $\not\!\!E_T$ spectrum of the W candidates with the $\not\!\!E_T$ cut removed. A local maxima at low $\not\!\!E_T$ can be observed arising from QCD events. We model the observed data distribution with W MC events with the fractional amounts of Z$\rightarrow \mu\mu$ and W$\rightarrow \tau\nu$ backgrounds added. Various amounts of QCD shape is then added to the MC and the χ^2 computed. Figure 69 shows the $\not\!\!E_T$ distribution for the case of 1.7% QCD shape added, which was obtained from a χ^2 minimization. The W candidates are drawn in blue, the W MC events with backgrounds added are drawn in red. Since the QCD shape is obtained from the iso>0.3 region, we expect

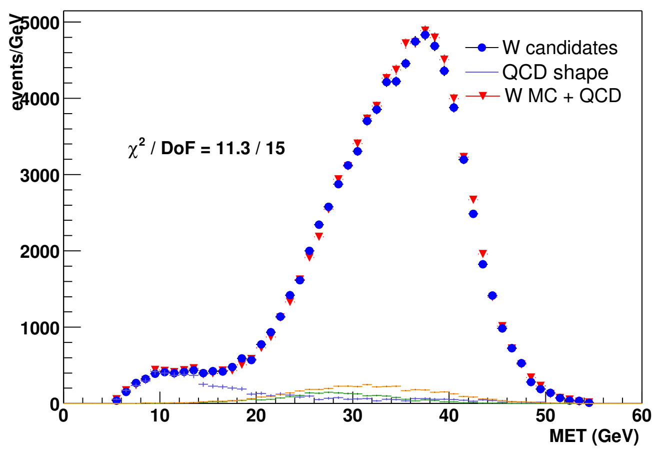

Figure 69: χ^2 fit for 1.7% QCD shape added in the $\not\!\!E_T$ distribution.

some signal contamination in this distribution. Estimating this contamination using signal MC samples, we find a 0.3% contamination, effectively reducing the QCD di-jet background estimate to 1.4%.

We further examine two other distributions where we expect a significant difference in shape for QCD and W candidate events, namely the track isolation and calorimeter isolation ratio distribution. This time the order is reversed and the QCD shape obtained from the low MET of the W candidates. Different amounts of QCD shape is added to a tight Z sample to match the distributions for the W signal. The χ^2 is computed between the combined tight Z events with QCD distribution added and the distribution from the W signal. The distribution for the QCD shape is drawn in green, the combined shape from the tight Z sample and QCD shape is drawn in red and the W candidates are represented by the blue points. Figure 70 shows the calorimeter isolation ratio where 0.9% QCD shape is added (obtained from the χ^2 minimization). Applying the same technique using the track isolation ratio an estimate of

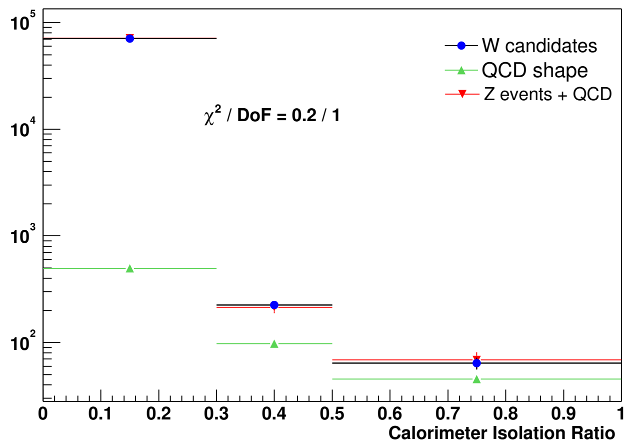

Figure 70: χ^2 fit for 0.9% QCD shape added in the calorimeter isolation ratio distribution.

0.5±0.2% is obtained. We estimate a total QCD background of 0.9±0.5%, using the value obtained from the fit to the calorimeter isolation ratio as the central value and the spread of the two other estimates as a systematic uncertainty. The kinematic QCD distributions from dijet events are obtained by inverting the E$_{em}$, E$_{had}$, Δx stub matching and requiring the isolation fraction to be greater than 0.25. If three out of four of these conditions on top of the other W selection cuts are met the event is included in the QCD shapes.

8.2.4 Backgrounds from Z$\rightarrow \mu\mu$ and $W \rightarrow \tau\nu$

Events which have two isolated, minimum ionizing high p_T tracks with opposite charge are rejected according to the Z rejection defined in the event selection. Figure 71 shows the rejected events with Z$\rightarrow \mu\mu$ MC overlaid. The two distributions show reasonable agreement. To evaluate how many W events get rejected we apply $W \rightarrow \mu\nu$ MC events to the Z rejection. Only 3 events are found. To estimate the Z$\rightarrow \mu\mu$ and $W \rightarrow \tau\nu$ backgrounds we use MC samples generated with Pythia and the CDF detector simulation applied. We apply our $W \rightarrow \mu\nu$ event selection on both samples as well as on $W \rightarrow \mu\nu$ signal MC sample and compute the individual acceptances for each process. Then using Standard Model values for the relative production rates of the three processes and utilizing these acceptance values one can calculate the relative contribution from each process. The production cross section for $W \rightarrow \mu\nu$ and

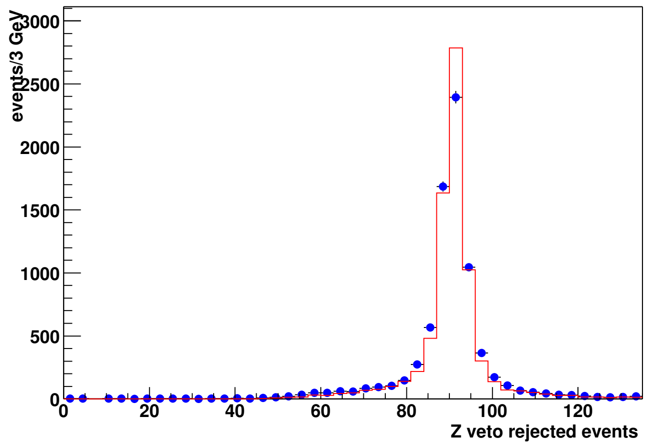

Figure 71: Events rejected by Z veto with Z$\rightarrow \mu\mu$ MC overlaid.

$W \rightarrow \tau\nu$ are equal whereas the $W \rightarrow \mu\nu$ and Z$\rightarrow \mu\mu$ production cross section are related by a factor R. NNLO calculation finds R=10.67±0.15 at $\sqrt{s}$ = 1.96 TeV. We combine the

	W$\rightarrow \mu\nu$ MC	Z$\rightarrow \mu\mu$ MC	$W \rightarrow \tau\nu$ MC
Number of MC events	474450	93681	466453
Passing all cuts	72489	7303	1448
Acceptance	15.28±0.06	7.80±0.09	0.31±0.01
Correction for R		0.73±0.02	
Acceptance Fraction	93.62±0.52	4.48±0.18	1.90±0.05
Background in %		4.38±0.18	1.86±0.05

Table 12: Relative acceptances

theoretical uncertainty on R with an experimental uncertainty based on a RunI measurement and use R=10.67±0.45. Table 8.2.4 shows the calculation of the relative acceptances, the applied correction to the Z$\rightarrow \mu\mu$ acceptance and the fractions of each individual process to the combined acceptance. The background fraction from Z$\rightarrow \mu\mu$ and $W \rightarrow \tau\nu$ events are then obtained by correcting for QCD, decay in flight and cosmic background events which were not included in the combined acceptance of the three processes. The MC is also used to obtain the kinematic shapes. Figure 72 shows the M_T distributions, Figure 73 the p_T distributions and Figure 74 the $\not\!\!E_T$ distributions for all backgrounds and total background overlaid.

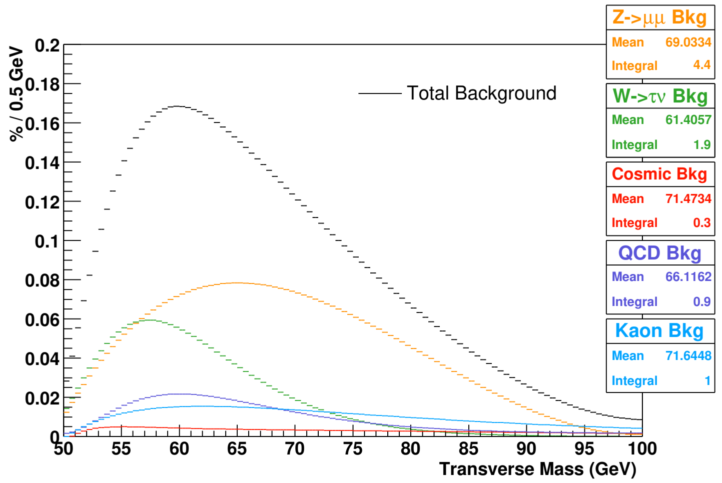

Figure 72: M_T distributions for all backgrounds and total background overlaid.

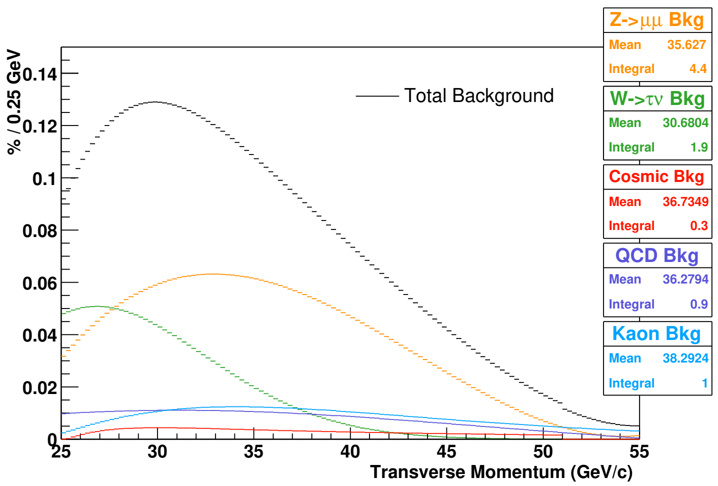

Figure 73: p_T distributions for all backgrounds and total background overlaid.

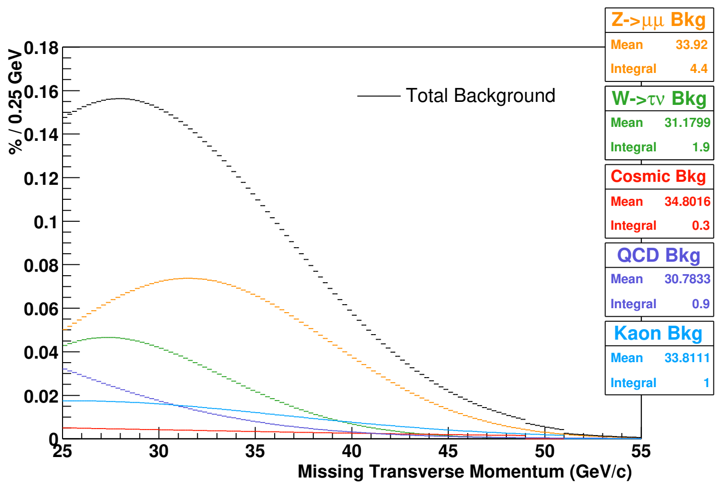

Figure 74: $\not{E}_T$ distributions for all backgrounds and total background overlaid.

8.2.5 Systematic uncertainty on W Mass

In order to obtain the systematic uncertainty on the W mass due to backgrounds a high statistics MC template and MC data file is generated. The data file is then fitted applying different background sizes or varied background shapes to the MC template.

To estimate the systematic uncertainty on the W mass due to the background size uncertainties, the backgrounds are varied by their uncertainties in the MC template. The systematic variations are listed in table 13.

Background	Size	ΔM_W in MeV (M_T fit)	ΔM_W in MeV (p_T fit)	ΔM_W in MeV ($\not\!\!E_T$ fit)
Z$\rightarrow \mu\mu$	4.4±0.2	2	0	7
W$\rightarrow \tau\nu$	1.9±0.1	4	6	6
QCD	0.9±0.5	12	4	18
Kaon	1.0±1.0	8	16	20
Cosmic Rays	0.3±0.1	1	1	0

Table 13: Systematic uncertainty on W mass due to background size uncertainty.

The fitted kinematic shapes also have some uncertainty which we estimate by fitting different shapes obtained from the 3σ contour of the fit parameters. These shape variations are applied to the MC template and a fit value is obtained for each. Table 14 lists the largest variations adjusted to 1σ shape uncertainty. In summary we estimate the following

Background	ΔM_W in MeV (M_T fit)	ΔM_W in MeV (p_T fit)	ΔM_W in MeV ($\not\!\!E_T$ fit)
Z$\rightarrow \mu\mu$	5	7	5
W$\rightarrow \tau\nu$	1	7	8
QCD	7	7	3
Kaon	2	3	3
Cosmic Rays	0	0	1

Table 14: Systematic uncertainty on W mass due to fitted shape uncertainty.

systematic uncertainty on the W mass due to backgrounds. 20 MeV for the M_T fit, 22 MeV for the p_T fit and 30 MeV for the $\not\!\!E_T$ fit.

9 Mass Fitter and Results

The W mass is extracted by performing a binned maximum-likelihood fit to various kinematic distributions: lepton and neutrino p_T, and transverse mass m_T. The Z mass, J/ψ mass and upsilon mass fits are similarly done using the dilepton mass distributions. Background line shapes are added to the simulated line shapes with specified normalizations. The sum of the simulated signal and background line shapes is normalized so that its integral in the specified fit region equals the integral of the data distribution in the same region. Using the simulation templates to give the expected number of events in each bin, the Poisson probability of the data in each bin is computed. The total likelihood is defined as the product of the Poisson probabilities over all bins in the fit region. The total likelihood is maximized as a function of the true parameter associated with the simulation templates, typically the particle mass, or energy/momentum scale.

We summarise here the results of the fits to the W mass kinematic distributions for both the electron and muon channels. We include a section summarising all the systematic uncertainties that have been described elsewhere. Finally we include a number of cross-checks that we have performed to ensure the integrity of the result.

9.1 Fit Results

We caution the reader that the fit results (the actual fit mass values) are still blinded (even to us!). We have generated a single random offset from a flat distribution between ± 100 MeV/c^2. This offset was put in a file that we then removed read access. The fits are performed, and yield the true W mass value, however before it is output the offset is added. We propose not to un-blind the result before we get significant feedback from the collaboration and we satisfy ourselves that all cross-checks, we can think of, succeed. This will either occur between the pre-blessing and the blessing or maybe even after the blessing. The offset is common to the electron and muon fits in each of the three kinematic distributions we are studying. Thus we can already appreciate the consistency of the fit results by comparing the 'blinded' numbers.

Figures 75-79 show the fits to the electron sample. The fit regions are $60 < m_T < 90$ GeV, $30 < p_T < 45$ GeV, and $30 < \not{E}_T < 45$ GeV respectively. These results are summarised in Table 15. We have performed a set of MC fits to these three distributions to determine the expected correlation between these three results. We have measured the statistical correlations between the m_T and p_T fits to be 90% correlated while the m_T and $p_T(\nu)$ fits are 70% correlated. We believe that the variations observed between the fit values here are consistent with those correlations.

Figures 76-80 also show the same fits to the muon sample, with the same fit regions. Once again the results are summarised in Table 15. We have measured the correlations between the m_t and p_t fits to be 85% correlated the m_t and $p_t(\nu)$ fits are 87% correlated and the p_t and $\not{E}_T$ fits are 80% correlated. The pseudo-experiment studies that lead to these correlations are shown in figures 81-83 where the systematic uncertainties come from an analysis of the

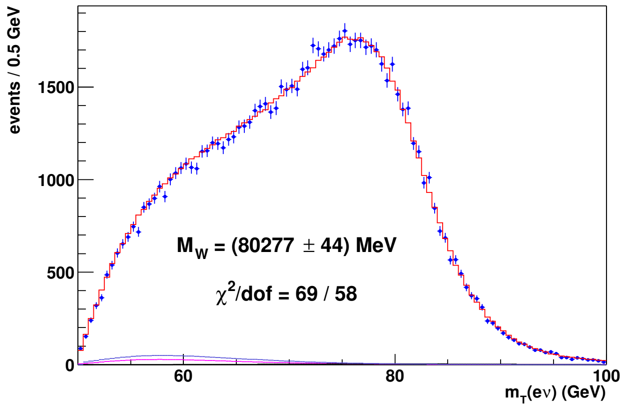

Figure 75: The W transverse mass fit for electron channel.

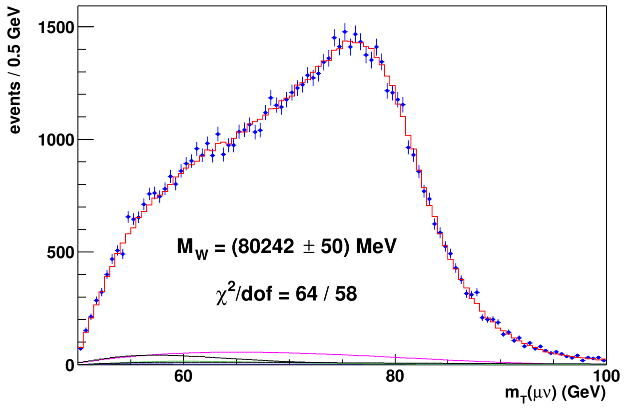

Figure 76: The W transverse mass fit for muon channel.

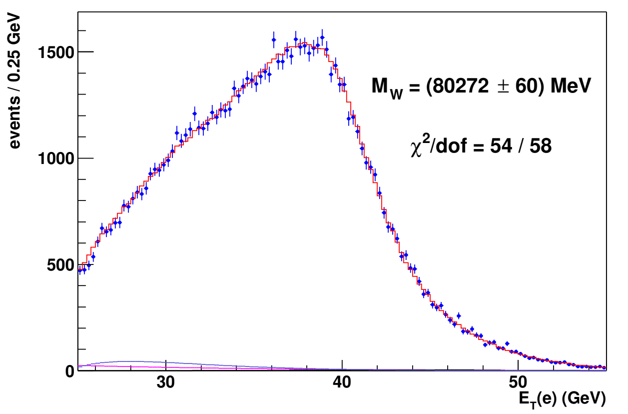

Figure 77: The W electron p_T fit.

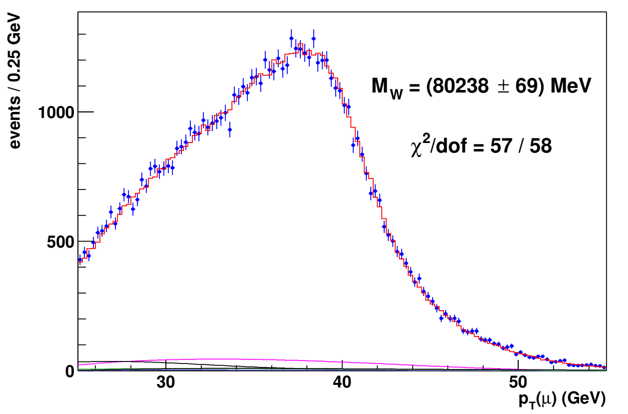

Figure 78: The W muon p_T fit.

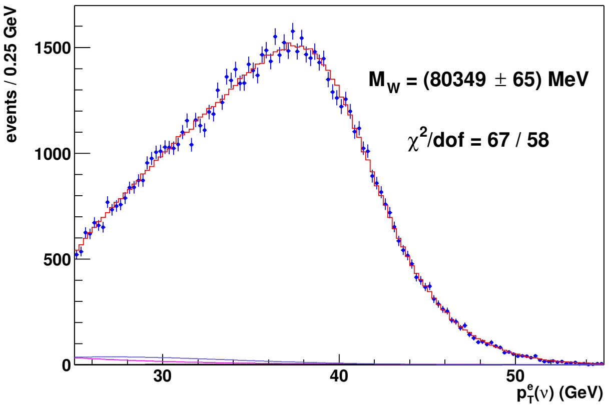

Figure 79: The W missing E_T fit for electron channel.

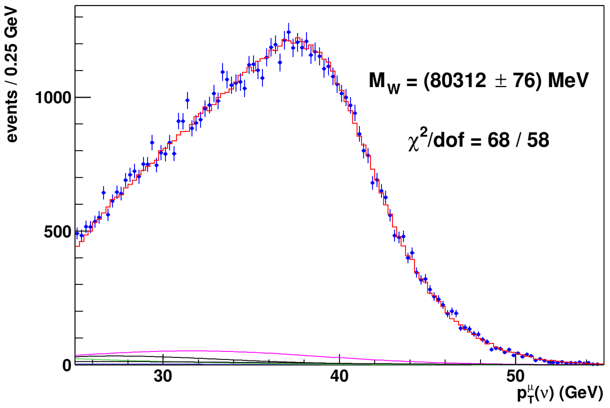

Figure 80: The W missing E_T fit for muon channel.

Charged Lepton	Kinematic Distribution	Fit Result (MeV/c^2)	χ^2/DoF
Electron	Transverse Mass	80277 ± 44	69/58
Electron	Transverse Momentum	80272 ± 60	54/58
Electron	Neutrino p_t	80349 ± 65	67/58
Muon	Transverse Mass	80242 ± 50	64/58
Muon	Transverse Momentum	80238 ± 69	57/58
Muon	Neutrino p_t	80312 ± 76	69/58

Table 15: Fit results for electrons and muons from the three kinematic distributions that we use to extract m_W.

influence of the remaining statistical uncertainty on the 100 individual pseudo-experiment results, while the statistical uncertainty comes from computing the correlation coefficient assuming each pair of measurements is infinitely precise. We believe that the variations observed between the fit values here are consistent with those correlations.

Since the statistical correlations are high so we do not combine the results of the fits to the three different kinematic distributions for each charged lepton species. Instead, given the high correlations, the three fits provide cross-checks of the result and our overall fitting model. We are working on quantifying the degree to which the three different fits are consistent with the correlations predicted by MC tests.

Once we have discussed the systematic uncertainties (see Sec. 9.2), and their degree of correlation between electrons and muons, we can proceed to combine these results to get an overall W mass value.

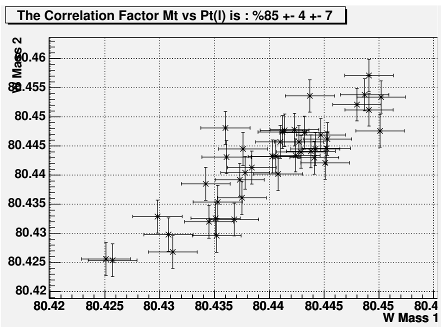

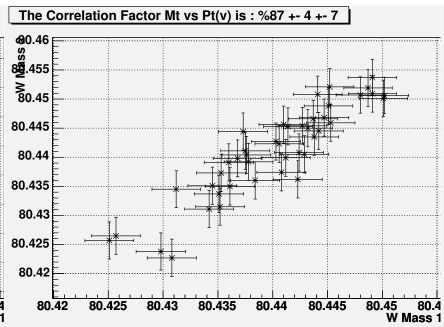

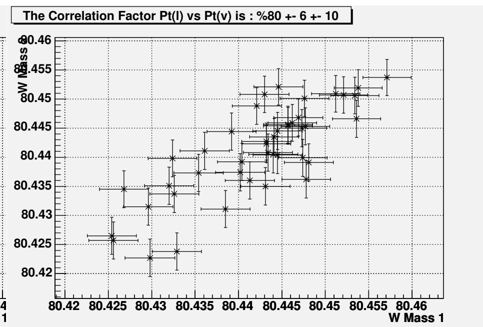

Figure 81: The correlation between m_t and p_t fits for 100 pseudo-experiments. The statistical uncertainty on the correlation coefficient arises from the scatter of the points – assume each is infinitely precise. The systematic uncertainty is computed by sampling the residual statistical uncertainty on each point and seeing how much that could distort the correlation coefficient.

Figure 82: The correlation between m_t and $\not{E}_T$ fits for 100 pseudo-experiments. The statistical uncertainty on the correlation coefficient arises from the scatter of the points – assume each is infinitely precise. The systematic uncertainty is computed by sampling the residual statistical uncertainty on each point and seeing how much that could distort the correlation coefficient.

Figure 83: The correlation between p_t and $\not{E}_T$ fits for 100 pseudo-experiments. The statistical uncertainty on the correlation coefficient arises from the scatter of the points – assume each is infinitely precise. The systematic uncertainty is computed by sampling the residual statistical uncertainty on each point and seeing how much that could distort the correlation coefficient.

9.2 Systematic Uncertainties

We summarise the systematic uncertainties resulting from our study of the various inputs to our kinematic lineshape model as described in the previous sections of the note. Table 16 gives a summary of our current understanding of all systematics as well as some indication as to whether they are correlated between electrons and muons. For now we concentrate on the systematics on the transverse mass distributions but prior to blessing it should be possible to produce similar tables for the charged lepton p_t fits and neutrino p_t fits.

The "lepton scale" uncertainty includes the effect of the momentum resolution from Sec. 5.3-5.5 for the muons and Sec. 6.1 for the electrons. This results in a 25 MeV/c^2 uncertainty on the muons (including 15 MeV/c^2 from the scale and 20 MeV/c^2 from the curvature corrections) and 77 MeV/c^2 uncertainty on the electrons (including the 25 MeV/c^2 from the momentum scale, 30 MeV/c^2 from the statistical uncertainty on the E/p fit and 66 MeV/c^2 from the material matching in the E/p tail) and 25 MeV/c^2 from the calorimeter non-linearity. The resolution on the charged lepton measurements changes the slope of the Jacobian edge resulting in an apparent mass shift. Our constraints on this resolution come from Sec. 6.1 for the electrons and Sec. 5.6 for the muons. To reduce our sensitivity to the finite statistics of even very large MC samples we vary the resolution in our lineshape simulation up and down by twice the uncertainties quoted on the respective resolutions. We then divide the apparent mass shifts from MC simulations by four to get the effective 1σ systematics due to charge lepton resolution.

Similarly we vary the uncertainties on our recoil model parameters by twice those quoted in Sec. 7 and run these through our MC simulation. We take the resulting shifts in mass and divide by two to get the systematics quoted in the table.

We estimate that there is a 15 (10) MeV systematic in the underlying event energy that is removed when we remove the electron (muon) towers in the recoil measurement (see Sec. 3.7). There is no uncertainty associated with the lepton p_T fits, and twice as large an uncertainty for the $\not{E}_T$ fits. The electron and muon uncertainties are measured from different data samples and hence we take them to be uncorrelated.

Backgrounds are discussed in Sec. 8.1 for electrons and Sec. 8.2 for muons. There we varied the shapes and normalisations of the various background constituents. The QCD background (in particular the decay in flight background for muons) are by far the largest and least well understood backgrounds. We end up with systematic uncertainties of 15 and 20 MeV/c^2 for electrons and muons, respectively.

In Sec. 2 we investigated the influence of the non-perturbative, phenomenological, parameters that control the low $p_t(W)$ shape in the generation of W bosons with `RESBOS`. Despite the generous ranges over-which we varied these parameters we conclude that our systematic here is 15 MeV/c^2, common to electrons and muons. This does not cover the shape of the $p_t(W)$ distribution for higher momentum W bosons. This part of the spectrum is much more sensitive to the response of the CDF detector to the underlying event. The systematics for these effects are included in our investigation of the recoil response model.

Section 2.4 discussed the variation of our lineshape due to different choices of parton distribution functions. We used the full CTEQ6M error PDF set and concluded that the

Systematic (MeV/c^2)	Electrons	Muons	Common	Electrons (Ib)	Muons (Ib)
Lepton Scale	81	25	25	75	85
Calorimetry Non-Linearity	25	0	0		
Lepton Resolution	7	12	0	25	20
Recoil Scale	20	20	20	37	35
Recoil Resolution	42	42	42	"	"
u_{par} efficiency	7	7	0	0	18
Lepton Removal	15	10	10	"	"
Backgrounds	16	20	0	5	25
$p_T(W)$ model (g_1, g_2, g_3)	13	13	13	15	20
Parton Distributions	15	15	15	15	15
QED radiation	15	20	12	20	10
Γ_W	12	12	12	-	-
Total	104	66	59	92	103

Table 16: Table of systematic uncertainties for transverse mass fits. When comparing to the Ib result some uncertainties were combined. The quotes indicate IIa uncertainties that likely form part of the Ib quoted on the line above.

transverse mass distribution was sensitive at the 15 MeV/c^2 level, see Table 16. A cross-check with a recent MRST PDF showed that this was not an unreasonable level of uncertainty.

In Sec. 2 we also investigated the various effects of QED radiation on our line shape. At this point we conclude that our model is susceptible to 25 MeV/c^2 uncertainties for electrons (which are more likely to radiate) and 21 MeV/c^2 uncertainties for muons.

We generate our fitting templates with $\Gamma_W = 2.12$ GeV/c^2. Direct measurements of this width give a world average uncertainty of 70 MeV/c^2 that more than covers the indirect width of the W which is 2.09 GeV/c^2. This 70 MeV/c^2 uncertainty on the width translates into a 12 MeV/c^2 uncertainty on the W mass. We include this as a systematic that is common to the electron and muon fits.

We were asked to compare our systematic uncertainty estimates with those from the CDF Ib measurement. We include two extra columns in table 16 with the Ib results. In some cases uncertainties we have treated separately were (likely) combined in the Ib result. In general, one sees that we are significantly more confident of our calibration systematics as all cross-checks we have performed seem to work out. Other systematics are very comparable. In some cases we are still more conservative and expect to do better as we work through additional cross-checks.

9.3 Cross-Checks

As discussed in section 9.1 and tabulated in table 16 we fit not only the transverse mass distribution – but also the charge lepton p_t distributions, for each lepton flavour, and the neutrino missing E_T distribution. In order to fully appreciate the degree to which these other fits support/agree with the transverse mass fits we need two ingredients: 1) the statistical correlation between fits to the different kinematic distributions and 2) estimates of the analogous systematics to those listed in table 16 for the transverse mass distribution.

We have performed a number of Monte Carlo simulated fit samples with 70,000 events in order to measure the statistical correlation between fits to the m_t, p_T and missing $\not{E}_T$ distributions.

We have also performed all the systematic variations listed in table 16 for the p_T and $\not{E}_T$ fits. These systematics are listed in tables 17 and 18, respectively.

We have also divided the data into several kinematic sub-samples and check the W mass fits in these regions. We do this for electrons and muons and for each of the three kinematic variables described above: m_t, $p_t(l^+)$ and $p_t(\nu)$. The results are listed in table 19.

We show the signed χ distributions (data$-$MC normalized by statistical error on data), of the W mass fits, in Figs. 84-89. The variation of the fitted mass values, relative to the nominal results, as the fit region is varied, is shown in Fig. 90-101.

We have also performed MC tests of our fitter in order to estimate the statistical uncertainties on each of our six fits. The results of these MC tests are plotted in figure 102 to 107. We see that the statistical uncertainties on our data fits are consistent with our expectations (or slightly conservative – but we are working to understand this).

Systematic (MeV/c^2)	Electrons	Muons	Common
Lepton Scale	81	25	25
Calorimeter Non-Linearity	25	0	0
Lepton Resolution	5	11	0
Recoil Scale	5	5	5
Recoil Resolution	16	16	16
$u_{\|\|}$ efficiency	5	5	0
Lepton Removal	0	0	0
Backgrounds	6	22	0
$p_T(W)$ model (g_1, g_2, g_3)	27	27	27
Parton Distributions	18	18	18
QED radiation	15	20	12
Γ_W	12	12	12
Total	94	55	44

Table 17: Table of systematic uncertainties for the charged lepton p_T fits.

Systematic (MeV/c^2)	Electrons	Muons	Common
Lepton Scale	81	25	25
Calorimeter Non-Linearity	25	0	0
Lepton Resolution	7	12	0
Recoil Scale	20	20	20
Recoil Resolution	72	72	72
$u_{\|\|}$ efficiency	22	22	0
Lepton Removal	30	20	20
Backgrounds	8	30	0
$p_T(W)$ model (g_1, g_2, g_3)	18	18	18
Parton Distributions	19	19	19
QED radiation	15	20	12
Γ_W	12	12	12
Total	121	96	83

Table 18: Table of systematic uncertainties for the missing transverse energy fits.

Lepton	Sub-sample	m_t	$p_t(l^{\pm})$	$p_t(\nu)$
Electron	positive	+88±65	+97±87	+55±92
Electron	negative	-80±62	-98±82	-55±91
Electron	up		+65±87	
Electron	down		-63±87	
Electron	early (run< 161000)	+70±68	+36±94	+103±101
Electron	late (run> 161000)	-50±60	-33±81	-75±84
Muon	positive	$+112 \pm 69$	$+182 \pm 96$	$+30 \pm 106$
Muon	negative	-110 ± 69	-183 ± 96	-27 ± 106
Muon	up		-72±96	
Muon	down		+90±110	
Muon	early (run< 161000)	-120±88	-30±122	+42±133
Muon	late (run> 161000)	+62±64	+15±90	-23±95

Table 19: Fit mass shifts (in MeV/c^2) for sub-divisions of our data.

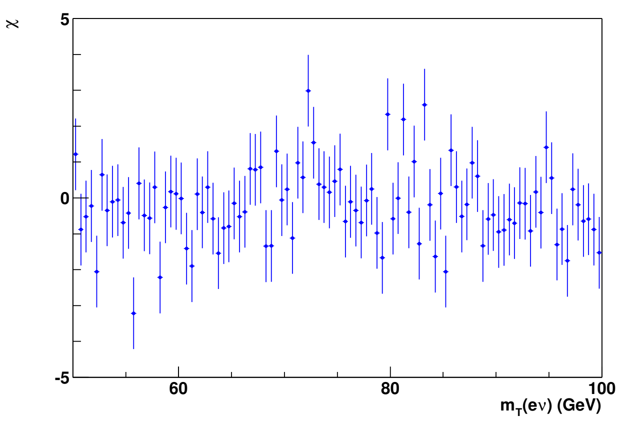

Figure 84: The signed χ distribution of the W transverse mass fit for electron channel.

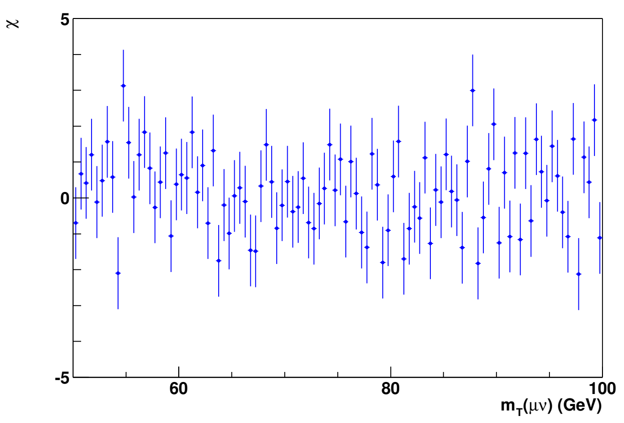

Figure 85: The signed χ distribution of the W transverse mass fit for muon channel.

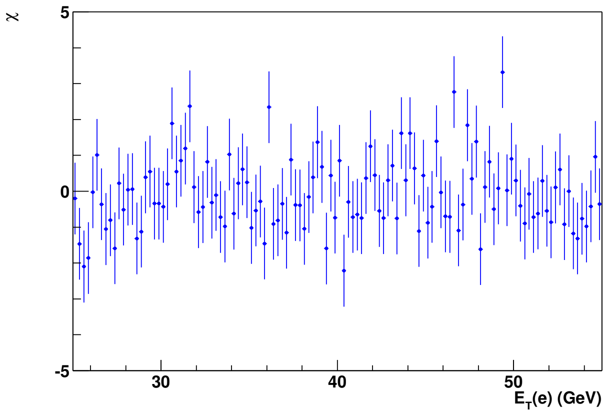

Figure 86: The signed χ distribution of the W electron p_T fit.

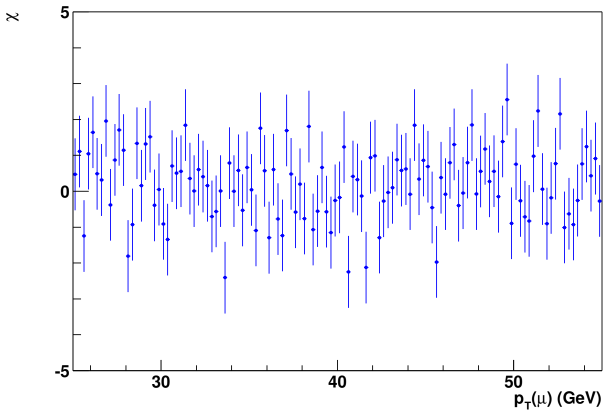

Figure 87: The signed χ distribution of the W muon p_T fit.

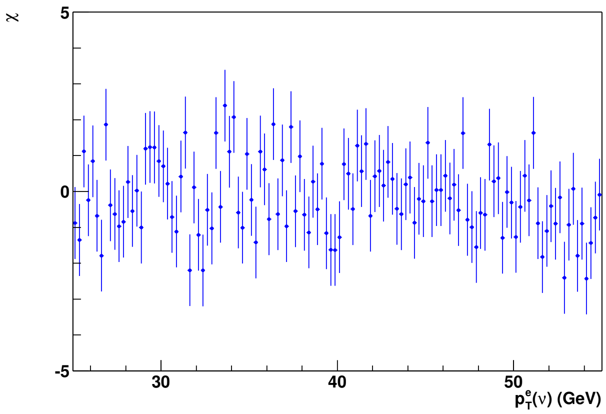

Figure 88: The signed χ distribution of the W $\not\!\!E_T$ fit for electron channel.

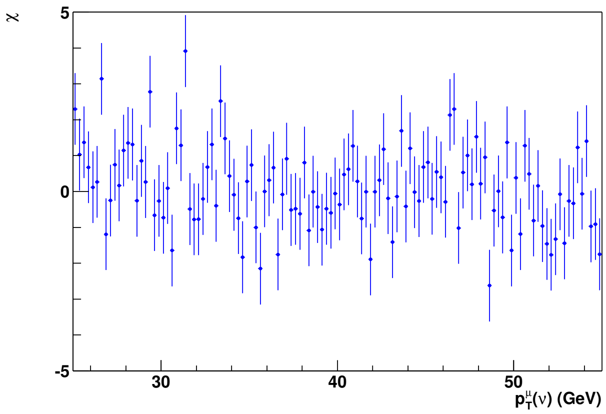

Figure 89: The signed χ distribution of the W $\not\!\!E_T$ fit for muon channel.

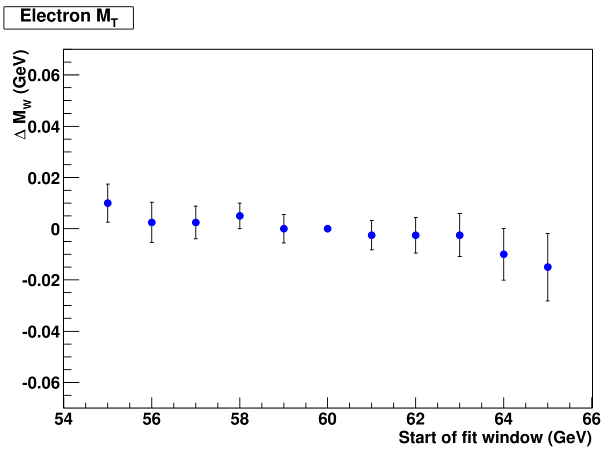

Figure 90: The variation of the W transverse mass fit with low fit window edge, for electron channel. Error bars indicate expected variation from MC pseudo-experiments.

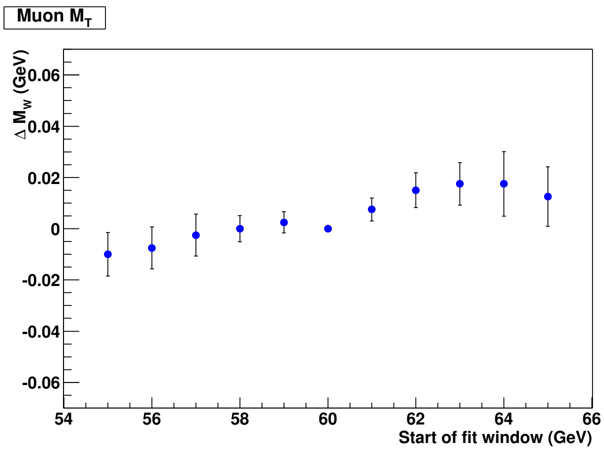

Figure 91: The variation of the W transverse mass fit with low fit window edge, for muon channel. Error bars indicate expected variation from MC pseudo-experiments.

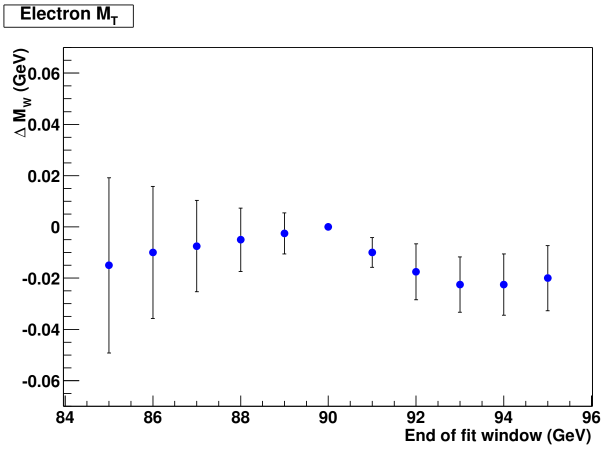

Figure 92: The variation of the W transverse mass fit with high fit window edge, for electron channel. Error bars indicate expected variation from MC pseudo-experiments.

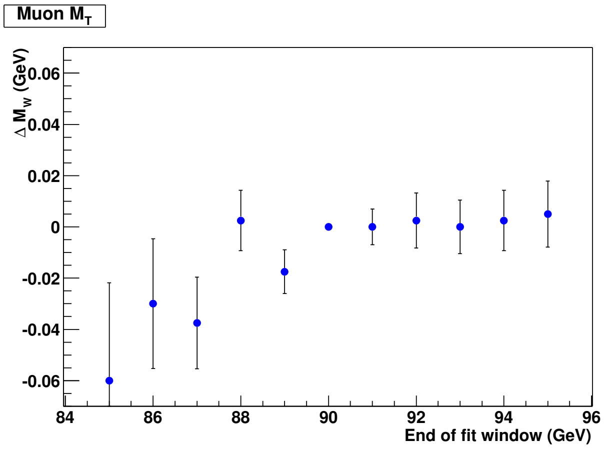

Figure 93: The variation of the W transverse mass fit with high fit window edge, for muon channel. Error bars indicate expected variation from MC pseudo-experiments.

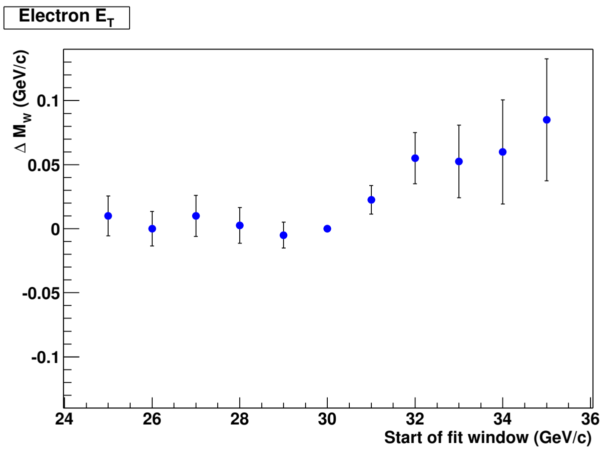

Figure 94: The variation of the p_T fit W mass with low fit window edge, for electron channel. Error bars indicate expected variation from MC pseudo-experiments.

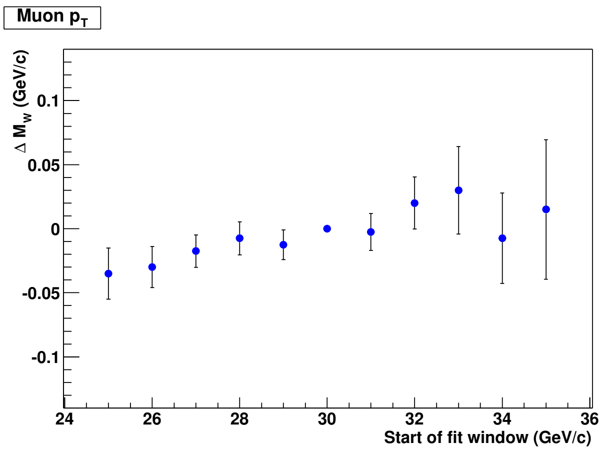

Figure 95: The variation of the p_T fit W mass with low fit window edge, for muon channel. Error bars indicate expected variation from MC pseudo-experiments.

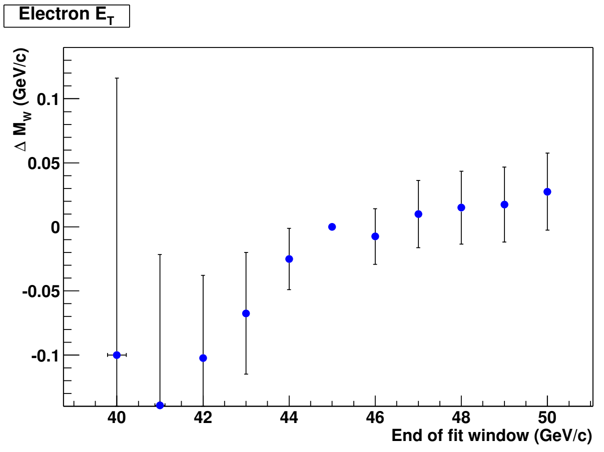

Figure 96: The variation of the p_T fit W mass with high fit window edge, for electron channel. Error bars indicate expected variation from MC pseudo-experiments.

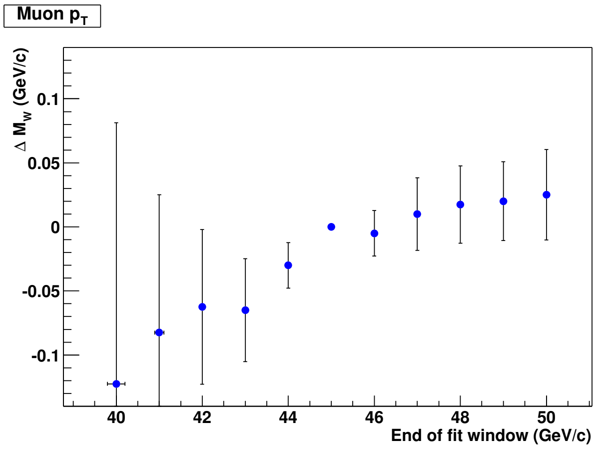

Figure 97: The variation of the p_T fit W mass with high fit window edge, for muon channel. Error bars indicate expected variation from MC pseudo-experiments.

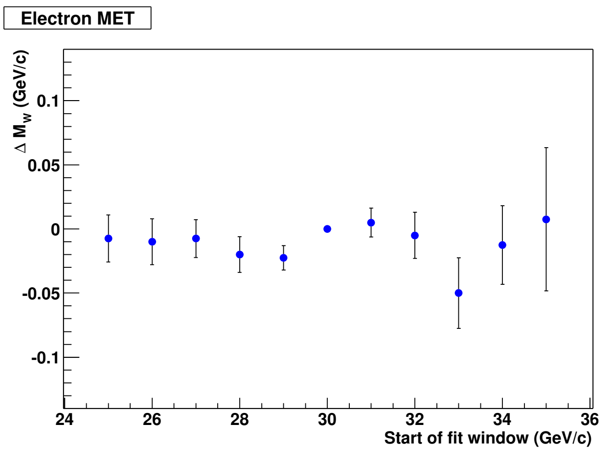

Figure 98: The variation of the $\not{E}_T$ fit W mass with low fit window edge, for electron channel. Error bars indicate expected variation from MC pseudo-experiments.

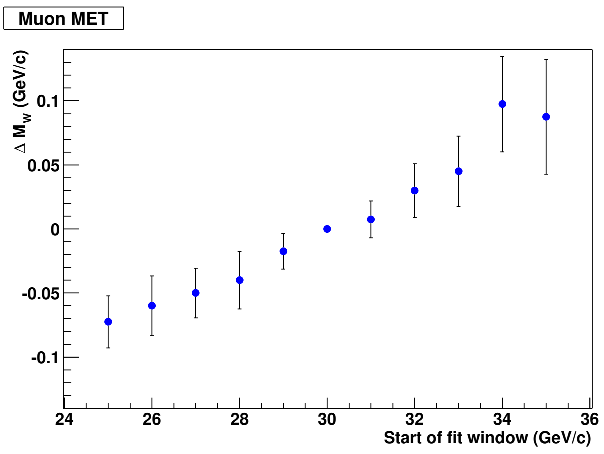

Figure 99: The variation of the $\not{E}_T$ fit W mass with low fit window edge, for muon channel. Error bars indicate expected variation from MC pseudo-experiments.

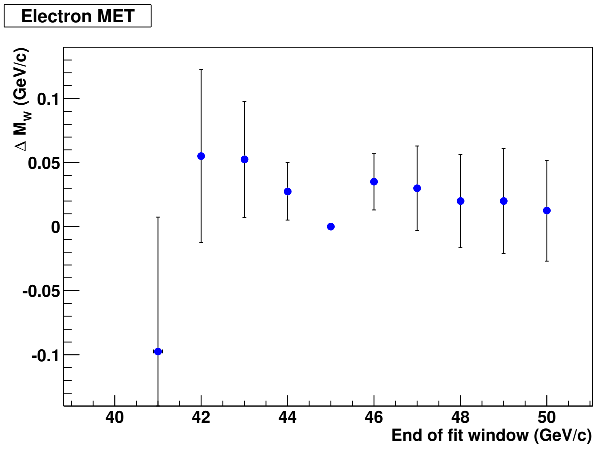

Figure 100: The variation of the $\not{E}_T$ fit W mass with high fit window edge, for electron channel. Error bars indicate expected variation from MC pseudo-experiments.

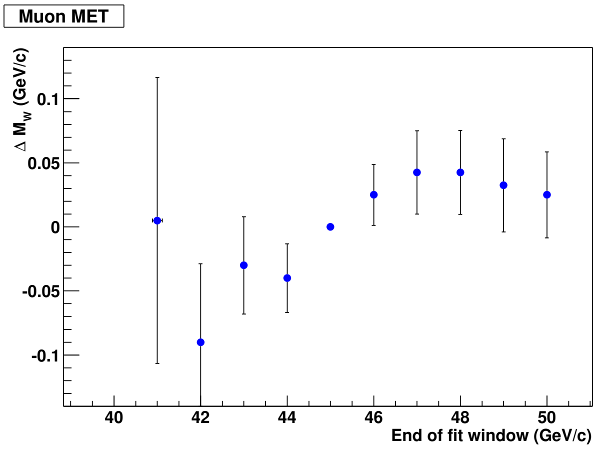

Figure 101: The variation of the $\not{E}_T$ fit W mass with high fit window edge, for muon channel. Error bars indicate expected variation from MC pseudo-experiments.

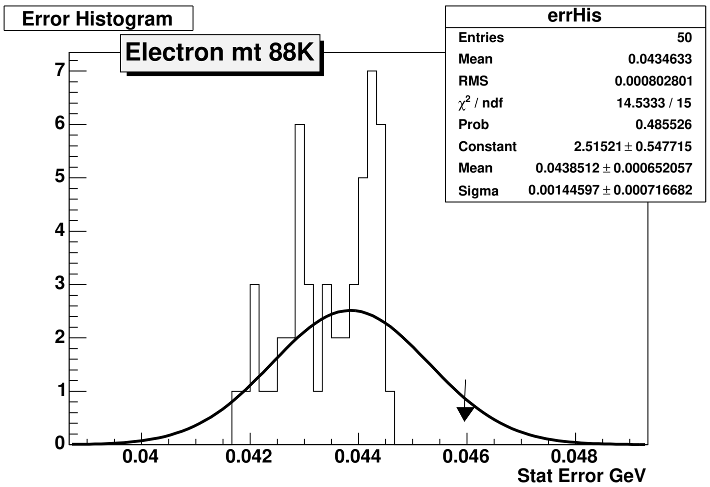

Figure 102: The expected statistical uncertainty for the W transverse mass fit for electron channel. The arrow indicates the uncertainty on the fit to our data sample.

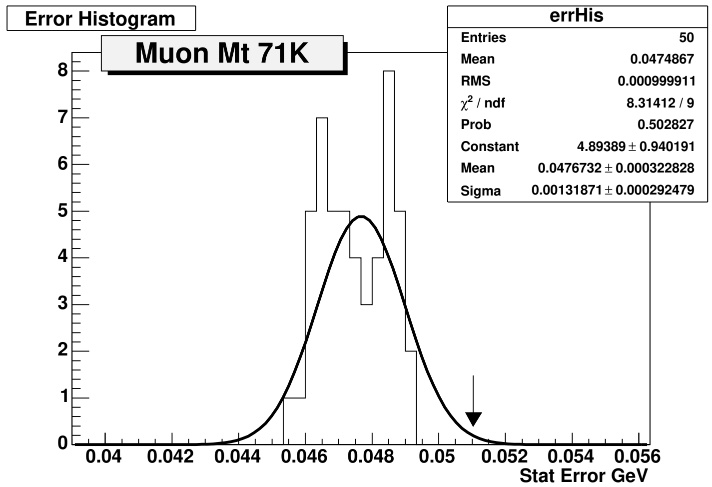

Figure 103: The expected statistical uncertainty for the W transverse mass fit for muon channel. The arrow indicates the uncertainty on the fit to our data sample.

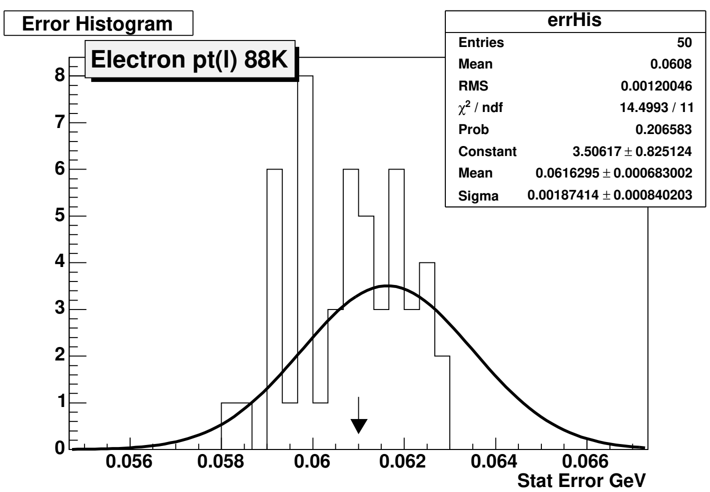

Figure 104: The expected statistical uncertainty for the W electron p_T fit. The arrow indicates the uncertainty on the fit to our data sample.

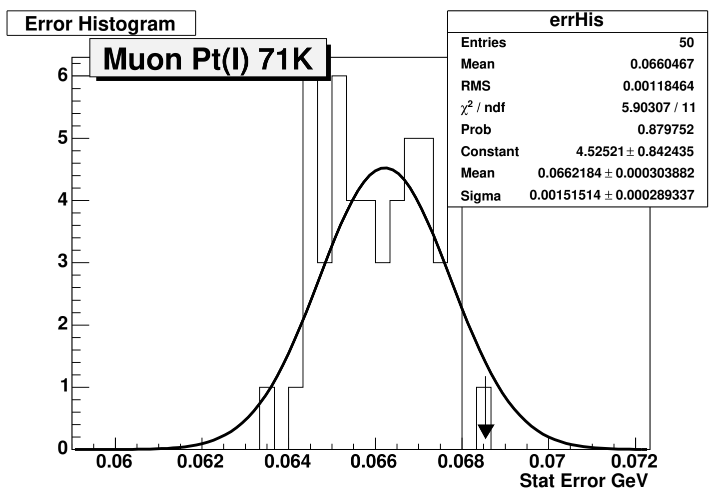

Figure 105: The expected statistical uncertainty for the W muon p_T fit. The arrow indicates the uncertainty on the fit to our data sample.

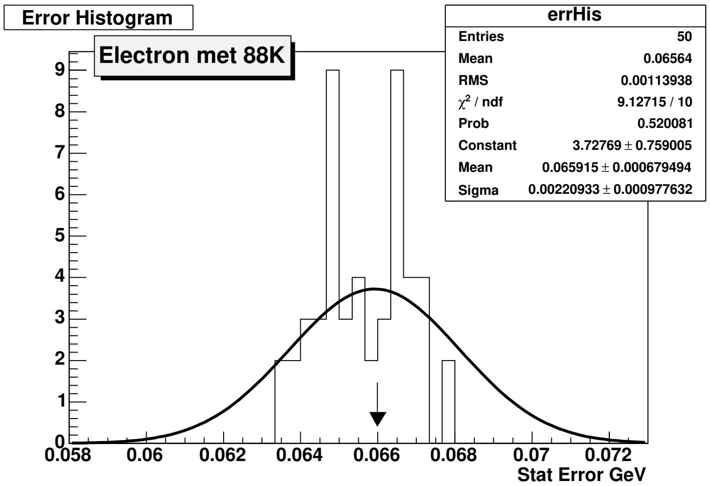

Figure 106: The expected statistical uncertainty for the W missing E_T fit for electron channel. The arrow indicates the uncertainty on the fit to our data sample.

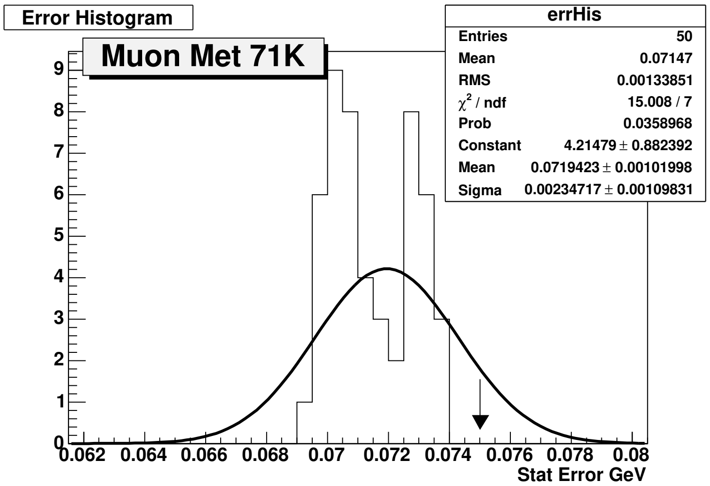

Figure 107: The expected statistical uncertainty for the W missing E_T fit for muon channel. The arrow indicates the uncertainty on the fit to our data sample.

9.4 Combined Mass Result

We combine the two results by weighting the two results with their independent uncertainties – both statistical and independent systematics. With the numbers (and commonality) quoted in Table 16 and the statistical precisions from Table 15 the electrons account for 40 % of the weight and the muons 60 % of the weight. The combined mass value from the transverse mass fits is:

$$m_W = 80257 \pm 33 \text{ (stat.)} \pm 70 \text{ (syst.) MeV/c}^2 = 80257 \pm 77 \text{ MeV/c}^2$$

The difference between the electron and muon fits (based on the independent uncertainties) is 0.5 standard deviations.

The combination of the cross-check fits gives:

$$m_W = 80252 \pm 45 \text{ (stat.)} \pm 60 \text{ (syst.) MeV/c}^2 = 80252 \pm 75 \text{ MeV/c}^2$$

from the charged lepton p_T fits (a difference of 0.3 standard deviations) and:

$$m_W = 80325 \pm 49 \text{ (stat.)} \pm 98 \text{ (syst.) MeV/c}^2 = 80325 \pm 110 \text{ MeV/c}^2$$

(a difference of 0.3 standard deviations) from the missing $\not{E}_T$ fit.

To put in context the difference between the $\not{E}_T$ fit result and the m_T fit result, we expect the statistical uncertainty on the difference to be at the $\sqrt{49^2 - 33^2} = 36$ MeV/c^2 level. It seems reasonable to have a systematic uncertainty on the difference at the level of

Experiment	Mass (MeV/c^2)
L3	80376 ± 77
DELPHI	80404 ± 74
OPAL	80490 ± 65
ALEPH	80379 ± 58
CDF-I	80433 ± 79
D0-I	80483 ± 84
LEP Average	80412 ± 42
Tevatron Average	80454 ± 59
World Average	80426 ± 34
CDF-II	80257 ± 77
"New Average"	80399 ± 31

Table 20: Current world's best W mass measurements. Note that the LEP experiment results include about 30 MeV/c^2 of correlated systematic uncertainty from the LEP beam energy measurement and color recombination effects.

$\sqrt{98^2 - 70^2} = 68$ MeV/c^2. Thus the total uncertainty on the difference is $\mathcal{O}(77)$ MeV/c^2. So the difference between the m_T and $\not{E}_T$ fits is about one standard deviation.

9.5 Comparison to Previous Results

Table 20 shows how our result compares to the other measurements that are currently part of the PDG world average.

10 Summary and Future Plans

References

[1] C. Balazs and C.-P. Yuan, Phys. Rev. D **56** 5558 (1997).

[2] U. Baur, S. Keller, and D. Wackeroth, Phys. Rev. D **59** 013002 (1998).

[3] M. Lancaster and D. Waters, *CDF Note* **5240** (2000).

[4] F.A. Berends, R. Kleiss, J.P. Reval, and J.P. Vialle, Z. Phys. C **27**, 155 (1985); F.A. Berends and R. Kleiss, *ibid.* **27**, 365,(1985).

[5] U. Baur, private communication.

[6] T. Affolder *et al.*, Phys. Rev. D. **64**, 052001 (2001).

[7] M. Lancaster, *CDF Note* **4048** (1997).

[8] C.M. Carloni Calame, G. Montagna, Nicrosini, and M. Treccani, Phys. Rev. D. **69**, 037301 (2004).

[9] F. Landry, R. Brock, P. M. Nadolsky, and C.-P. Yuan, Phys. Rev. D **67**, 073016 (2003).

[10] F. Landry, R. Brock, G. Ladinsky, and C.-P. Yuan, Phys. Rev. D **63**, 013004 (2000).

[11] A general-purpose framework for PDF analysis using PYTHIA and ROOT has been developed by Pasha Murat.

[12] Kurt Rinnert, private communication.

[13] Ray Culbertson, private communication. The code for fast simulation of COT geometry, track propagation, hit generation and fitting was originally written by Ray for COT alignment studies.

[14] C. Hays and A. V. Kotwal, *CDF Note* **7119** (2004).

[15] H. K. Gerberich, A. V. Kotwal, and C. Hays, *CDF Note* **6089** (2002); A. V. Kotwal, H. K. Gerberich and C. Hays, Nucl. Instrum. Methods Phys. Res. A **506**, 110 (2003).

[16] *http://phy.duke.edu/ hkg/ntuple/*

[17] C. Hays and A. V. Kotwal, *CDF Note* **7118** (2004).

[18] C. Hays and A. V. Kotwal, *CDF Note* **7110** (2004).

[19] M. Lancaster, private communication.

[20] B. Abbott *et al.*, Phys. Rev. D **58**, 092003 (1998).

[21] Larry Nodulman *CDF Note* **6971** (2004).

[22] Kindly provided by Mark Lancaster and Dave Waters.